LABORATORY CHARACTERIZATION, MODELING, AND NUMERICAL SIMULATION OF AN EXCAVATION DAMAGED ZONE AROUND DEEP GEOLOGIC REPOSITORIES IN SEDIMENTARY ROCKS

FINAL REPORT

Prepared by

Hadj Abdi and Dr. Erman Evgin

Department of Civil Engineering
University of Ottawa
Ottawa, Ontario, Canada K1N 6N5

uOttawa

for

Canadian Nuclear Safety Commission

February 8, 2013

Summary

This report contains (1) A literature review, (2) Experimental data for the mechanical behavior of Tournemire argillite, (3) A constitutive model for the mechanical behavior of Tournemire argillite, and (4) Numerical simulation of EDZ around a proposed DGR in Cobourg limestone at the Bruce site, Canada.

The experimental program includes the measurements of the physical properties of the transversely isotropic material of the Tournemire argillite and its mechanical response under uniaxial tests, triaxial tests with different confining pressures, unconfined and confined cyclic tests, Brazilian tests, and creep tests.

Based on the experimental data, an elastoplastic model has been developed to simulate the mechanical behavior of the Tournemire argillite in triaxial tests. The model is formulated using the classical theory of plasticity and continuum damage mechanics concepts. All model parameters are estimated from the experimental data.

The numerical simulations consisted of (1) Two and three dimensional finite element analyses which dealt with the mechanical (M) aspects of the problem, and (2) Plane strain finite element analyses of the coupled Hydro -Mechanical (HM) processes around an emplacement room at Bruce site. The influence of the anisotropic fluid flow characteristics on the development of the excavation damaged zone is investigated.

Table of Contents

Part 1

Literature review on the state-of-the-art knowledge on the development of DGRs

1.1. Background

Many international cooperative projects have been implemented in support of the performance assessment for underground disposal of radioactive wastes. One of the goals for these projects were to conduct cooperative research on modeling coupled processes in geologic formations. As an example, the DECOVALEX project was designed to model the evolution of the EDZ and investigate the effects of coupled THMC processes around a DGR in hard rocks. A summary of the results from the DECOVALEX-THMC project can be found in, e.g., Hudson et al. (2008).

Tunneling affects the in situ stress field. Consequently, tension, compression, and shear can develop at different parts of the tunnel. For unsupported tunnels, the stress normal to the walls is vanished while tangential stresses may increase significantly and can lead to local failures under tension and/or shear. Such processes can be accelerated by the disturbance caused by the excavation to the hydraulic regime within the rock formation. A part of the near-field rock could become compressed or sheared and porewater pressure may increase or decrease locally.

Kaiser et al. (2000) stated that two forms of instability can develop around underground openings. Structurally controlled failures are common in low confining stress environments at shallow depths, and stress-induced yielding occurs when stress magnitudes reach the rock mass strength. In weak and soft rocks the yielding may result in large convergence displacements. In hard and strong rocks the yielding may result in relatively small convergence displacements.

In recent years, efforts have been made to study various locations for a potential repository in three broad rock types, namely, crystalline rock, salt, and argillaceous formations. All these efforts have involved large-scale field tests, laboratory characterization, theoretical studies, and numerical modeling. Among the three rock types, field studies of argillaceous rocks are probably the most extensive. These have included large-scale tests in which flow over 10 m distance along an EDZ has been measured and evaluated (Bastiaens and Mertens, 2003). These large-scale measurements have the advantage of being able to account for realistic anisotropy and heterogeneity effects that are always present in situ.

1.2. Potential types of rock mass to host radioactive waste

1.2.1. Crystalline rocks

Several countries are considering construction of repositories in crystalline rock below the groundwater table. These rocks generally have extremely low permeability, except where they are fractured. Major excavation response experiments in crystalline rocks have been finalized including Stripa and Aspo (Sweden), AECL URL (Canada), Grimsel (Switzerland), and KURT (South Korea).

The Stripa project was carried out in an abandoned iron mine (Carlsson 1986). The objective of this project was to test the predictive capabilities of radar and seismic characterization methods and numerical groundwater models. Most of the experiments were carried out at the 360-meter level in massive granite. The functionalities of the bentonite as a buffer material were evaluated. The orientation and the extent of fractures in the site were mapped successfully. Stress-permeability relationships were developed and major flow paths were identified.

The URL project was developed in the Canadian Shield for the purpose of carrying out large scale in situ tests in the granite of Lac Du Bonnet. The main working levels of the URL are at depths of 240 and 420 m. The geology and fracture distributions in the vicinity of the URL site were extensively investigated (Soonawala, 1984). Souley et al. (2001) found that the in situ measurements of permeability and predictions were globally in agreement, and the depth of 50–70 cm is a good estimation of the extent of the EDZ. The cross-section of the tunnel had an elliptical shape with approximated dimensions of 4.4 m horizontally and 3.5 m vertically. Rutqvist et al. (2009) carried out numerical modeling for the excavation-induced damage, permeability changes, and fluid-pressure responses. The modeling indicated that stress-induced permeability increase above the tunnel is a result of micro and macro-fracturing under high deviatoric (shear) stresses, whereas permeability increase alongside the tunnel is a result of opening of existing micro-fractures under the decrease in mean stress.

Also at the URL project, the tunnels excavated at the 420-meter level showed signs of instability such as spalling and notch development (Martin, 1993). It is generally assumed that cohesion and friction of the material are mobilized at the same displacements such that both components can be relied on simultaneously. However, damage testing of samples of Lac du Bonnet granite has shown that as friction is mobilized in the sample, cohesion is reduced (Martin and Chandler, 1994).

The Grimsel project consists of several 3.5 m diameter tunnels excavated in granite. The purpose of this project is to carry out tests in many branches of science including geology,

geophysics, hydrogeology, rock mechanics, and nuclide transport. The data obtained in this project was used to improve the understanding of the interaction between modelling, laboratory tests, and in situ tests. The investigation included heat transfer, rock stress measurements, EDZ, and chemical transport.

In South Korea, a small scale underground research laboratory (KURT) was developed in granite to investigate the behavior of barriers (Cho et al. 2008). Borehole drilling, geological survey, and in situ and laboratory tests were carried out to validate the numerical modeling. It was found that the size of the EDZ varied from 1.1 m to 1.5 m around the 6 x 6 m horseshoe shaped tunnel. The degradation in the elastic modulus and rock strength within the EDZ were around 50% and 15%, respectively.

International experts carried out a variety of experiments at a depth of nearly 500 meters in the Aspo underground hard rock laboratory to test the repository's barriers (Autio et al. 2003). It was found that the porosity of the damaged rock was higher than the porosity of undisturbed rock. The average depth of the damaged zone varies from 5 to 20 mm from the excavation wall around the 5 m diameter tunnel. The extent of the EDZ and the conductivity of the EDZ adjacent to the floors of the tunnels are generally larger than in the roof and wall sections (Autio et al. 2005).

The excavation method is an important factor in controlling the excavation damage. Using TBM method, less than 5 mm of damage were recorded at Aspo and at Grimsel projects. Excavation using drilling and blasting resulted in more damage. In the ZEDEX project, Emsley et al (1997) found that the extent of the damaged zone is significantly greater in the drift excavated by blasting compared to the drift excavated by TBM. Similar observations have been reported for crystalline rock in Japan (Sugihara, 2009).

In general, it is observed that only a small number of fracture zones account for the majority of the flow of fluids in crystalline rocks. Consequently, DGRs should be developed within a relatively un-fractured, low permeability, and stable geological media to isolate the radioactive waste from conductive fracture zones. Also, non-destructive techniques should be used to characterize fracture zones, as destructive techniques such as drilling exploratory holes can become potential leakage pathways.

Some apparent differences are observed in the results from Stripa, Grimsel, Aspo, URL (Canada), and KURT projects. Perhaps these differences are due to the differences in the in situ stresses, tunnel shape, tunnel orientation, network of fractures in the rock, and excavation techniques used.

1.2.2. Salt rocks

Bedded salt formations are also under consideration as radioactive waste repositories. The response of salt rock to a stress is very complex, but a substantial progress has been made to understand the behavior of salt rock. The creep phenomenon and plastic deformation are well known mechanical responses of salt formations. Because of these characteristics, the prediction of the long-term performance of underground openings in salt rock could be challenging.

Salt formations have little flowing water that could transport the contaminants to the surface, they are relatively easy to be mined, have good heat conduction, and heal its own fractures due to its plastic behavior (Langer, 1999). The big concern is the leakage that could occur to overlying strata if the repository is breached, and fractures may also exist in the salt inter-beds. In addition, radiolysis and corrosion of the waste package could generate a significant amount of gas, producing pressure buildups that might generate fractures and establish leakage pathways.

In 1957, the National Academy of Science, in the United States, declared that the most promising storage option of radioactive waste was in salt formations. Consequently, the Waste Isolation Pilot Project (WIPP) site in New Mexico has been studied extensively to assess its suitability as a repository for radioactive waste, and has been a licensed facility since 1999. Based on the results obtained from in situ gas permeability measurements, Stormont (1997) showed that damage within a salt formation could be detected and an EDZ could be characterized. However, in 2010 the American Administration ordered the closure of the WIPP site because of strong opposition in the state of New Mexico.

In Germany, the Gorleben salt dome has been investigated for its suitability to host at depths between 840 m and 1200 m a repository for all kinds of radioactive waste (Lidskog and Andersson, 2001). A wide spectrum of geotechnical and geophysical studies have been performed to measure the deformation behavior of underground openings in the salt formation and to develop models. Also, in Germany large-scale field experiments were performed in the Asse mine to investigate the coupled THMC processes induced in geological salt formations. It was found that the healing process caused a reduction in permeability of the formation from 10^{-16} m^2 to 10^{-18} m^2 in 90 years; not full healing yet to intact rock value of 10^{-20} m^2. The healing process is the result of viscoplastic deformation and re-crystallization by presence of brine.

It is expected that radioactive waste in a salt rock repository will continue to emit radiation and thermal energy for decades after placement, resulting in a significant rise of the surrounding salt rock temperature. Liang et al. (2006) investigated the physical and mechanical characteristics of thenardite salt rock under different temperatures ranging from

20°C to 240°C. They found that both the uniaxial compressive strength and axial strain increase with temperature, whereas the tangent modulus goes in the opposite direction. The strain-softening behavior of the rock becomes increasingly evident with the increase in temperature.

Long-term performance of caverns in salt formations, where deformation can continue to develop with time (creep) and cause expansion of the EDZ, is more of a concern for the safe disposal of radioactive waste than in crystalline rocks.

1.2.3. Sedimentary rocks

The current research is more focused on argillaceous formations. They exhibit a very favorable environment for disposal of radioactive waste because of their low permeability and diffusivity, combined with a possible self-healing of fractures and a good capacity to retard radionuclide transport. A big concern is that due to the excavations and the associated THMC disturbance in the area close to the excavations, the favorable properties of such formations could change and the host rock could lose part of its barrier function. In addition, the associated de-saturation and re-saturation as well as heating of the repository system are of concern and need a detailed evaluation to assess their influence on the long-term behavior of the system.

The French Institute for Protection and Nuclear Safety has selected the Tournemire site for its own research program on deep geological disposal (Bonin, 1998). The objective of the project is to investigate the THMC processes, rock and water chemistry, and transport by diffusion and advection. The EDZs around the century-old tunnel, the nine year-old galleries, and the four year-old gallery were assessed (Rejeb and Cabrera, 2006). The Tournemire experiment shows that the excavation generates hydro-mechanical disturbances which can extend up to 6 times the mean radius of the gallery (2.5 m).

In central Japan, it was found that the size of the EDZ in the Neogene sedimentary rock at Tono mine is a function of the excavation method used. The mechanical excavation method is more effective than blasting in limiting the extent of the EDZ and change in rock mass properties (Sato et al. 2000).

Due to its low permeability and the lack of tectonically disturbed zones, the Opalinus clay at Mont Terri in Switzerland has been selected as a potential host for radioactive waste (Martin et al. 2002, Bossart et al. 2004). Several experiments have been carried out to characterize the EDZ. It was found that the characteristics of EDZ are dominated by stress-induced fractures and changing moisture conditions. Research shows that EDZ consists of an inner

zone and an outer zone. The inner zone is made of an interconnected network of unsaturated fractures connected to the excavation. The connectivity of the induced fractures in the outer zone to the excavation is marginal.

Furthermore, at Mont Terri the effects of the ventilation and re-saturation of the EDZ during the phase of repository operation and waste emplacement were assessed through in situ experiments. Numerical models were developed to simulate the short term evolution of the EDZ. Laboratory testing indicated that the behavior of Opalinus Clay is highly nonlinear at low confining stresses (Corkum and Martin, 2007). The EDZ was found to be strongly related to the existing stress field and rock anisotropy due to bedding planes (Popp et al., 2008).

Tang et al. (2002) investigated fluid flow, stress, and damage in sandstone. They found a good relationship between the loading and the flow properties along various portions of the complete stress-strain curve as shown in Fig. 1.1.
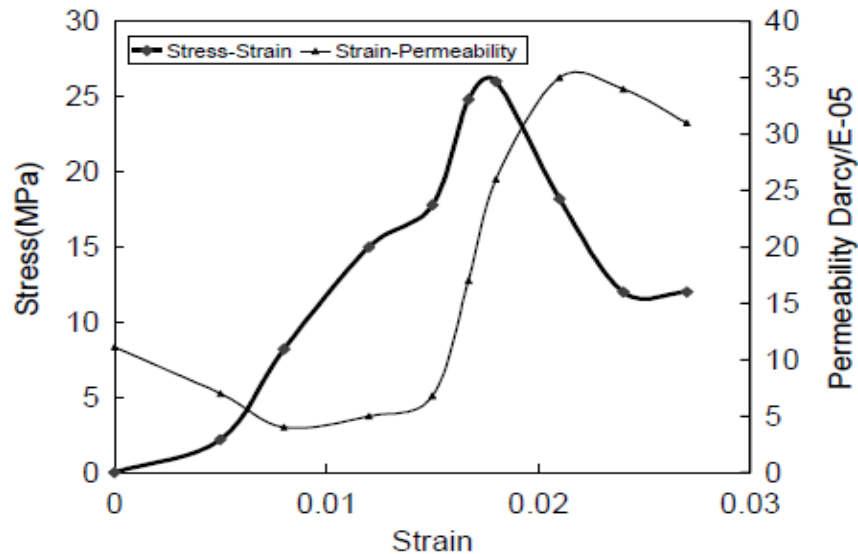
Figure 1.1. Results of triaxial tests on sandstone: relationships among stress, strain, and permeability (Tang et al., 2002).

A series of conferences, on 'Clays in natural and engineered barriers for radioactive waste confinement' were organized by ANDRA. They showed that the extent and shape of the EDZ in argillaceous rocks could be quite different from that of hard rock. Compared to hard rock, the mechanical behavior of argillaceous rocks exhibits time dependent effects. However, it seems that constitutive models applicable to hard rock could be adapted to argillaceous rocks, if one takes into account the additional time effects due to viscosity.

Depending on the mineralogical content, argillaceous rock may have some self-healing capacity (Bock et al., 2009). After backfilling and closure of DGR, the re-saturation process start and it may take years for the re-saturation process to complete. Swelling of the argillaceous rock or backfill material can lead to partial or complete closure of the developed microcracks and fractures in the rock. This process of healing may reduce the flow through the EDZ with time, and it can be an important aspect in characterizing potential host rock masses.

1.3.   EDZ initiation and evolution

The EDZ is the perturbed rock zone around an underground opening following excavation. It may create a preferred pathway for radionuclide migration, particularly in low permeability rock masses. The EDZ is controlled by the initial stress field, the material properties, the existence of natural fracture zones, the geometry of the opening, the depth of the opening, and the excavation method used. Microcracks and fractures, and in general a rearrangement of rock structures, can occur in this zone, resulting in drastic increases of permeability mainly through the excavation-induced fractures and cracks.

Developing an understanding of the initiation and evolution of the EDZ is an important aspect of a DGR development. The strategy for assessing the role of the EDZ in the DGR concept is threefold (Perras et al., 2010); i) to understand possible role in creating discrete pathways along the excavated and backfilled openings for mass transport in rock, ii) to minimize damage extent through excavation methods and geometry of excavation, and iii) to evaluate sealing methods.

It is important to note that the EDZ behavior is a dynamic phenomenon, dependent on changing conditions such as moisture, temperature, and strength degradation. Self-healing is itself a slow process, with characteristic times possibly on the order of 100 years or more. On top of these factors are the even longer term issues of chemical reactions and biological activities. All these issues make the problem a very challenging and rich field for scientific study.

Large-scale field tests, laboratory tests, and numerical modeling have been conducted to study the initiation and evolution of the EDZ. As an example, Rutqvist et al. (2009) applied different numerical approaches to model the evolution of the EDZ around a heated nuclear waste emplacement drift in fractured rock. These approaches include boundary element, finite element, and finite difference methods. The numerical results indicate that thermally

induced differential stresses near the top of the emplacement drift may cause progressive failure and permeability changes.

There are no clear rules for defining the boundary between the damaged, disturbed, and undisturbed rock mass properties. It is recognized that the EDZ is time-dependent process, and stress redistribution may lead to localized compression and swelling in the post-closure phase. For example, in the region of tangential stress concentration the maximum stress may exceed the previous overconsolidation stress and the material may behave more like normally consolidated sediment rather than an overconsolidated one (Blumling et al. 2007). In the unloaded areas, suction may attract moisture and these materials may locally swell. Hence the EDZ may experience several complex processes and the material properties may significantly alter with time.

In open literature, it is suggested that the excavation damaged zone can be subdivided into three smaller zones. The type of rock involved plays a big role in the size of each zone (McEwen 2003). As an example, a schematic view of EDZ is presented in Fig. 1.2 (Rutqvist and Stephansson, 2003).
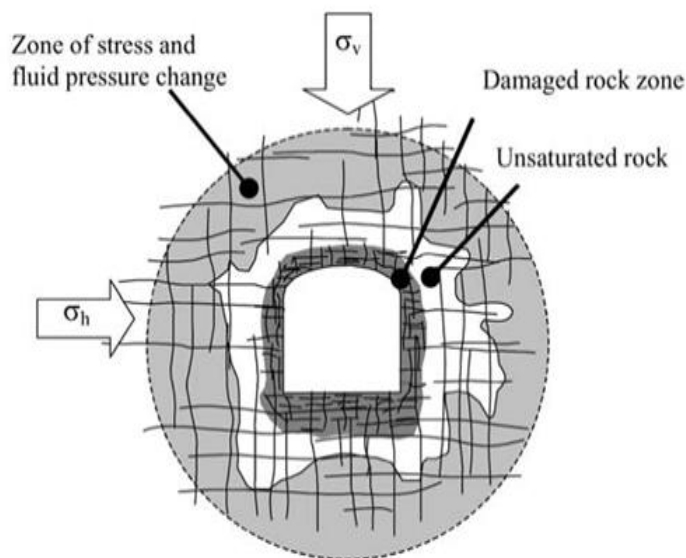
Figure 1.2. Schematic view of the EDZ around a tunnel (Rutqvist and Stephansson, 2003).

An excavation damaged zone, is usually subdivided into three different zones as shown in Fig. 1.3 (Highly damaged zone (HDZ), Excavation damaged zone (EDZ), and Excavation disturbed zone (EdZ)).
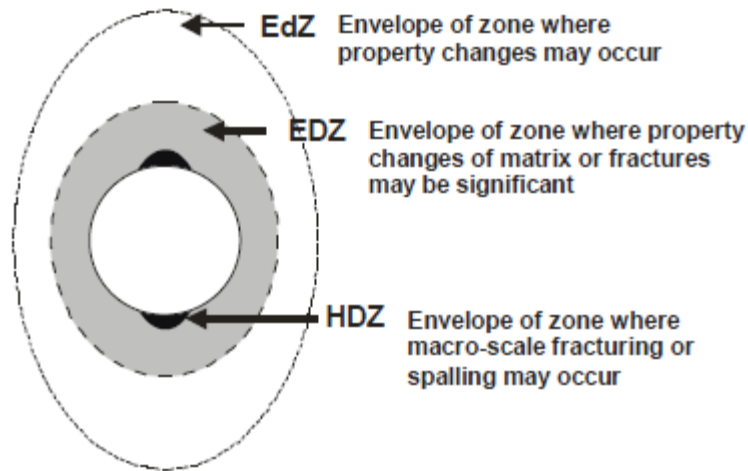
Figure 1.3. Schematic view of the EDZ (NWMO Report, 2011, DGR-TR-2011-21).

There is no an international consensus to relate the definition of the EDZ with time dependent processes, which are important for the long-term safety of a repository for geological disposal of radioactive waste (Tsang and Bernier, 2004).

In this investigation, we include the effect of time dependent processes in the description of EDZ. The EDZ initiation and evolution can be structured into three phases: the initial phase, the transient phase, and the long-term phase.

The **initial phase** corresponds to the initiation of the EDZ which alters the mechanical, hydrological, and chemical characteristics of the rock. In this phase, EDZ can be divided into three different zones as illustrated in Fig. 1.4:

- *Highly damaged zone (HDZ):* Macro-scale fractures or spalling can occur in this zone. Its permeability may increase significantly by a factor of up to 10^3 or more.
- *Excavation damaged zone (EDZ):* Hydro-mechanical and geochemical perturbations can develop in this zone. These perturbations may induce change in flow and transport properties. The permeability may increase by a factor up to 10 or more.
- *Excavation disturbed zone (EdZ):* Possible hydro-mechanical and geochemical modifications can develop in this zone without changes in flow and transport properties.
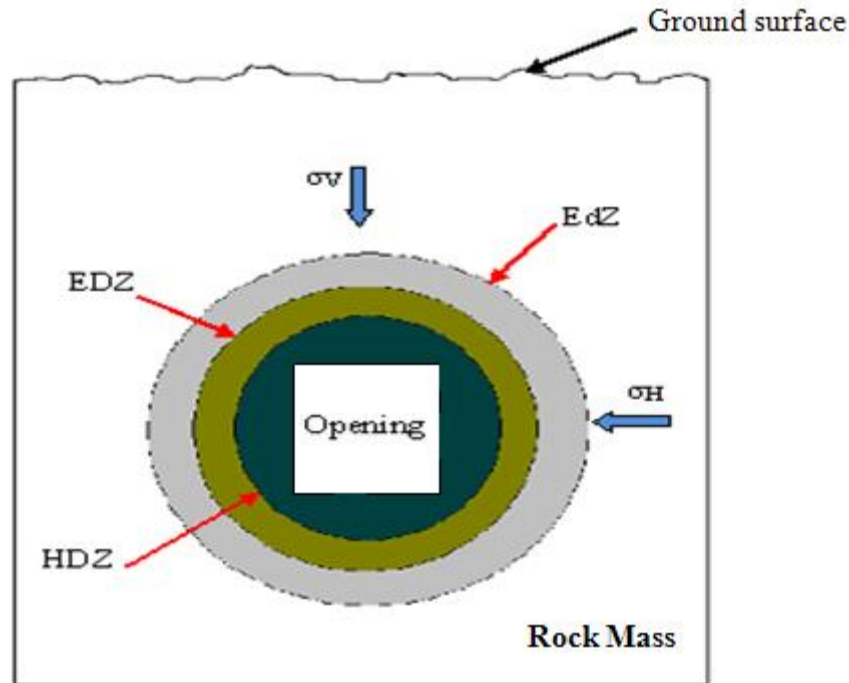
Figure 1.4. Model geometry.

The **transient phase** corresponds to the operational phase of the underground facility. During this phase, the tunnels and emplacement rooms are ventilated and exposed to the atmosphere. This will lead to de-saturation process, and de-saturation can result in the hardening of rock, creep or the formation of micro- and macro-scale fractures in the host rock surrounding the underground openings. De-saturation process can be followed by re-saturation process after the emplacement of the wastes and sealing of the rooms. Predominant processes during the transient phase include hydro-mechanical phenomena coupled with geochemical processes (principally due to oxidation).

The **long-term phase** corresponds to the post-closure phase and gradual re-saturation of the repository. Re-saturation can lead to a partial or complete closure of microcracks which were formed during the initial and transient phases. This process of self-healing is investigated within NF-PRO, Europe EURATOM Framework Program, through in situ experiments and laboratory studies on rock samples. EDZ evolution during this phase will be mainly determined by the thermal impact on the hydro-mechanical EDZ properties, geochemical changes, gas-pressure build-up, time-dependent strength degradation, and rock mass relaxation. The flow of liquids around the repository may be affected by heat generated by the radioactive waste, radiation-induced chemical decomposition, corrosion, and degassing of the groundwater. Gas would be generated as a result of slow geochemical and biological

11

reactions. The damage in the EDZ can be further accelerated by glacial loading-unloading, seismic activities, and gas pressure build-up.

The design life of a DGR can be as long as 1 Ma and the processes that can take place within the EDZ during this period of time can be summarized as follows. After the initial excavation, the repository stays open for a period of time, 10~30 years or more, for the emplacement of the waste and then is backfilled. During this period of time, the EDZ becomes unsaturated as the water flows out of the rock. It is also possible that chemical changes would take place. After closure, re-saturation process could start to take place within the EDZ. The temperature might also start rising within the EDZ depending on the type of waste. Other parameters that could affect the EDZ after closure are thermal stresses, evaporation, chemical reactions, seismic activities, glacial loading-unloading, strength degradation in rock due to aging, and pressure build-up due to gas generation.

It is possible that mineral precipitation/dissolution reactions may take place inside the existing and excavation-induced microcracks, including: 1) dissolution or precipitation of evaporate minerals, including halite and gypsum or anhydrite; 2) calcite precipitation or dissolution; 3) conversion of a limestone rock into dolomite by replacement of calcium by magnesium; 4) dissolution or precipitation of alumino-silicates; and 5) ion exchange reactions with clays may take place. These chemical reactions may seal/open the hydraulically conductive fractures, and may also influence groundwater compositions.

Investigations can be made in underground openings and/or in boreholes to characterize the EDZ. Figure 1.5 gives a summary of the factors relating to EDZ.

```
┌──────────────────┐          ┌──────────────┐  ┌──────────────┐   ┌────────────────────────────────────┐
│ Tunnel           │          │              │  │              │   │ - Rock conditions                  │
│ Geometry         │◄──┐      │              │  │              │   │ - Drilling precision               │
└──────────────────┘   │      │              │  │ Drill & Blast│──►│ - Explosives                       │
                       │      │              │  │              │   │      a) Specific charge            │
┌──────────────────┐   │      │              │  │              │   │      b) Detonation velocity        │
│ State of Stress  │◄──┤      │  Excavation  │  └──────────────┘   │ - Initiation                       │
└──────────────────┘   │      │  Method      │                     │ - Charging: Decoupling             │
                       │      │              │  ┌──────────────┐   └────────────────────────────────────┘
┌──────────────────┐   │      │              │  │ Tunnel Boring│   ┌────────────────────────────────────┐
│ Mechanical       │◄──┤      │              │  │ Machine - TBM│──►│ - Rock conditions                  │
│ Properties of    │   │      └──────────────┘  │              │   │ - Cutter head design               │
│ The Rock Mass    │   │                        └──────────────┘   │ utter head forces                  │
└──────────────────┘   │                                           └────────────────────────────────────┘
                       │      ┌──────────────┐  ┌──────────────┐   ┌────────────────────────────────────┐
┌──────────────────┐   │      │              │  │              │   │ - Survey of overbreaks             │
│ Geological       │◄──┘      │              │  │ Investigation│   │ - Observations on half barrels     │
│ Structures and   │          │ Characteri-  │  │ in Tunnel    │──►│ - Mapping of fractures             │
│ Orientation of   │          │ zation       │  │              │   │ - Surface geophysics               │
│ the Tunnel       │          │ Method       │  └──────────────┘   │ - Weir measurements                │
└──────────────────┘          │              │                     │   (Hydraulic transmissivity)       │
                              │              │  ┌──────────────┐   └────────────────────────────────────┘
        Rock Mass Response    │              │  │ Borehole     │   ┌────────────────────────────────────┐
        to Tunneling   EDZ    └──────────────┘  │ Investigation│──►│ - Macroscopic fractures            │
                                                └──────────────┘   │ - Borehole geophysics              │
                                                                   │ - Borehole hydraulic tests         │
                                                                   └────────────────────────────────────┘
```
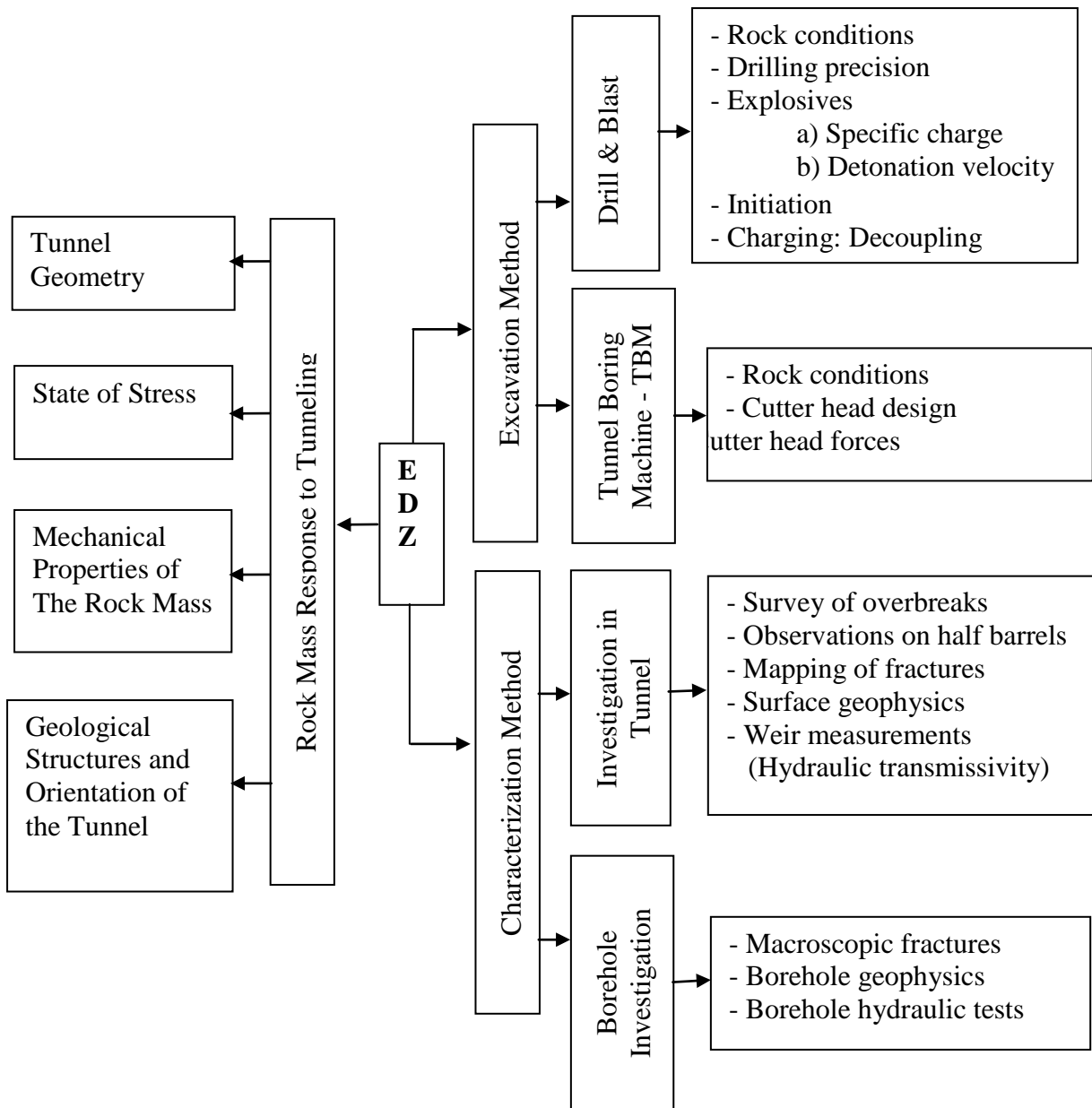
Figure 1.5. Summary of the factors relating the rock mass response to tunneling, excavation method and characterization methods (Hudson et al., 2009)

1.4. Mechanical properties of a rock mass

1.4.1. In situ stresses, rock mass strength, and rock mass strength degradation

The design of underground openings requires the estimation of in situ stresses and rock mass strength. The in situ stress state varies considerably throughout a rock mass (Martin and Chandler, 1993). The measurement of in situ stresses is difficult, but it is essential to establish the magnitude and direction of the stresses with some reasonable degree of confidence. Although over-coring and hydraulic methods are used for estimating in situ stresses, the convergence method proved to be more reliable for estimating in situ stresses at the tunnel scale (Martin et al. 1997).

The strength of a rock mass is difficult to assess. Generally, it is estimated from laboratory tests, but the samples used in the tests are of relatively small size and do not represent the rock heterogeneity. In addition, the effect of potential discrete features or discontinuities is not considered. Therefore, translating laboratory strength to field strength can be problematic. The difficulty lies in extrapolating the laboratory strength, obtained from small samples of intact rock, to account for the presence of joints, fractures, and discontinuities. On the other hand, applying in situ testing approaches for determining the strength of a rock mass is not economically feasible. Back analysis of observed failures can provide good values for large scale rock mass strength, but this works in cases in which rock mass failure has occurred.

It is well known, deep underground tunnelling causes redistribution in the stress field and, consequently, high stresses areas and damage may develop within the excavation damaged zone. The degradation in the strength properties of the material in this zone may have severe consequences, and the long-term monitoring of the variation in the strength properties is important to ensure the stability of underground structures.

1.4.2. Failure of a rock mass

Most rocks are classified as brittle materials. The elastic deformation of rocks is caused primarily by changes in intermolecular distances under applied loads. The inelastic deformation is caused by plastic deformations and the initiation and propagation of microcracks as this process can lead to the development of macroscopic fractures. The accumulation of microcracks throughout the rock mass is responsible for the nonlinear character of the mechanical response and ultimately for the failure of the rock.

The deformation and strength of rock measured in a laboratory depend on several factors. Among them are loading/strain rate, confining pressure, temperature, moisture, and mineralogical composition. The presence or absence of water affects the behavior of the rock as water appears to weaken the chemical bonds and forms films around mineral grains along which slippage can take place. Dry rocks tend to behave in brittle manner, whereas some wet rocks tend to behave in ductile manner.

Martin et al. (1999) indicated that at low in situ stress magnitudes, the failure process due to excavation in rock mass is controlled by the continuity and distribution of the natural fractures. However as in situ stress magnitudes increase, the failure process is dominated by new stress-induced fractures growing parallel to the excavation boundary.

Micro-structural changes within materials, undergoing deformation through compression, cause a reduction in various material mechanical properties (Fang and Harrison, 2002). Fig. 1.6 shows a typical stress–strain curve established by unloading and reloading a rock specimen during a triaxial compression test (Martin and Chandler, 1994). This figure clearly demonstrates that both strength and stiffness of the failing rock reduce gradually as fractures develop.
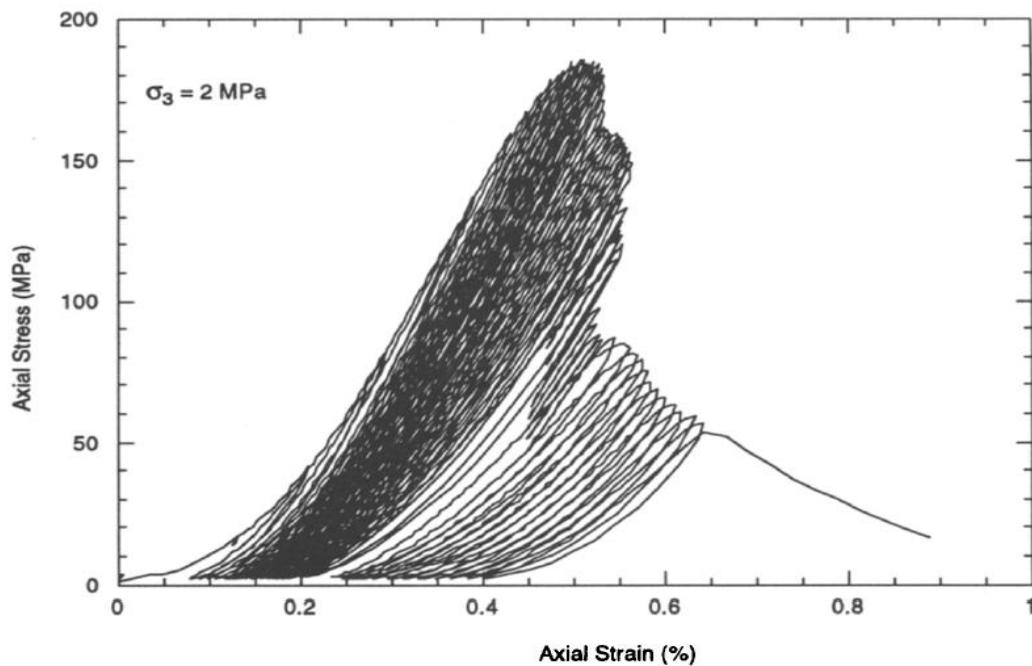

Figure 1.6. Example of the repeated loading and unloading (Martin and Chandler, 1994).

Martin and Chandler (1994) showed that the stress-strain relationship for a brittle material can be divided into five regions. Eberhardt et al. (1999) reexamined this idea as shown in Fig. 1.7. The region I represents the closure of existing microcracks. In region II, the rock is

presumed to be a linear, homogeneous, elastic material. Region III marks the beginning of dilation (stable crack growth). Region IV represents the onset of unstable crack growth. The peak strength of the material marks the beginning of the region V. Martin and Chandler (1994) showed that the initiation of new cracks and propagation of cracks start to occur at around 40% of the peak strength, and the unstable cracking starts to occur at around 80% of the peak strength for Lac du Bonnet granite.
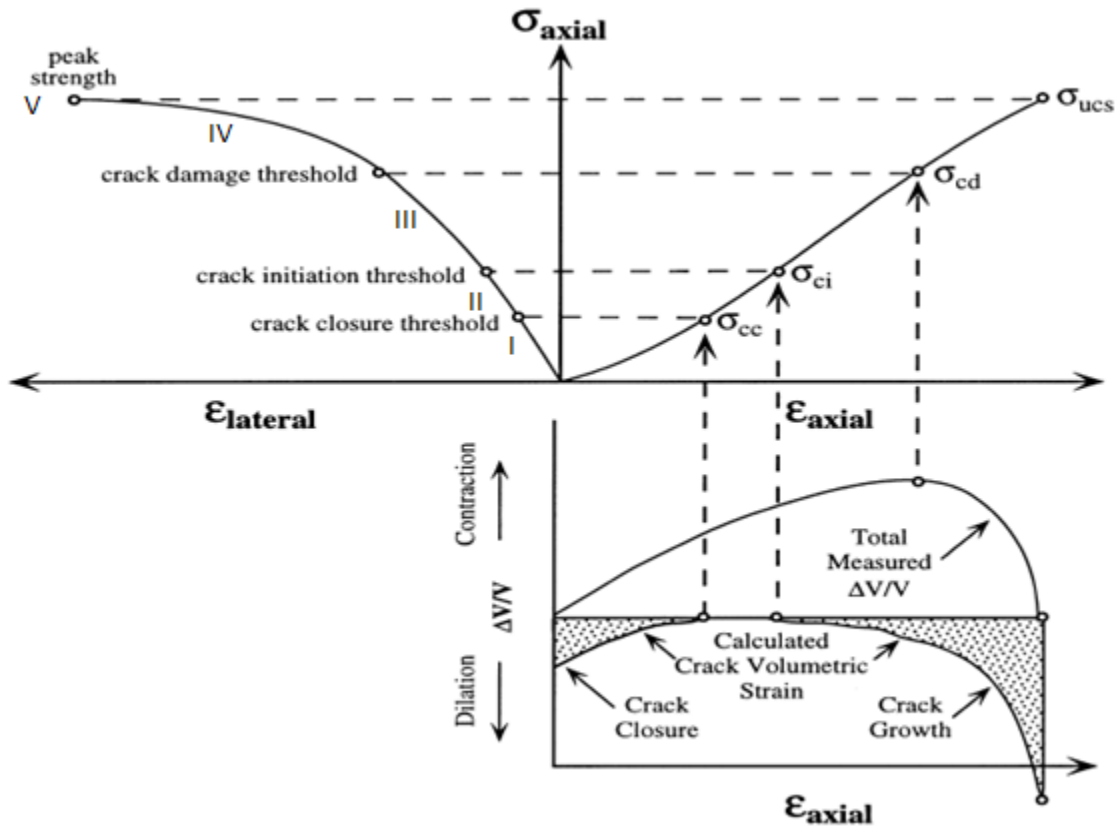

Figure 1.7. Stress-strain diagram showing the stages of crack development (Eberhardt et al. 1999).

In a mine-by-test that was designed to examine the progressive nature of brittle failure process around an underground opening in granite, Martin et al. (1997) showed that the failure process, the formation of the v-shaped notch, is linked to the tunnel face advance. The notch formation is dominated by a slabbing process that occurs at scales ranging from the grain-size to several centimetres in thickness.

During brittle failure process, Martin et al. (1999) found that the cohesion and friction are not mobilized simultaneously. Around underground openings the brittle failure process is

16

dominated by a loss of the intrinsic cohesion of the rock mass such that the frictional strength component can be ignored for estimating the depth of brittle failure.

1.4.3. Thermo-mechanical behavior of a rock mass

High temperatures are usually involved in high level radioactive waste disposal. The heat transfer within the rock mass can cause differential thermal expansion of constituent mineral grains, dehydration, and dissociation of certain minerals such as dolomite and calcite. One of the objectives of the European TIMODAZ project is to investigate the effect of thermal changes on the EDZ around nuclear waste disposal facilities (Charlier et al. 2008).

Wai and Lo (1982) investigated the strength of limestone at a temperature of about 84^oC. They found that the temperature had only a negligible effect on the strength, and the elastic modulus and Poisson's ratio were insensitive to temperature change. The effect of temperature is also investigated by Takemura et al. (2006) by submerging sandstone in hot water for hundreds of days. They found that this process causes some weathering of the rock, and also the strength and elastic properties of the rock are sensitive to temperature changes.

In the present study, only the low and intermediate level radioactive waste disposal is considered. These types of waste do not generate a lot of heat. The change in temperature in the repository will be small. Therefore, it is assumed that the temperature change will not influence the deformation and strength characteristics of the rock in our investigation.

1.4.4. Inherent anisotropy in geomaterials

Many geomaterials display inherent anisotropy which is strongly linked with the microstructural arrangement. Such anisotropy may occur in granular media, but it is most typically associated with sedimentary rocks which are characterized by the existence of bedding planes. As an example, rocks of southern Ontario are anisotropic in both deformation and strength characteristics (Lo and Hori, 1979). Some geological formations behave more anisotropically than others due to well defined bedding planes (Chappell, 1990).

Angabini (2003) investigated the deformation behaviour of an anisotropic limestone. The rock samples showed some degree of anisotropy in their elastic properties, ultrasonic velocities, grain orientation, and gas diffusion. The anisotropy was also caused by tectonic movements. Ajalloeian and Lashkaripour (2000) found that mudrocks exhibit some degree of anisotropy in compressive strength as a result of a partial alignment of plate-like clay minerals with small thickness.

Martin (1990) conducted an extensive program to characterize the far-field in situ stress states in granite. One of his findings is that major geological features, such as thrust faults, can act as in situ stress domain boundaries, and both the stress magnitudes and orientations can change when these boundaries are crossed. Also, stress relief in the form of microcracking can occur and results in anisotropy and nonlinear rock response.

Bedding planes within a rock formation can dominate the failure process depending on their spacing. The anisotropic strength can result in a less symmetrical EDZ. In the present research, the anisotropic behavior of the Tournemire argillite is investigated.

1.4.5. Creep behavior of a rock mass

Creep can damage rock fabric and may even lead to failure, and it is usually reported in terms of strain rate. Hard rock does not display significant creep under loads present in conventional engineering problems. For this rock, the dominant mechanism is microcrack generation and propagation along grain boundaries. A cumulative damaging process either stabilizes or accelerates depending on loading conditions. Salt rocks creep when subjected to any appreciable shear stress. They exhibit instantaneous strain on stress change followed by creep. Argillaceous formations may exhibit some creep especially along discontinuities and weakness planes which may be filled with different type of minerals.

1.4.6. Failure criteria

With a better understanding of the rock mass strength, it is possible to reduce instability problems that may occur due to underground excavations. The existing rock mass failure criteria are stress dependent and often include several parameters that describe the rock mass properties. These parameters are often based on laboratory tests and classification systems. One of most frequently used failure criterion in rock mechanics is developed by Hoek and Brown (HB). The increasing number of applications of this criterion to different rocks has necessitated some modifications, and new elements were introduced into the criterion (Hoek et al. 2002). In most of the cases, it is found that the criterion predicts strength envelopes which agree well with values determined from laboratory triaxial tests of intact rock, and from observed failures in rock masses. The $MSDP_u$ failure criterion (Mises-Schleicher and Drucker-Prager unified) proposed by Li et al. (2005) is also applied in a limited number of projects. This criterion encompasses many classical criteria, such as Drucker-Prager, Von-Mises, Mohr-Coulomb, etc.

1.5. Geological disposal of radioactive waste in Canada

1.5.1. Background

In Canada, the long term management of the used nuclear fuel is under the authority of the Nuclear Fuel Waste Act. The Nuclear Waste Management Organization (NWMO) was established in 2002 in accordance with the Act to assume responsibility for long-term management of Canada's used nuclear fuel. NWMO in its report to the government in November 2005 recommended the consideration of both granitic rocks and sedimentary rocks for its phased approach for the eventual geological disposal of used nuclear fuel. On June 14, 2007, the report from the NWMO was accepted by the Government of Canada for its Adaptive Phased Management (APM) for used nuclear fuel. Currently, the NWMO is under a site selection process to identify an informed and willing community to host facilities for the management of Canada's used nuclear fuel for the long term.

The Ontario Power Generation (OPG) is considering constructing a Deep Geologic Repository (DGR) for the long-term management of its low and intermediate level waste (LILW) in sedimentary rock formations of Southern Ontario at its Bruce nuclear power plant site. The Environment Impact Statement and the application to prepare site and construction have been submitted to federal governments for review.

Research in Canada on geological disposal for nuclear wastes is in a full swing at nuclear sector to bridge the knowledge gaps by funding research and characterization programs and by initiating collaborative works with the European organizations such as ANDRA in France and NAGRA in Switzerland and others. Here, we review only the design of the DGR for LILW in Ontario and the geology of the Bruce site. Figure 1.8 describes the conceptual design of the DGR which consists of a series of emplacement rooms, access tunnels, and shafts. The emplacement rooms will be excavated at a depth of 680 m within a limestone formation. The limestone is characterized with relatively high-strength and low permeability (order of $10^{-21} \sim 10^{-19}$ m^2).
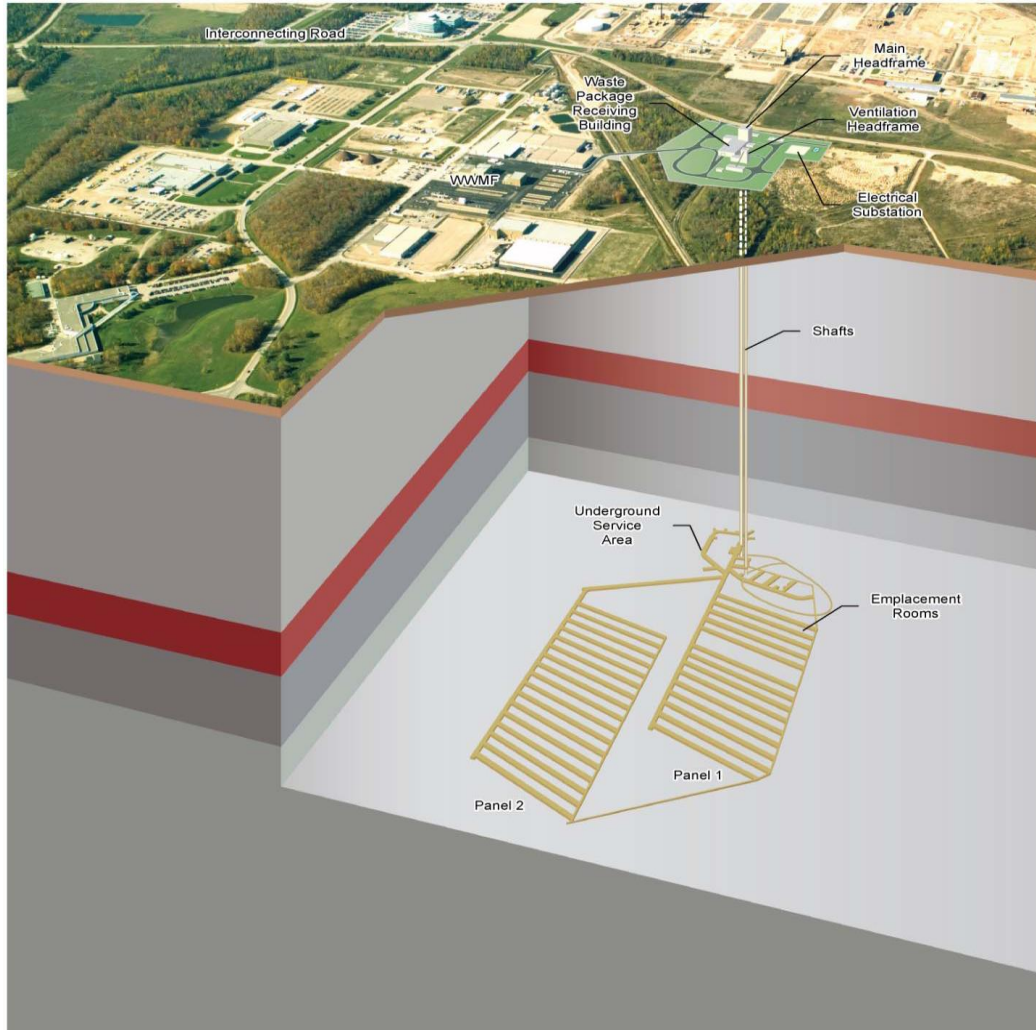
Figure 1.8. Preliminary design of the proposed DGR (OPG Report-1, 2011).

The long term performance of the geological disposal relies on robustness of multiple barriers (natural and engineered). For sedimentary rock formations of the Southern Ontario, the following attributes could provide confidence on its long term efficiency: 1) homogeneity and sufficient lateral and vertical extent of the rock mass; 2) transport of solutes is dominated by diffusion processes; and 3) stability of the geosphere for the past millions of years.

1.5.2. Geology of the Bruce site at the location of OPG DGR for the disposal of LILW

The proposed DGR for LILW will be developed within Ordovician sedimentary rock formations. These formations were formed approximately from 430 to 500 Ma ago, and possibly perturbed by nine glacial events during the latter half of the Pleistocene. The DGR will be surrounded and overlain by multiple layers of low permeability sedimentary rocks. The layers of sedimentary rocks were formed within the depression of the Michigan basin. The groundwater at the level of the repository is saline (>200 g/L). A cross-section of the Michigan basin showing the rock formations is given in Fig. 1.9. The types of rock include carbonates, shale, evaporate and sandstone which are located above the Pre-Cambrian crystalline basement rock.
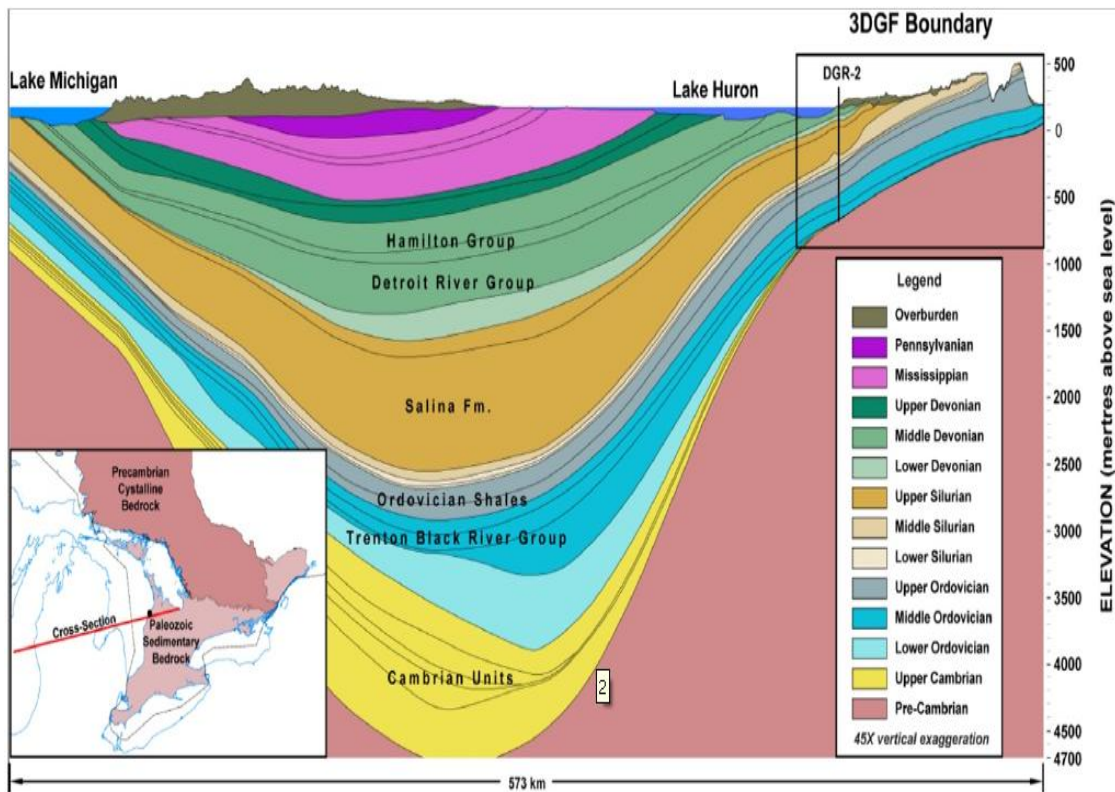
Figure 1.9. Rock formations of Michigan basin (OPG Report-1, 2008).

Field investigation has been done and several boreholes are drilled. Rock formations observed in borehole DGR2 at the Bruce site are shown in Fig. 1.10. The repository will be located in the Cobourg limestone.

Ontario is located in the Mid-Plate stress province and is characterized by high horizontal compressive stresses (Adams and Bell, 1991). This behavior is due mainly to regional tectonic activities and past glaciations. The existence of high horizontal stresses in many sedimentary and shield rocks of Ontario have been well documented; e.g., Lo (1978) and Lee (1981). Based on the regional data (Gartner Lee Limited, 2008), at the level of the repository the ratio $\sigma_H/\sigma_v = 1.7$ to 2.5, while the ratio $\sigma_h/\sigma_v = 1.0$ to 1.2 (Fig. 1.11). The orientation of the maximum horizontal stress in the Michigan Basin appears to be in a NE to ENE direction.
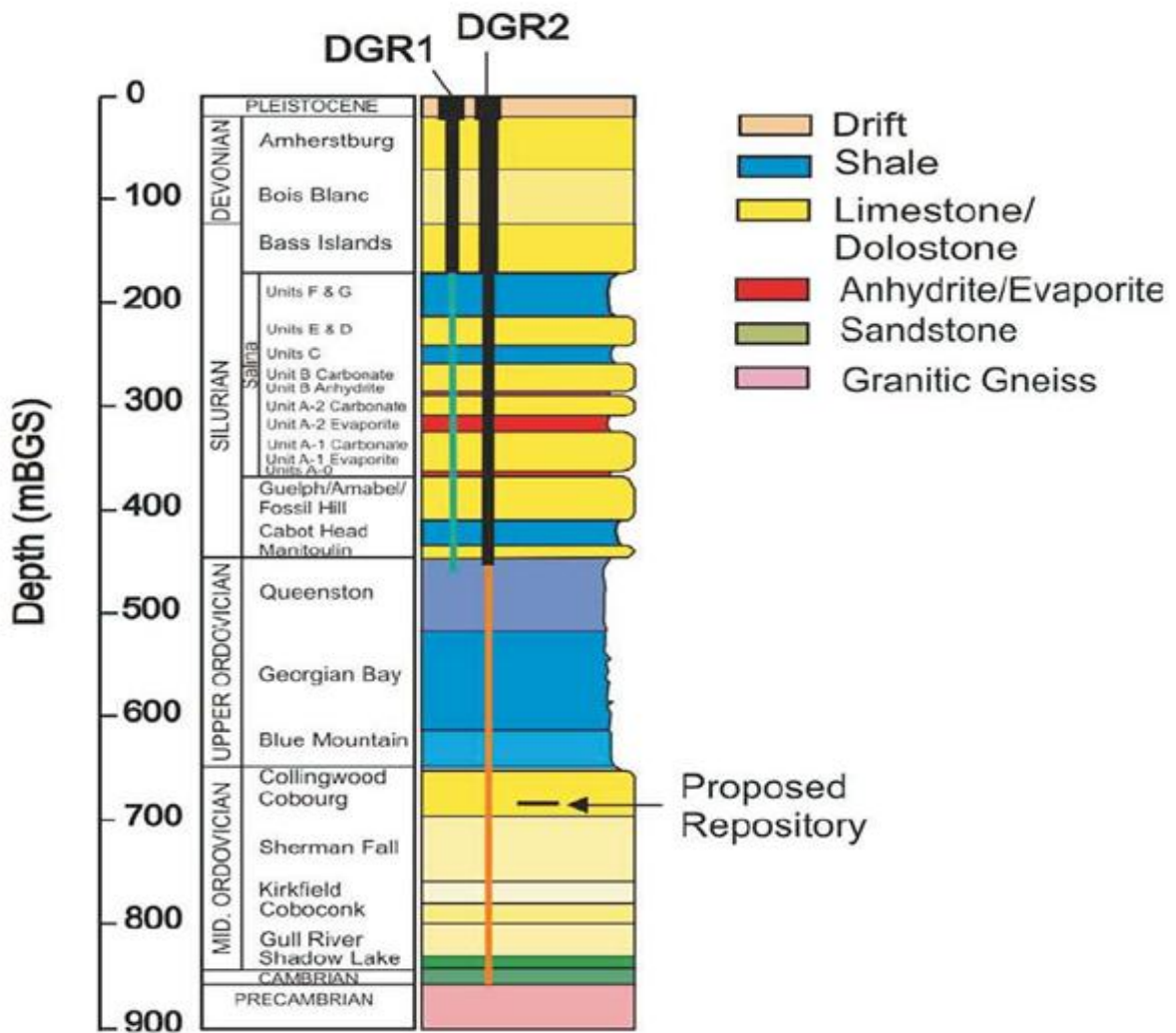
Figure 1.10. Rock formations observed in borehole DGR2 (OPG Report-1, 2008).
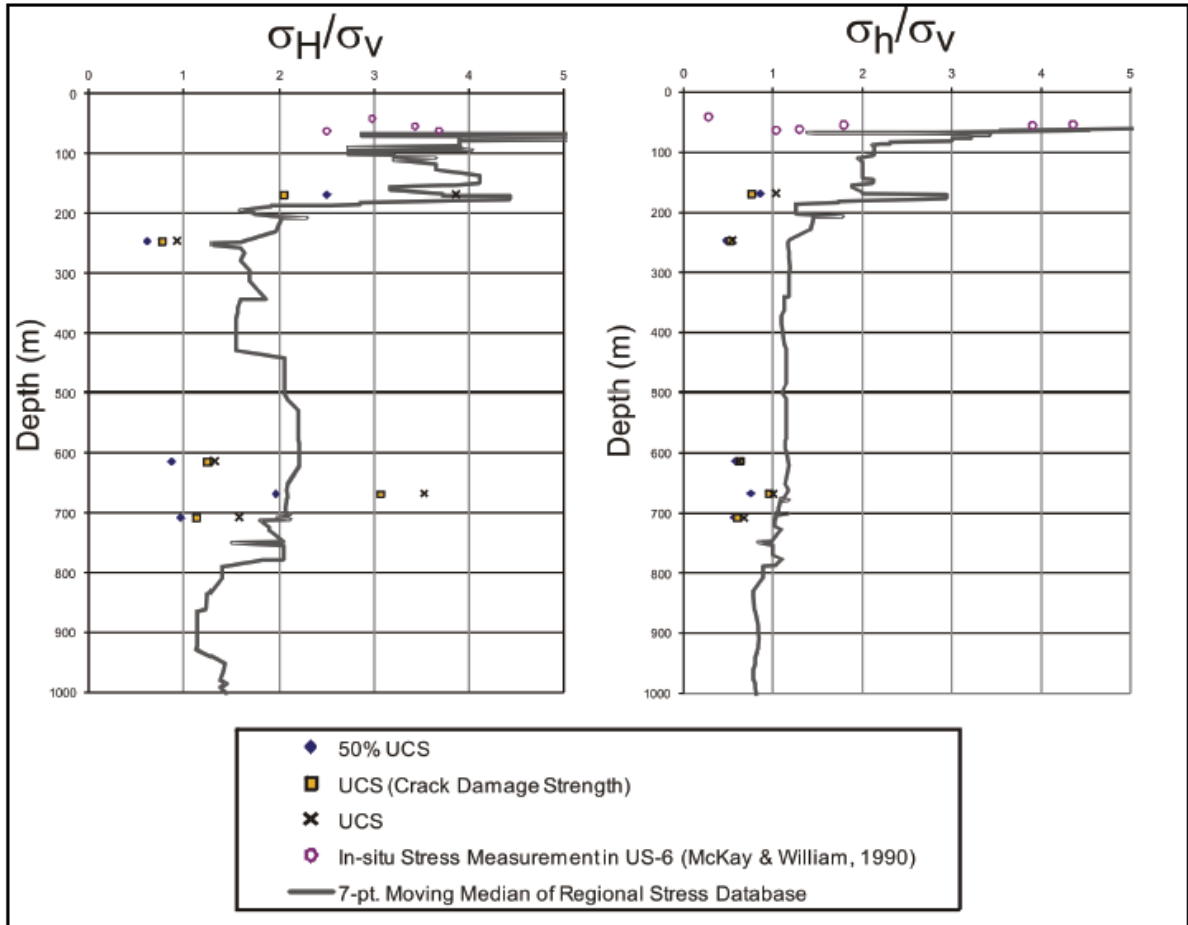
Figure 1.11. In-situ stress ratios based on far-field regional data using the moving median technique (from OPG Report 2008e).

Part 2

A laboratory investigation on the mechanical behavior of Tournemire argillite

2.1 Background

A laboratory test program to investigate the mechanical behavior of the Tournemire argillite was designed and carried out at CANMET Laboratories in Ottawa, Canada. The Tournemire argillite is characterized by the presence of closely spaced bedding planes. Eighty (80) rock samples were obtained from seven boreholes drilled at different angles in the walls and floor of an existing gallery at the site of Tournemire Underground Research Laboratory (URL), France. The experimental program includes the measurements of basic physical properties of the argillite and its mechanical response under uniaxial compression tests, triaxial compression tests with various confining pressures, unconfined and confined cyclic tests, Brazilian tests, and creep tests.

At the location of sampling, the in-situ stresses were estimated to be: minor horizontal stress (σ_h) = 2.1±1.0 MPa, major horizontal stress (σ_H) = 4.0±2.0 MPa, vertical stress (σ_v) = = 3.8±0.4 MPa (Rejeb and Tijani, 2003). Thus, confining pressures of 0, 4, and 10 MPa were used for triaxial testing in the present investigation. A displacement rate of 0.03 mm/min was used to load all specimens and kept constant during testing, except for the Brazilian tests that were carried out with a loading rate of 3.4 kN/min. Rock specimens were loaded at different inclinations with respect to bedding planes (i.e. $\theta=0^o$, 30°, 45°, 60°, and 90°). Acoustic Emission was also recorded to detect the initiation and propagation of microcracks during the uniaxial compression tests. All tests were performed at the natural moisture content of samples as delivered to CANMET Labs.

The main objective of the testing program is to obtain the mechanical properties of the transversely isotropic material of the Tournemire argillite and to establish and validate a constitutive model for the argillite. This Part 2 describes the geology of the Tournemire site, the general layout of the URL, the mineralogy and hydraulic/geotechnical properties of the argillite, the testing program, and the experimental results.

2.2 Description of the Tournemire Site

The Tournemire site is located in a Mesozoic marine basin on the southern limit of the French Massif Central (Fig. 2.1). Sedimentary formations of this basin are characterized by three main Jurassic layers: a 250 m thick nearly horizontal layer of argillite and marls of Toarcian and Domerian age, located between two aquifer limestone and dolomite layers of Carixian and Aalenian age (Barbreau and Boisson, 1993; Boisson et al., 1997). The

Tournemire massif has faults and fractures, and water flow takes place along lower and upper limestone aquifers. The Tournemire argillite is characterized by the presence of closely spaced bedding planes dipping at 4° towards the North, and contains randomly distributed fractures.

X-ray diffraction analysis of the argillite showed that the mineralogical composition consists of 55% of clay minerals, 19% quartz, 15% calcite and 11% of other minerals such as dolomite, pyrite, siderite, and feldspars (Schmitt, 1994). The porosity of the argillite varies between 6% and 9% and its density is about 2550 kg/m^3. The natural moisture content varies between 3 and 5%. The permeability of the argillite is very low and estimated to be 10^{-21} ~ 10^{-22} m^2 (Matray et al., 2007). The porewater pressure, measured in various vertical and horizontal boreholes, varies between 0.2 and 0.6 MPa (Rejeb and Cabrera, 2006; Matray et al., 2007). The measurements of P-wave velocity indicate a coefficient of anisotropy around 2.16.
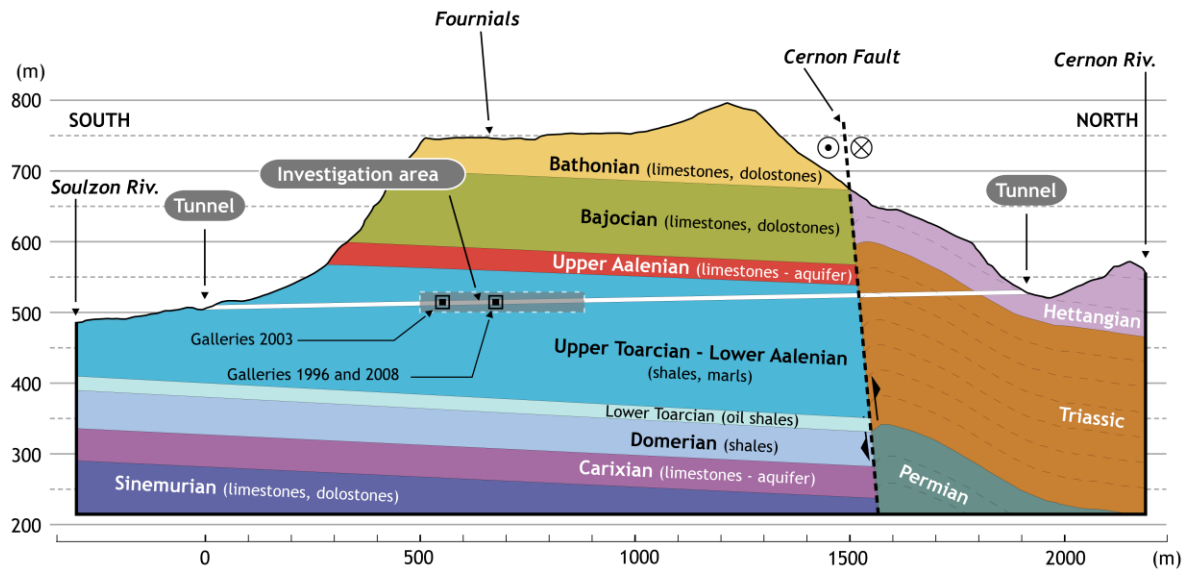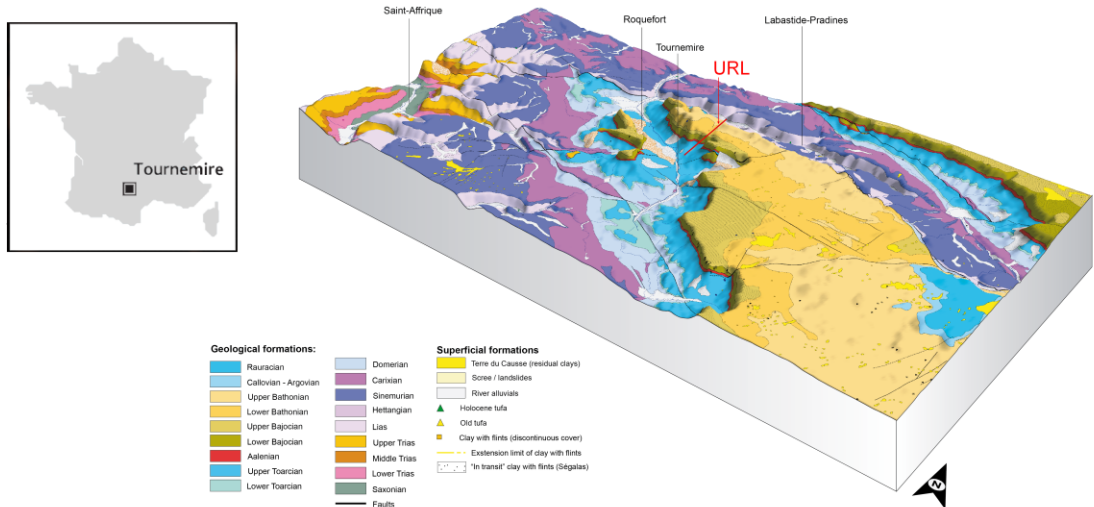
Figure 2.1: The Tournemire URL: location and geological environment (top); Geological cross section along the URL (bottom)

2.3   General layout of the URL and boreholes

Figure 2.2 provides a general view of the URL in Tournemire. It consists of a century-old tunnel, the sixteen year-old east and west galleries, the nine year-old east and west galleries, the four year-old north, south, and west galleries, and the four year old niche. The century-old tunnel is about 2 km long and 250 m deep. Rock specimens were obtained from Gallery South_08 and Gallery West_08. As shown in Figures 2.2 and 2.3, the drilling (sampling process) was carried out at different angles (θ) with respect to bedding planes: parallel (boreholes M13 and TD4M, θ=0°), perpendicular (boreholes M8 and M9, θ=90°), and three

27

intermediate inclinations (borehole M12, $\theta=30^o$; borehole M11, $\theta=45^o$; and borehole M10, $\theta=60^o$).
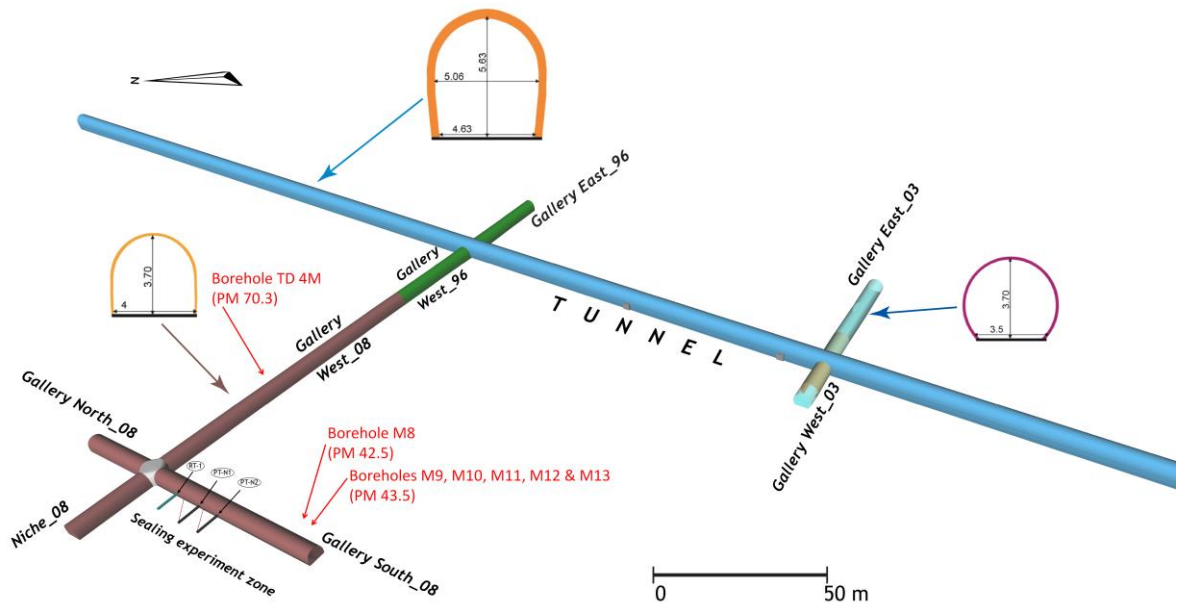
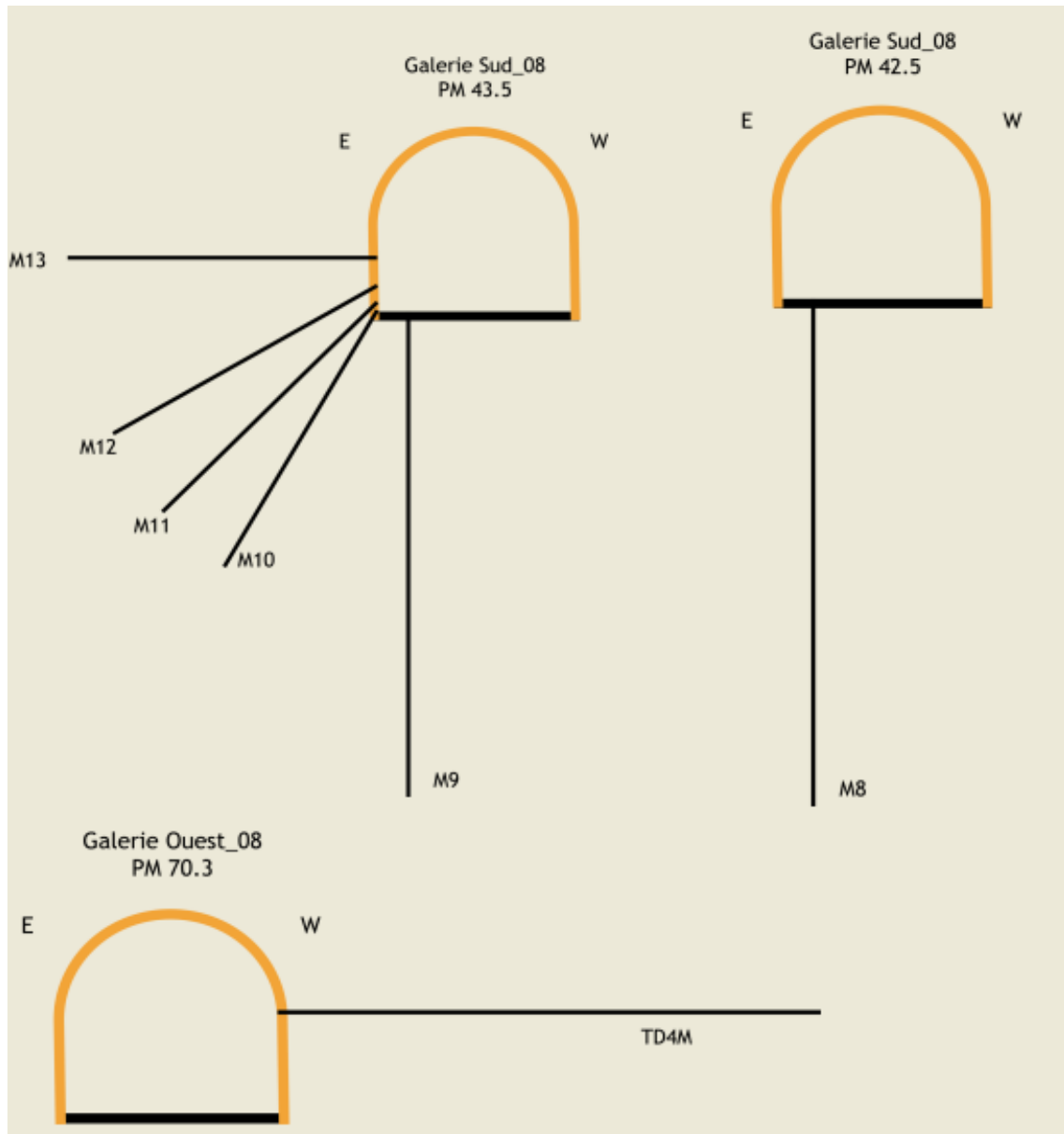Figure 2.2: General layout of the Tournemire URL

Figure 2.3: General layout of the boreholes: M8, M9, M10, M11, M12, M13, and TD4M.

2.4 Description of testing equipment and test specimens

The testing equipment consists of an MTS rock mechanics system, Model 815 (Fig. 2.4), with linear transducers to measure the axial displacement, a chain extensometer to measure the circumferential displacement at the center of the test specimen, transducers to measure pressures, and a data acquisition module. A detailed description of the MTS system is reported in Labrie and Conlon (2008). Acoustic emissions were recorded through a

measuring system developed by Physical Acoustics Corporation (PAC) which was operated simultaneously but independently from the main MTS.

Cylindrical argillite specimens of 61.3 mm in diameter and 133 mm in height were used for uniaxial, triaxial, cyclic tests, and creep tests, consistent with the specifications of the ASTM Standard for the preparation of test specimens (ASTM D4543). Specimens with the same diameter and a nominal length of 40 mm were used for Brazilian tests. Usual ASTM procedures (C496 and D3967, with 3-mm wood inserts at platens) were used in the Brazilian tests.
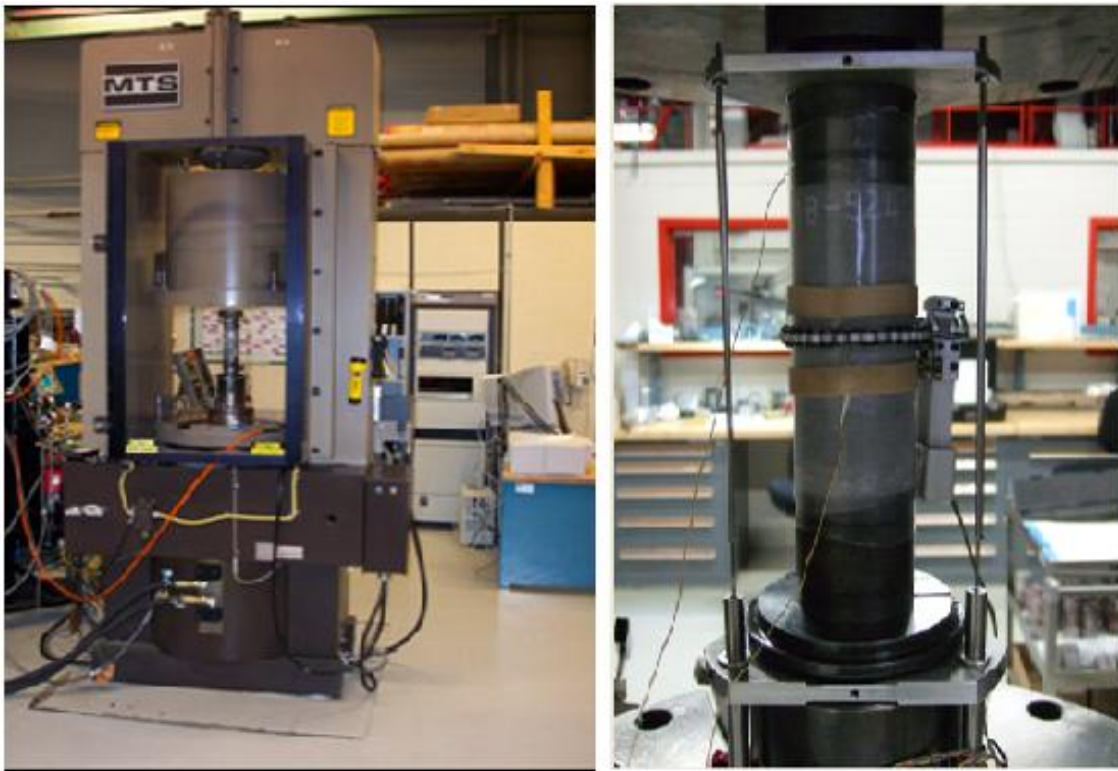
Figure 2.4: MTS Rock Mechanics Testing System.

2.5 Testing Program

In addition to the measurement of basic physical properties of the argillite such as the moisture content, density, porosity, and P-wave velocity, the following tests are also carried out at CANMET Laboratories (Table 2.1). Acoustic Emission was recorded to detect the initiation and propagation of microcracks during the uniaxial tests. The results of the creep tests are described and analyzed in Part 5.

Table 2.1: Description of the tests conducted at CANMET Labs. NOTE: The definition of θ is provided in Fig. 2.5.

LOADING ORIENTATION	DESCRIPTION OF THE TEST	BOREHOLE NUMBER	CONFINING PRESSURE (MPa)	ACOUSTIC EMISSION
$\theta=0^o$	Three uniaxial tests	M13	0	Yes
	Two triaxial tests	M13	4 and 10	No
	One cyclic test	M13	0	Yes
	One cyclic test	M13	10	No
	Three Brazilian tests	M13, TD4M	na	na
	One creep test	M13	0	No
$\theta=30^o$	Three uniaxial tests	M12	0	Yes
	Two triaxial tests	M12	4 and 10	No
	One cyclic test	M12	0	Yes
	One cyclic test	M12	10	No
	Two Brazilian tests	M12	na	na
	One creep test	M12	0	No
$\theta=45^o$	Three uniaxial tests	M11	0	Yes
	Two triaxial tests	M11	4 and 10	No
	One cyclic test	M11	0	Yes
	One cyclic test	M11	10	No
	Two Brazilian tests	M11	na	na
	One creep test	M11	0	No
$\theta=60^o$	Three uniaxial tests	M10	0	Yes
	Two triaxial tests	M10	4 and 10	No
	One cyclic test	M10	0	Yes
	One cyclic test	M10	10	No
	Two Brazilian tests	M10	na	na
	One creep test	M10	0	No
$\theta=90^o$	Three uniaxial tests	M8, M9	0	Yes
	Two triaxial tests	M9	4 and 10	No
	One cyclic test	M9	0	Yes
	One cyclic test	M9	10	No
	Three Brazilian tests	M8, M9	na	na
	One creep test	M9	0	No

2.6   Description of experimental results

Before proceeding with the presentation of results, the orientation angle (θ) should be defined. The loading orientation, θ, is the angle between the vertical axis (z), representing the direction of the major principal stress, and the x′ axis which is parallel to the bedding planes (Fig. 2.5). For example, $\theta=90^{o}$ means the major principal stress is perpendicular to the orientation of bedding planes, and $\theta=0^{o}$ means the major principal stress is parallel to the orientation of bedding planes. In this paper, the term 'depth' represents the distance of the sample within the borehole from the borehole collar.
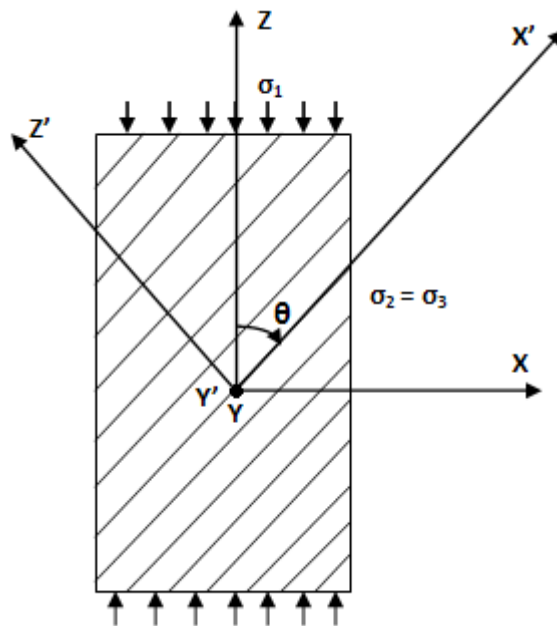
Figure 2.5. Loading orientation with respect to bedding planes.

2.6.1   Basic properties of the Tournemire argillite

The following properties were determined from laboratory experiments. The moisture content of the rock specimens is 3.86% with standard deviation (std) equal to 0.078, the bulk density is 2550 kg/m^3 (std=0.0244), the porosity is 9.52% (std=0.211), and the coefficient of anisotropy, based on P-wave velocity measurements is 2.16.

2.6.2   Acoustic Emission data and mobilization of strength parameters

Acoustic Emission (AE) data is used for detecting the initiation and propagation of microcracks in rock specimens under mechanical loading. The intensity of microcracking is assumed to depend on the number of recorded AE events (Hits). A typical "AE Signature" for an oven dry specimen of Tournemire argillite is shown in Fig. 2.6 (uniaxial test). In this figure, one of the horizontal axes represents the elapsed time during testing. "Parametric 1(Volts)" axis provides a measure of the applied load and "Hits" represents the number of AE events. The loading of the specimen starts at point A and proceeds towards point B. In this particular experiment, all AE events between points A and B are related to microcrack closer. Once these microcracks are closed, they do not propagate for some time during the loading. For that reason, there are not many AE events recorded between the points B and C. Starting at around point C, the number of hits increase significantly until the stress level reaches to its maximum value at point D. For the purpose of developing a constitutive relation, it would be possible to follow the approximations illustrated in Figure 2.7.

1. The material resistance to applied load between points A and C (shown in Fig. 2.6) can be based mainly on cohesion. In this part, there is a small amount of frictional resistance because of the existing microcracks in the material before testing. For additional AE events to take place either new microcracks to develop or the opposing surfaces of propagating microcracks (fractures) to slide against each other causing micro-tremors (AE event).

2. Between points C and D, both the cohesive resistance and frictional resistance are active. In this part, the rate of increase in cohesive resistance is decreasing and the rate of frictional resistance is increasing rapidly (see Fig. 2.7a).

3. After point D (peak strength), it is assumed that there is no cohesion left in the sample and only the frictional resistance between the opposing surfaces of fractures supports the applied load. In addition to the confining pressure, the presence of Teflon sleeve holding the fractured specimens together becomes an important factor in the apparent behavior of rock specimens in the post-peak regions. For example, if there was no

Teflon sleeve, the specimen in a uniaxial unconfined compression experiment would fall apart completely without any AE events after the peak strength.

The Tournemire argillite has a high clay content (55%) which makes this rock to behave less brittle than a hard rock. Considering all experimental AE data, new microcracks start to develop approximately at a stress level σ_{ci} = 70% ~75% of the peak strength (σ_{ci} =crack initiation stress). At a stress level above σ_{ci}, the development and propagation of microcracks accelerate with the increase in stress level. In addition, according to the observations made in the present experimental data, the crack damage stress level (σ_{cd}) as defined by Martin (1993) is reached approximately at a stress level of σ_{cd} = 85% ~ 90% of the peak strength.

For the Tournemire argillite the inelastic straining starts to develop at the beginning of the stress-strain curve as a result of the closure of the existing fissures and bedding planes. The experimental data suggest that the mobilization of strength parameters under increasing axial strain can be approximated as shown in Fig. 2.7 (a). The values of the mobilized strength parameters are influenced by the loading orientation angle θ and the confining pressure. In summary, upon loading the specimen, the mobilized cohesion starts to increase very rapidly with the increase in axial strain. The rate of increase in the mobilized cohesion tends to slow down when the stress level increases beyond σ_{ci} (Point C). The mobilized cohesion reaches a maximum value at the peak strength. However, as the axial strain increases beyond its value corresponding to the peak strength, the cohesion reduces rapidly to a negligible value. On the other hand, the mobilized friction angle is small at very low stress levels. Initially, the rate of its increase is also slow. When the stress level increases beyond σ_{ci}, the increase in the mobilized friction angle becomes large and its value reaches a maximum value at the peak strength. In the post peak region, the frictional resistance becomes the only component of the post-peak strength of the rock specimens tested.
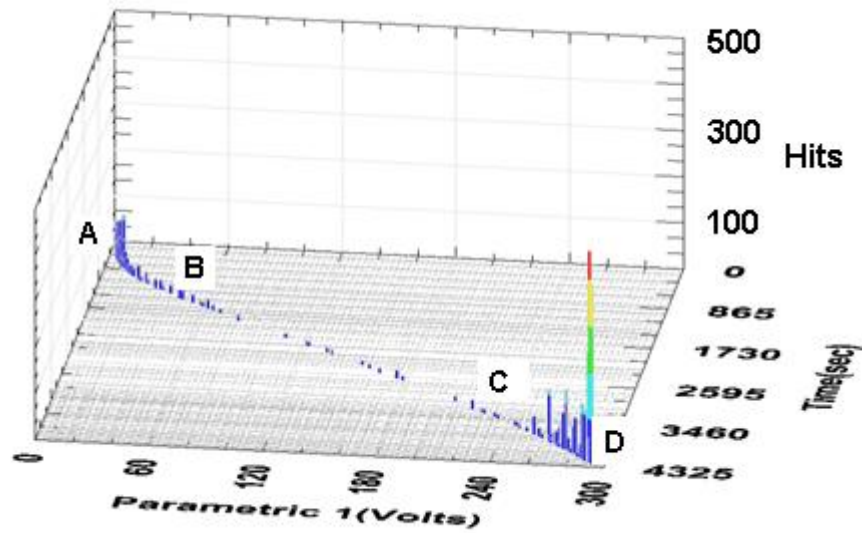
Figure 2.6. AE signature for a uniaxial test.

(Note: AE results shown in Fig. 2.6 were obtained from an oven dry specimen. The trends in the AE results for the specimens tested at their natural water content were similar except that the number of hits was almost ten times less than those for the oven dry sample.)
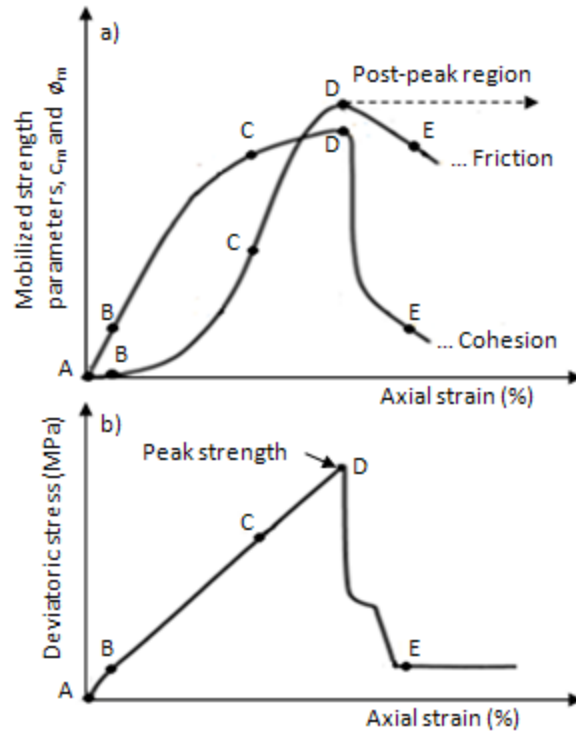
Figure 2.7. Mobilized strength parameters: a) c_m and ϕ_m as a function of axial strain, b) A typical stress-strain curve for the Tournemire argillite.

2.6.3   Brazilian indirect tensile tests

Brazilian tests were carried out on fifteen specimens obtained from different boreholes (M8, M9, M10, M11, M12, M13, and TD4M) at a depth ranging from 3.55 m to 7.4 m measured from the top of boreholes. The experimental results are given in Fig. 2.8. Brazilian tests showed consistent results with small dependence on loading orientation, θ. Each data point on Fig. 2.8 represents the average of three tests. The average tensile strength is around 5-5.5 MPa.
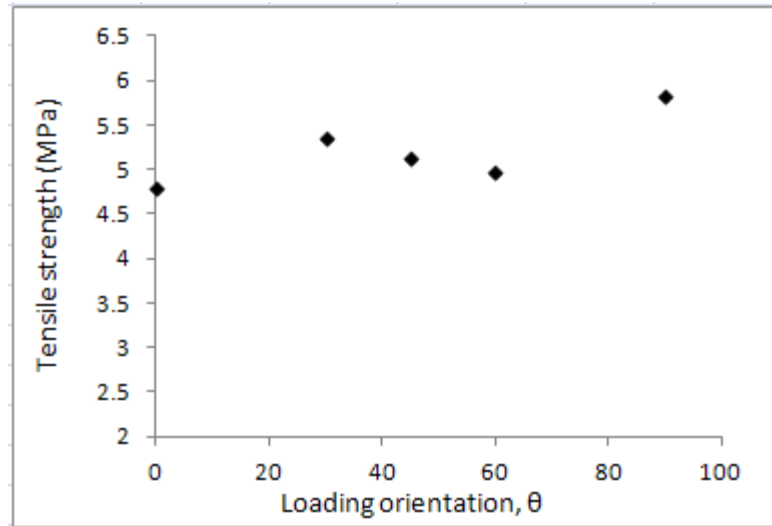
Figure 2.8: Variation of the tensile strength with loading orientation, θ.

2.6.4 Uniaxial and triaxial tests

Uniaxial compression and triaxial compression tests were carried out on specimens, which were obtained from depths ranging from 3.55 m to 6.85 m. The loading orientations considered are $\theta=0^{o}$, 30°, 45°, 60°, and 90°. Confining pressures (σ_c) of 4 MPa and 10 MPa are applied in triaxial tests. Typical stress-strain curves are shown in Figs 2.9 and 2.10 for all loading orientations and confining pressures. In Fig. 2.9, all curves first show hardening behavior and then softening behavior. The peak deviatoric stress, peak axial strain, volumetric strain, and post-peak behavior are influenced by the confining pressure and loading orientation angle, θ. The volumetric strain is mainly contraction up to the peak strength where a sharp transition to dilation occurs due to rapid formation and propagation of microcracks as also evidenced by AE data. The Tournemire argillite can be classified as a brittle material. A sudden collapse of the material, e.g. moving quickly from peak strength to minimum post-peak strength, is observed in both uniaxial and triaxial compression tests. In Fig. 2.10, for the test with $\theta=90^{o}$ and $\sigma_c=$ 10 MPa, a fracture is developed within the upper part of the specimen, above the middle section of the sample. As a result, the actual value of the volumetric strain after the peak strength is not captured by the instrumentation.
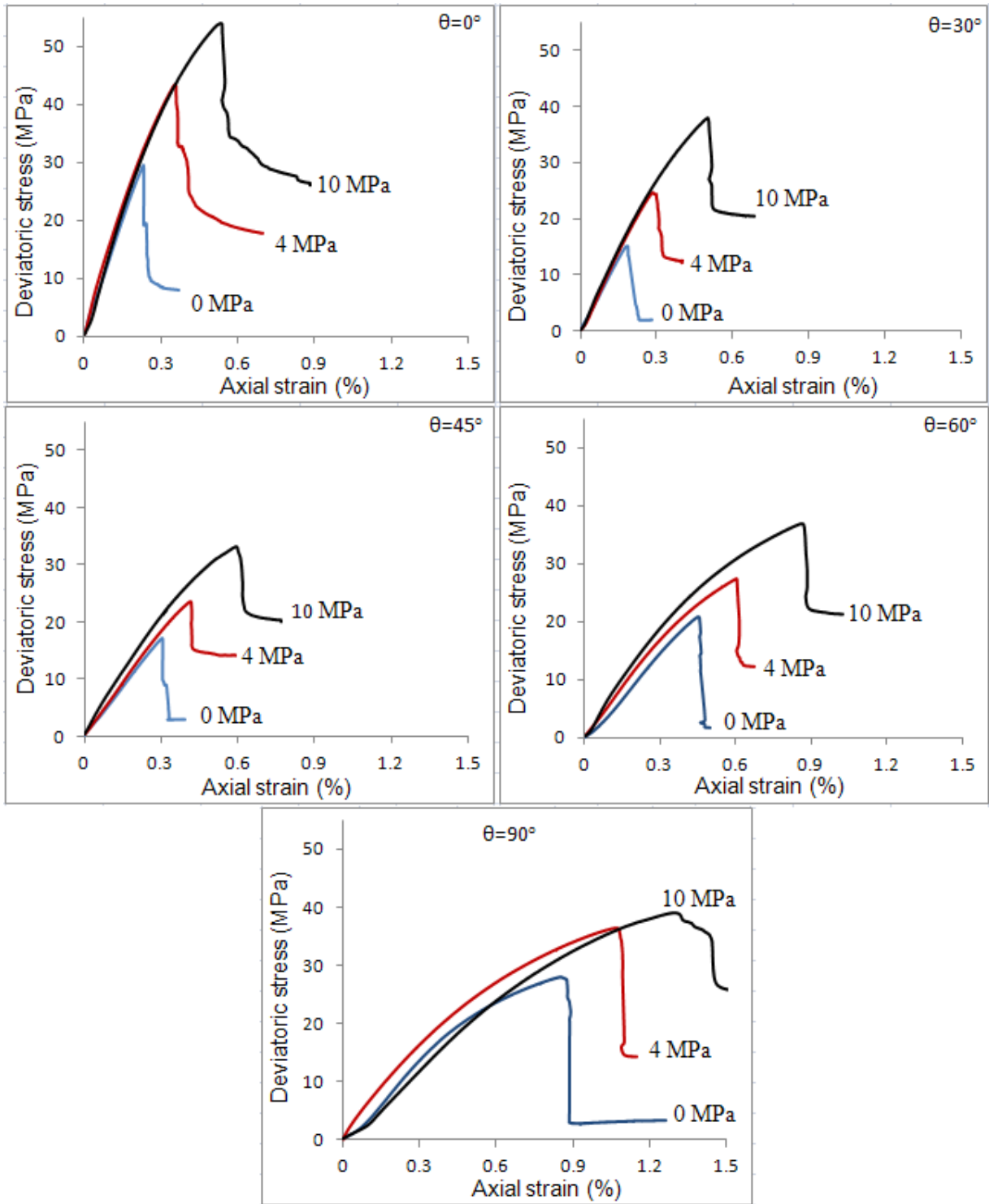
37

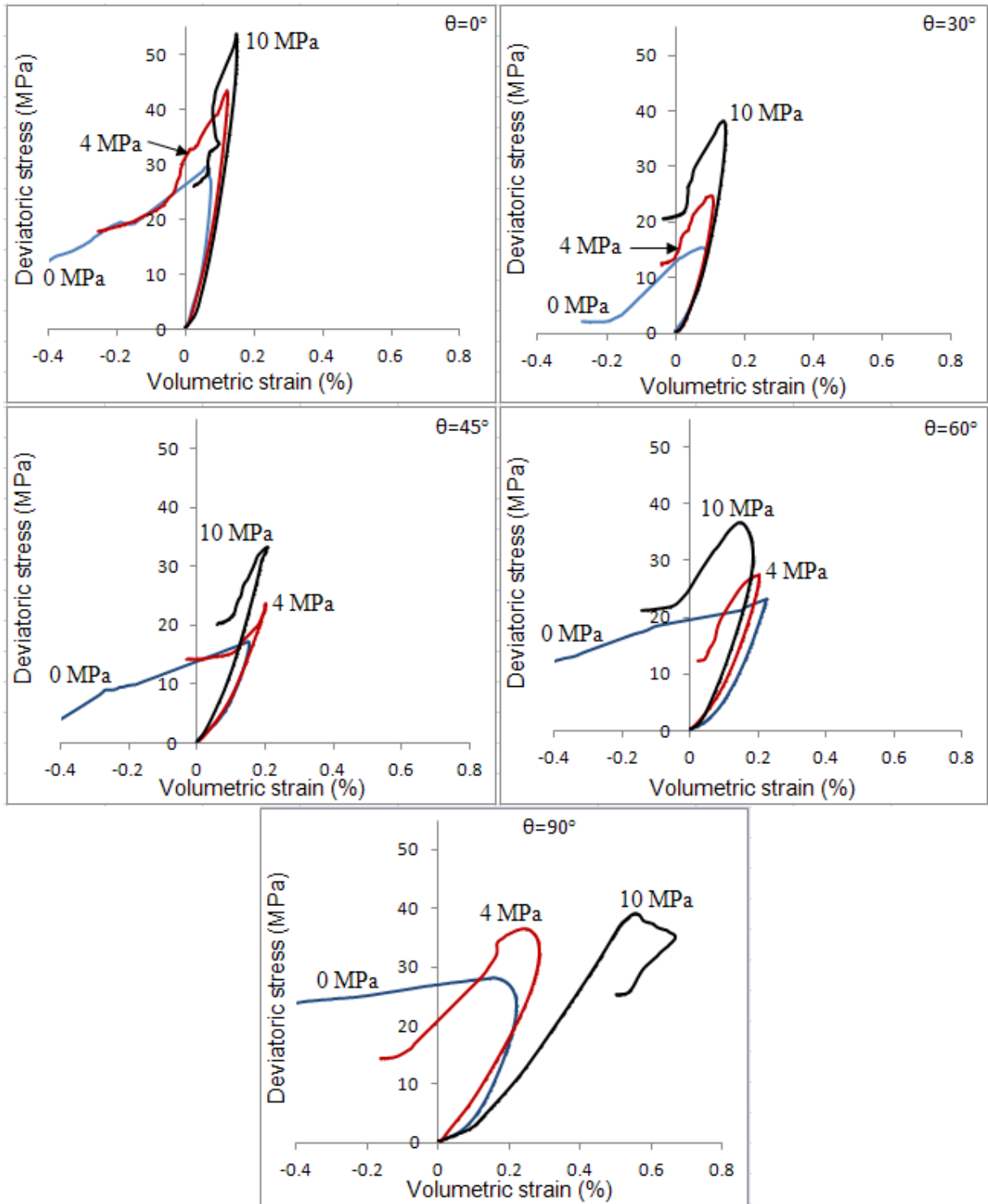Figure 2.9. Deviatoric stress-axial strain curves for various values of θ and confining pressures σ_c.

Figure 2.10. Deviatoric stress-volumetric strain curves for various values of loading orientation, θ and the confining pressure σ$_c$.

2.6.5   Unconfined and confined cyclic compression tests

Unconfined and confined cyclic compression tests were carried out on specimens obtained from depths ranging from 2.2 m to 5.75 m. Five different loading orientations are considered; $\theta=0^{\circ}$, 30°, 45°, 60°, and 90°. A confining pressure of $\sigma_c=10$ MPa was applied in the confined cyclic tests. The main objective of running these cyclic tests was to investigate the cyclic behavior of the Tournemire argillite and to determine whether the development of plastic strains would cause some degradation in the stiffness of the material.

Typical stress-strain curves are shown in Figs. 2.11 and 2.12 for unconfined cyclic compression tests, and in Figs. 2.13 and 2.14 for confined cyclic compression tests. In most experiments, the unloading-reloading cycles were imposed at various stress levels before the peak strength was reached. There were also a few cyclic tests conducted, whenever it was possible, in the post-peak region. The number of cycles varied from one test to another. For a given loading-unloading cycle, a strain rate was used to set the upper limit of the cycle and a pre-determined stress value was used to set the lower limit of the cycle. In some tests, the data was not captured completely after the peak by the MTS machine as in the case for $\theta=0^{\circ}$.

The experimental data indicate that the cyclic behavior of the material depends on whether cycling is done before or after the peak strength. Cycling before the peak strength resulted in the following observations:

- More plastic strain develops within the specimen with each additional cycle. The amount of plastic strain varies between $\frac{1}{3}$ and $\frac{1}{2}$ of the total strain, and depends on θ and σ_c.
- The degradation of the Young's modulus increases with the increase in plastic strain. The degree of degradation depends on θ and σ_c.
- Each cycle of loading and unloading causes more contraction in the specimen.

It is observed that the loading orientation θ has strong influence on the size, number, and orientations of fractures that can develop within the specimen before the applied stress reaches the peak strength. After the stress level reaches the peak strength, the specimen breaks into two or more blocks. The cyclic behavior of the material after the peak strength is controlled by the fracture/fractures produced. Each additional cycle results in more sliding of one block on another and more dilation of the specimen.

In this small number of experiments with a limited number of load cycles and loading range, it was observed that the load cycling has no significant effect on the strength of the material. Also, the failure mode of the material is not affected by load cycling. Important hysteresis was observed in these tests. The hysteresis phenomenon may be the result of viscous

properties of the argillite. The compressibility-dilatancy transition occurs near the peak strength as in uniaxial tests. The plastic strain is anisotropic as indicated by the results.
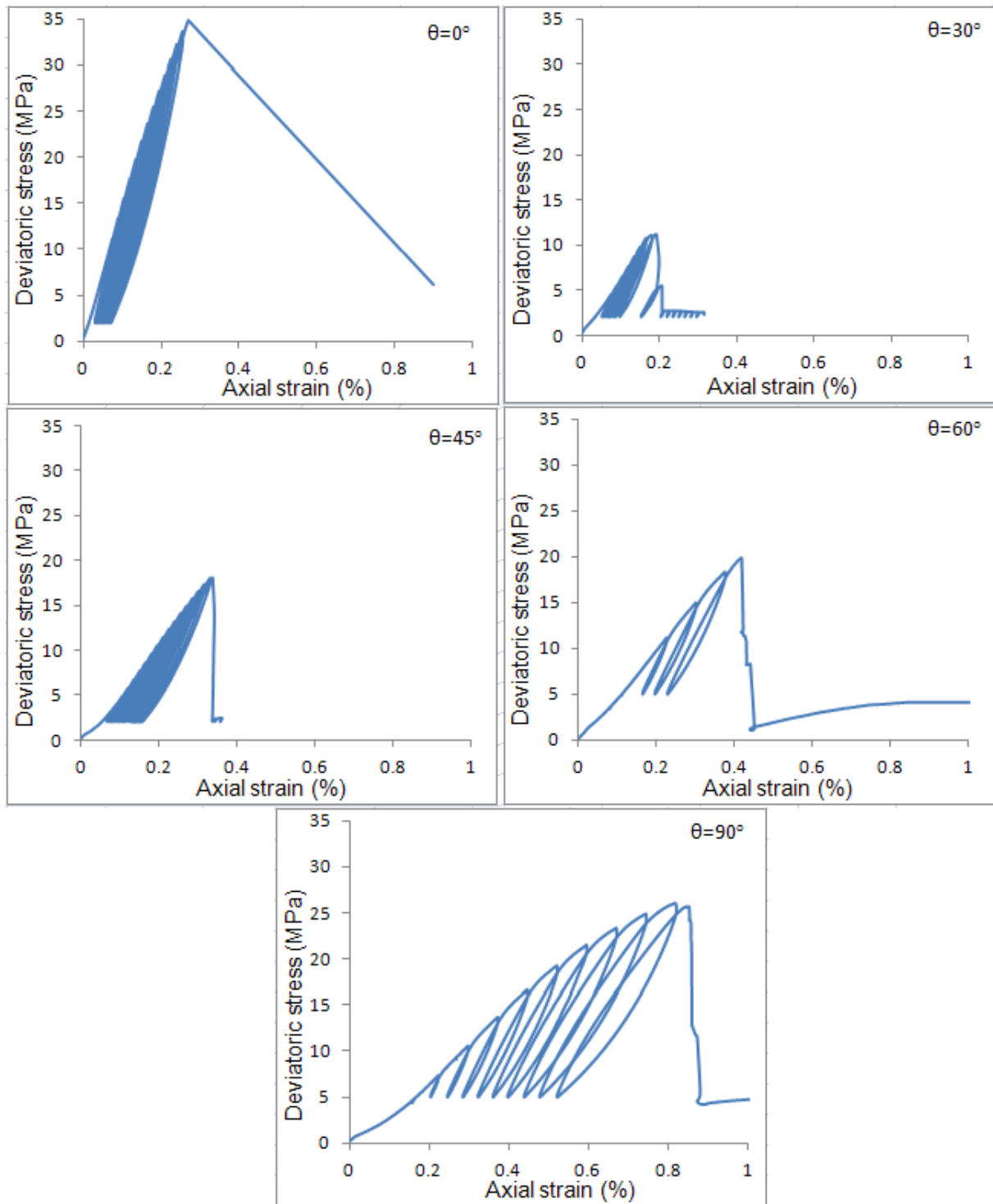

Figure 2.11. Deviatoric stress-axial strain curves for various values of θ (unconfined tests).
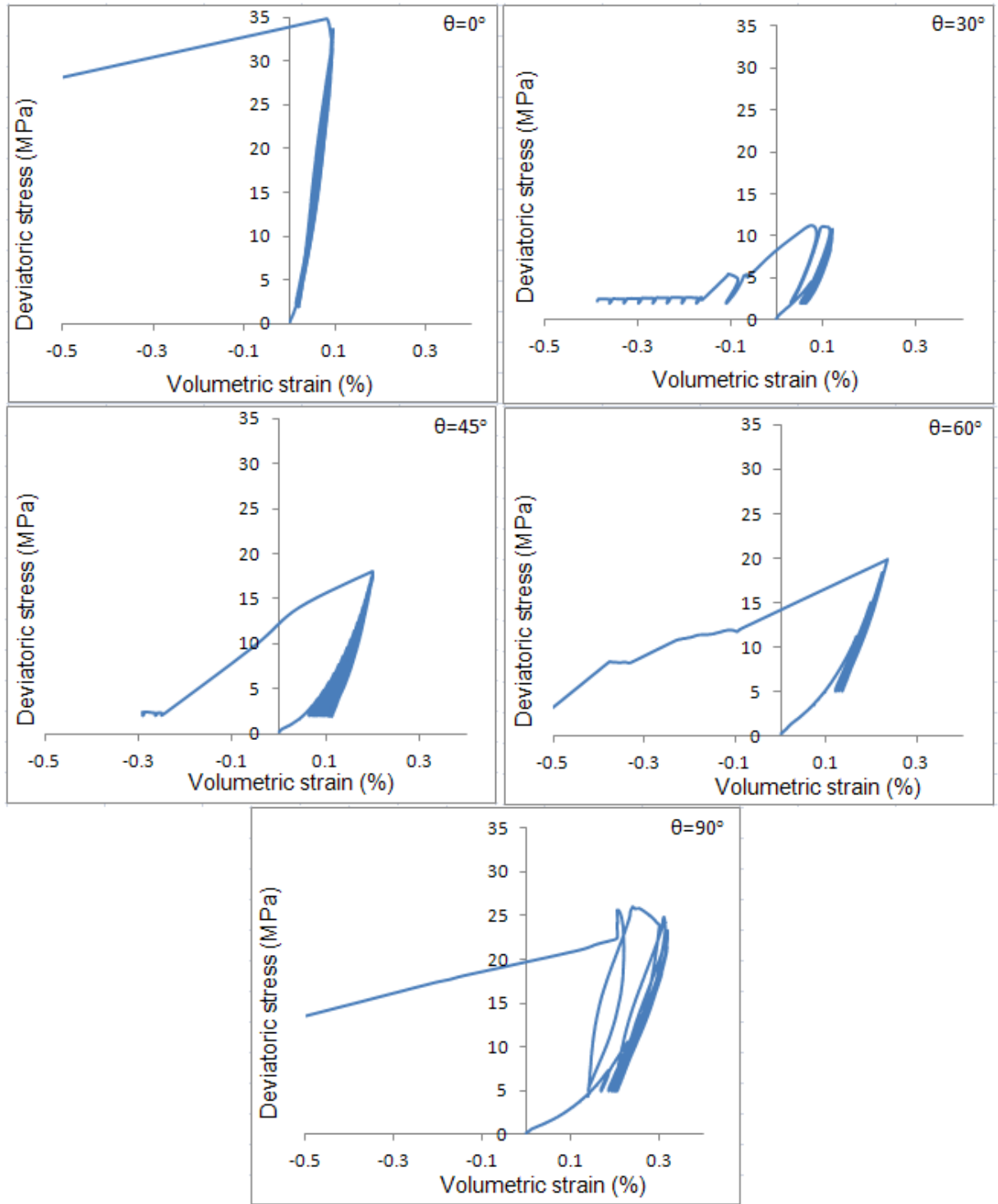
Figure 2.12. Deviatoric stress-volumetric strain curves for various values of θ (unconfined tests).
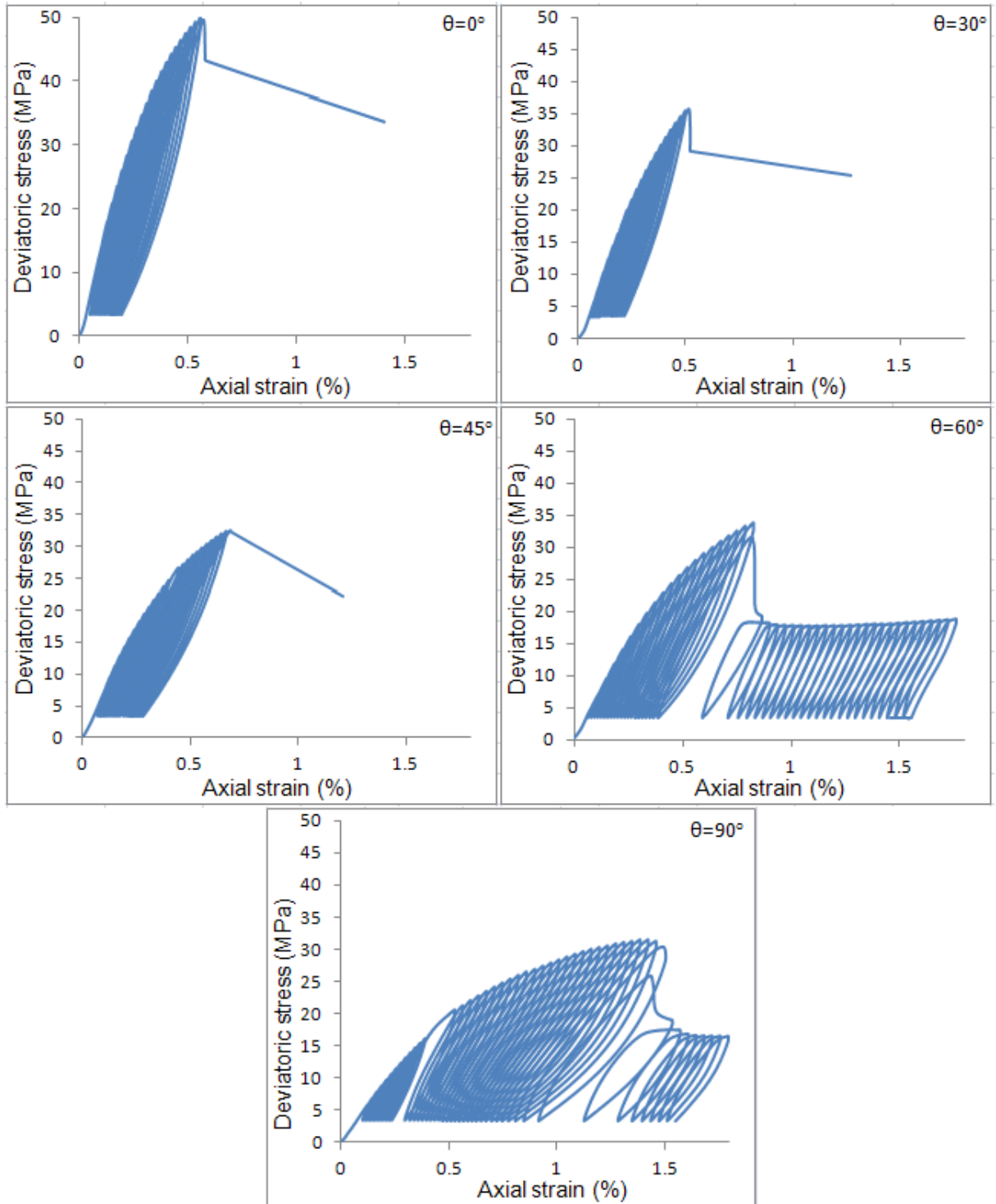
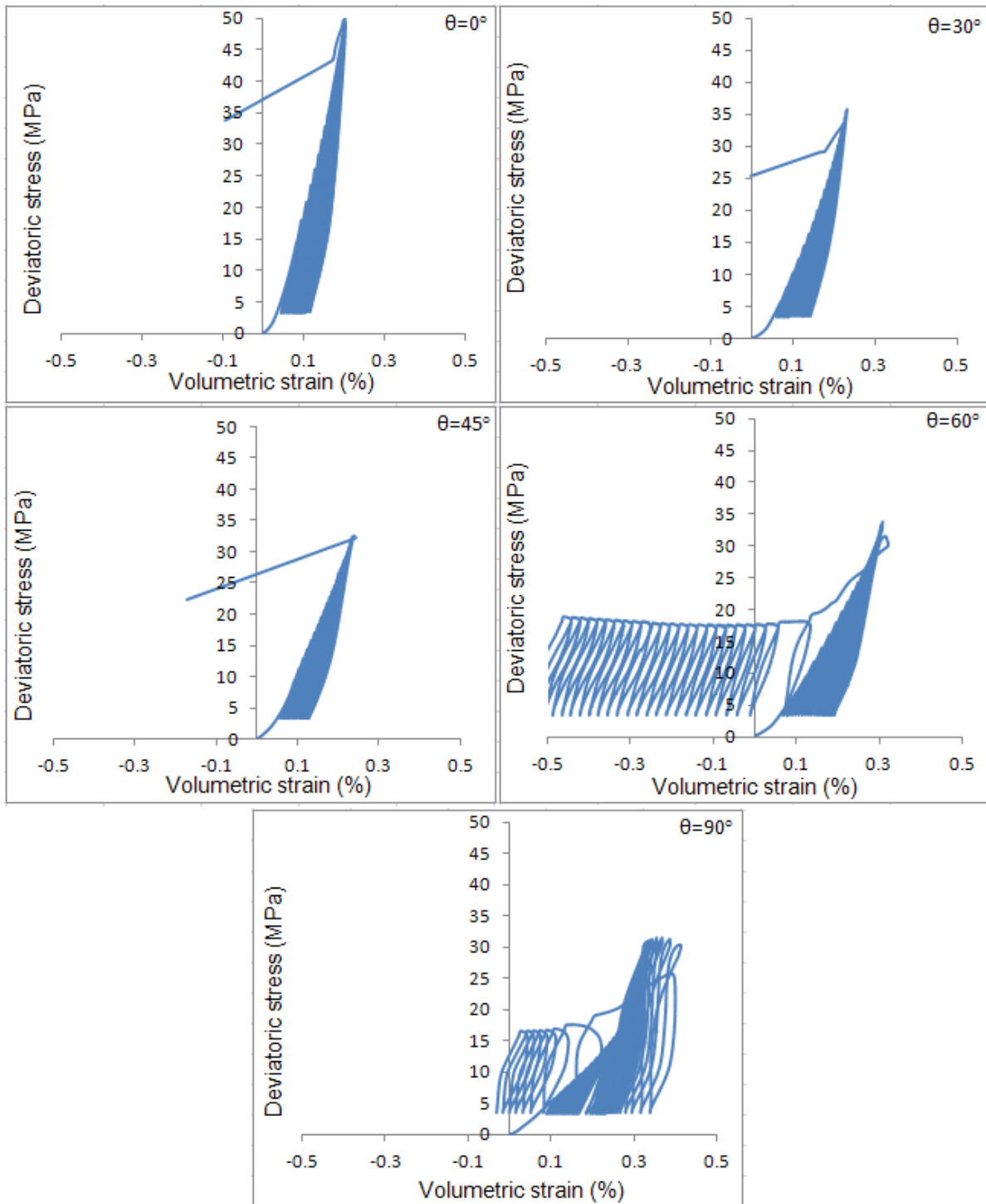Figure 2.13. Deviatoric stress-axial strain curves for various values of θ (confined tests, σ_c=10 MPa).

Figure 2.14. Deviatoric stress-volumetric strain curves for various values of θ (confined tests, σ_c=10 MPa).

2.6.6 Laboratory investigation of the creep behavior of the Tournemire argillite

Five uniaxial tests with strain increments have been performed at CANMET Labs to investigate the creep behavior of the Tournemire argillite. The specimens, 61.3 mm in diameter and 133 mm, used in this testing program were obtained from five different boreholes drilled at different angles with respect to bedding planes as described in Part 2. The standard for preparation of test specimen and testing equipment are also described in Part 2. Five different loading orientations are considered ($\theta=0^{o}$, 30°, 45°, 60°, and 90°), and the depth of the specimens vary from 4.7 m to 5.55 m. A constant displacement rate of 0.03 mm/min is maintained during loading.

In each test, first the axial strain is increased to a predefined axial strain level followed by a 1-hour period of waiting time in which the deviatoric stress is kept constant and the axial strain is measured. After, the axial strain is increased to another predefined level followed by a 1-hour period of waiting time in which the deviatoric stress is kept constant and the axial strain is also measured. This process is repeated until the failure state is reached. Deviatoric stress-axial strain and axial strain-time curves are shown in Figs 5.1 and 5.2 for all loading orientations.

It is indicated in Part 2 that for the Tournemire argillite the formation of new cracks (stable crack growth) and the crack damage level (unstable crack growth) occur at stress levels of about $\sigma_{ci} = 70\%$ ~ 75% of the peak stress and $\sigma_{cd} = 85\%$ ~ 90% of the peak stress, respectively. It appears the results of the creep tests can be analyzed in terms of σ_{cd}. If the deviatoric stress is below σ_{cd}, only a small increase in axial strain is measured during the creep period before a stable state is reached. When the deviatoric stress exceeds the σ_{cd}, the increase in axial strain during creep period becomes more significant. After 1 hour period of waiting time, the axial strain is still developing and this could be due to unstable crack growth under constant stress. At this stress level, a longer period of creep might cause the failure of the material. Compared to the results of uniaxial tests (Part 2), larger axial strain is measured at peak in creep tests.
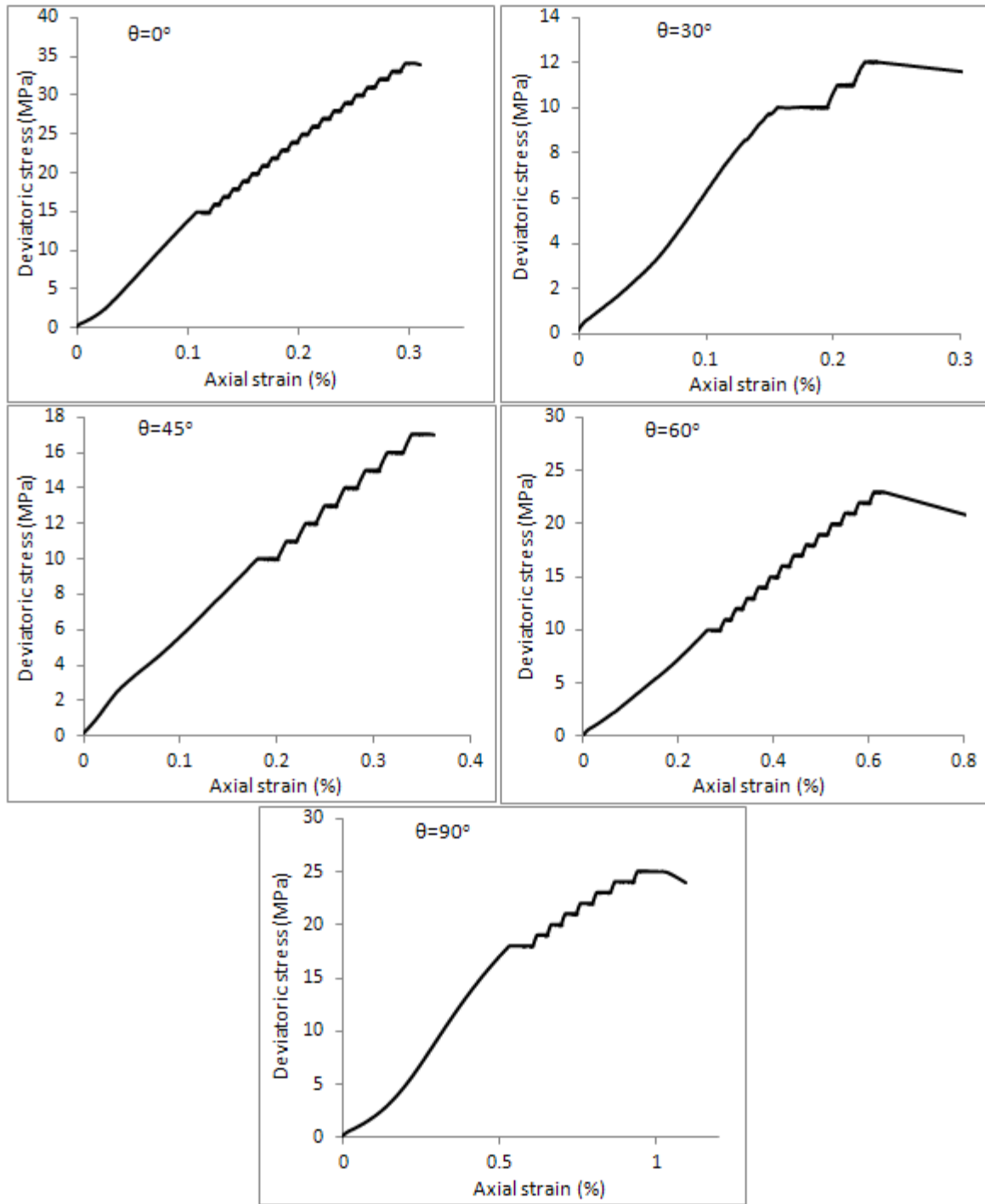
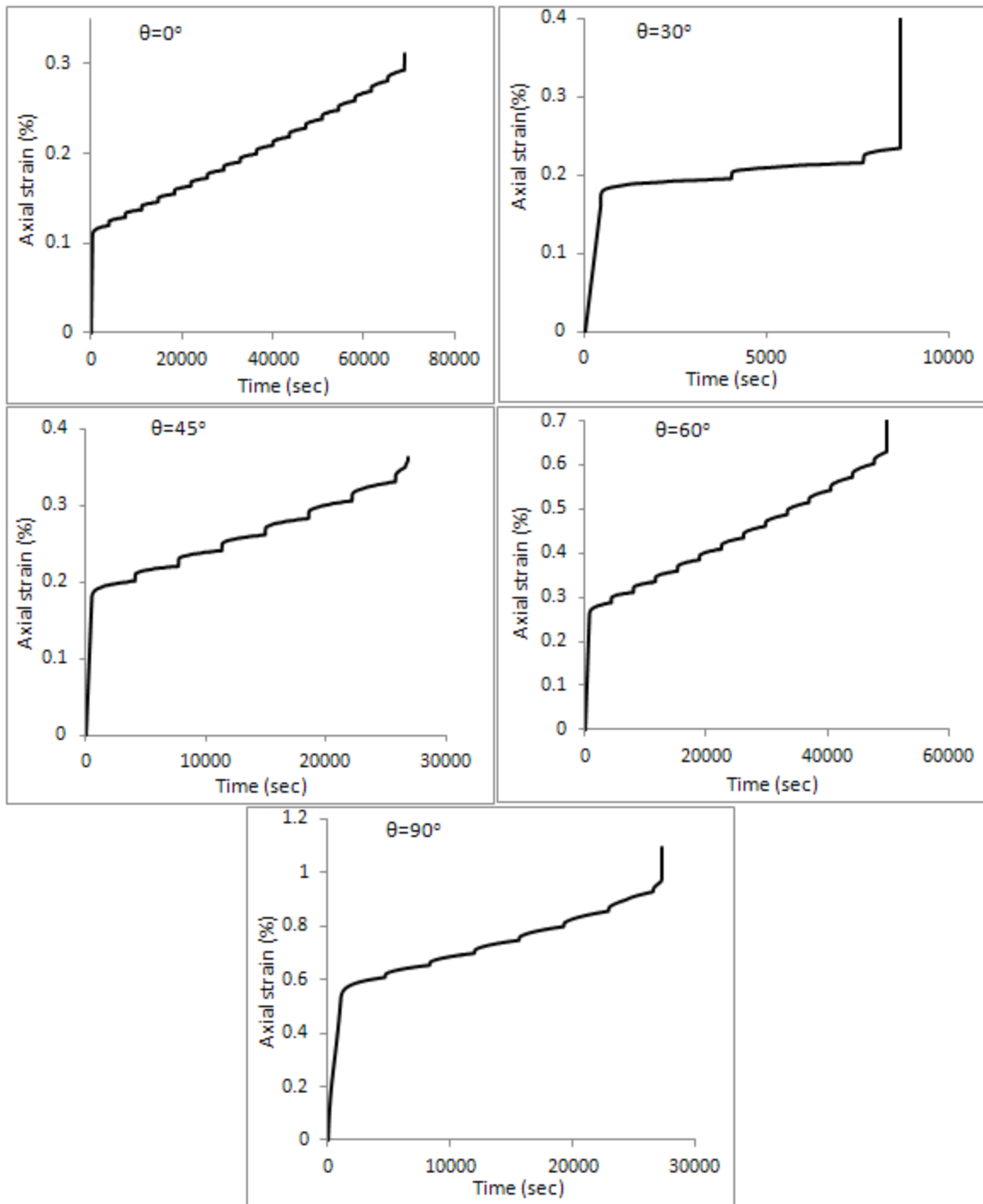Figure 2.15. Deviatoric stress-axial strain curves for different loading orientations.

Figure 2.16. Axial strain-time curves for different loading orientations.

2.7 Conclusions of Part 2

An experimental database of uniaxial compression tests, triaxial compression tests with confining pressures, confined and unconfined cyclic tests, and Brazilian tests on the Tournemire argillite has been generated. It was found that the Tournemire argillite is anisotropic in both strength and deformation behavior and it can be classified as a brittle material. The results can be used to establish and validate constitutive models for this anisotropic material.

Formation and propagation of microcracks within the material under stress depend on the mineralogical composition of the material. The Tournemire argillite has high clay content, 55%, which makes the argillite behaving less brittle than hard rocks. According to acoustic emission data, the new microcracks start to develop within the argillite at a stress level of about σ_{ci} =70% ~ 75% of the peak strength. The intensity of microcracking increases with the increase in stress level. In addition, the crack damage stress level is reached approximately at a stress level of σ_{cd} = 85% ~90% of the peak strength.

The mobilization of strength parameters during the experiments are as follows. Upon loading a specimen, the mobilized cohesion starts to increase very rapidly. The rate of increase in mobilized cohesion reduces when the stress level increases above approximately 70% of the peak strength. The mobilized cohesion reaches its maximum value at the peak strength and it reduces to a negligible value in the post-peak region. The value of the mobilized friction is very small at low stress levels, and it increases very rapidly when the stress level becomes more than the 70% of the peak strength. The mobilized friction angle reaches a maximum value at the peak strength. In the post-peak region of the experiment, the mobilized friction angle starts to decrease and eventually reaches a small value in uniaxial tests at large axial strains.

Axial and volumetric strains depend on θ and σ_c. Reducing the deviatoric stress in cyclic tests (unloading) provides the necessary data to calculate the elastic and plastic strains. Plastic strains were between two-thirds to one half of the total strain. The volumetric strain change is compressive up to the peak strength, after which dilation rapidly develops. The compressibility and shear behaviour of bedding planes play a significant role in the deformation of the argillite.

Time-dependent behaviour of the Tournemire argillite has been investigated. The creep tests showed that if the deviatoric stress is below the crack damage level, the creep of the rock is not significant. However, when the deviatoric stress exceeds the crack damage level the creep of the rock becomes more significant. This could be due to unstable crack growth under constant stress.

Part 3

Interpretation of the experimental results

3.1   Background

The main purpose of Part 3 is to interpret the experimental results described in Part 2. This includes the evaluation of the elastic and plastic response of the material, failure behavior of the material, establishing strength parameters, and comparing the results with previously published experimental data. Many parameters such as loading rate, sample size, moisture conditions, capabilities of the testing machine, testing protocols, etc, can affect the results of the tests. Therefore, comparison of the present experimental data with previous experimental data is not a straightforward process. However, we are expecting the same kind of trends in present test results.

3.2   Analysis of the Mechanical Behavior of Tournemire argillite

For the purpose of developing constitutive models for hard rocks, the experimentally obtained deviatoric stress-axial strain curves are divided into four zones: microcrack/bedding closure zone, elastic zone, elastoplastic zone with hardening, and a post-peak zone where the stress level sharply reduces towards the residual strength as shown in Fig. 3.1(a). Loading and unloading in the elastic zone would follow the same curve without producing any plastic strains. Somewhat similar deviatoric stress-axial strain curves were plotted for the Tournemire argillite. However, cyclic test results show that a purely elastic zone does not exists during monotonic loading in the case of Tournemire argillite, and the corresponding four zones are shown in Fig. 3.1(b). Plastic strains start to develop right from the beginning of the stress-strain curve. Therefore, the parameters of elastic stress-strain relation must be determined from the results of cyclic tests. A purely elastic behavior of the argillite exists only during the unloading-reloading cycles.
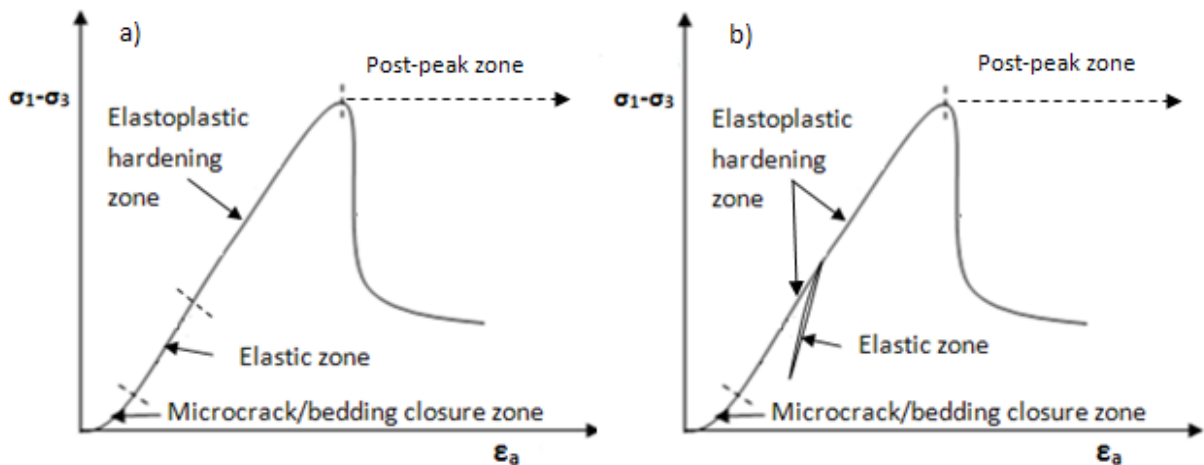

Figure 3.1: Schematic description of the stress-strain behavior: a) hard rock, and b) Tournemire argillite.

3.2.1 Microcrack/bedding closure zone

Sampling, transportation, and storage of the material may cause an increase in the size of the microcracks and opening of bedding planes. During uniaxial/triaxial testing, an increase in the stress level causes the closure of the existing microcracks and bedding planes. The closure of microcracks and the compression of the material between the bedding planes is more pronounced at $\theta=90^o$ than those in other loading orientations. However, such a "closure zone" in the stress-strain curves is less significant in the experiments with higher confining pressures as most initial microcracks and bedding planes are closed during the application of the hydrostatic pressure. The volume change in this zone is mainly compressive.

3.2.2 Elastic zone in cyclic tests

The elastic parameters of the Tournemire argillite were obtained from a straight line connecting the points representing the beginning of the unloading and reloading portions of the first cycle. Experimental data show that these parameters are strongly influenced by θ. The acoustic emission data seem to indicate that during unloading-reloading cycles in the elastic one, the stress-strain curve is free from any development of new microcracks. The Tournemire argillite can be classified as a transversely isotropic material (Niandou et al., 1997), and its elastic behavior can be described by the following relation:

$$
\begin{bmatrix} d\varepsilon_1 \\ d\varepsilon_2 \\ d\varepsilon_3 \\ d\gamma_{23} \\ d\gamma_{31} \\ d\gamma_{12} \end{bmatrix} = \begin{bmatrix} \frac{1}{E_1} & -\frac{v_{12}}{E_1} & -\frac{v_{12}}{E_1} & 0 & 0 & 0 \\ -\frac{v_{12}}{E_1} & \frac{1}{E_2} & -\frac{v_{23}}{E_2} & 0 & 0 & 0 \\ -\frac{v_{12}}{E_1} & -\frac{v_{23}}{E_2} & \frac{1}{E_2} & 0 & 0 & 0 \\ 0 & 0 & 0 & \frac{1}{G_{23}} & 0 & 0 \\ 0 & 0 & 0 & 0 & \frac{1}{G_{31}} & 0 \\ 0 & 0 & 0 & 0 & 0 & \frac{1}{G_{12}} \end{bmatrix} * \begin{bmatrix} d\sigma_1 \\ d\sigma_2 \\ d\sigma_3 \\ d\tau_{23} \\ d\tau_{31} \\ d\tau_{12} \end{bmatrix} \qquad (3.1)
$$

where the axis 1 is perpendicular to bedding planes, and axes 2 and 3 are parallel to bedding planes.

The above elastic compliance matrix depends on five independent parameters: E_1 and v_{12} that can be obtained from tests performed at $\theta=90^o$, E_2 and v_{23} that can be obtained from tests

performed at θ=0°, and the shear modulus G_{12} that can be obtained from a test performed at an angle 0°<θ<90° and using the following equation (Niandou et al., 1997):

$$G_{12} = \left(\frac{1}{E_i\, sin^2\theta\, cos^2\theta} - \frac{cos^2\theta}{E_2\, sin^2\theta} - \frac{sin^2\theta}{E_1\, cos^2\theta} + \frac{2\, v_{12}}{E_1}\right)^{-1} \qquad (3.2)$$

where E_i is the Young modulus which is determined from a test carried out in the θ orientation.

Elastic parameters

The unconfined cyclic tests are used to estimate the elastic parameters. In each test, the first unloading-reloading cycle is considered for estimating the parameters. From the cyclic test (θ=90°) on a rock specimen from borehole M9, the following two elastic parameters are obtained:

$$E_1 = 12.5\ GPa$$

$$v_{12} = 0.08$$

From the cyclic test (θ=0°) on a rock specimen from borehole M13, the following two elastic parameters are obtained:

$$E_2 = 21\ GPa$$

$$v_{23} = 0.16$$

In the framework of the theory of elasticity, the symmetry of the elastic matrix should be verified, e.g., $\frac{v_{12}}{E_1} = \frac{v_{21}}{E_2}$. This gives $v_{21} = 0.14$. Using the eq. 3.2 and the values of θ=45° and E_i = 12 GPa results in $G_{12} = 4.57\ GPa$.

The experimental data showed that the Young's modulus (E) varied with the stress level at which the unloading–reloading cycle was applied. Figure 3.2 shows the variation of E with the normalized deviatoric stress. In order to see the effect of loading orientation on E, the variation of E, estimated at 70% $\sigma_d/\sigma_{d\text{-peak}}$, with θ is shown in Fig. 3.3. Even though there is no big difference in the results of tests conducted at θ=30°, 45°, and 60°, the experimental data indicate that E is decreasing with the increase in θ.
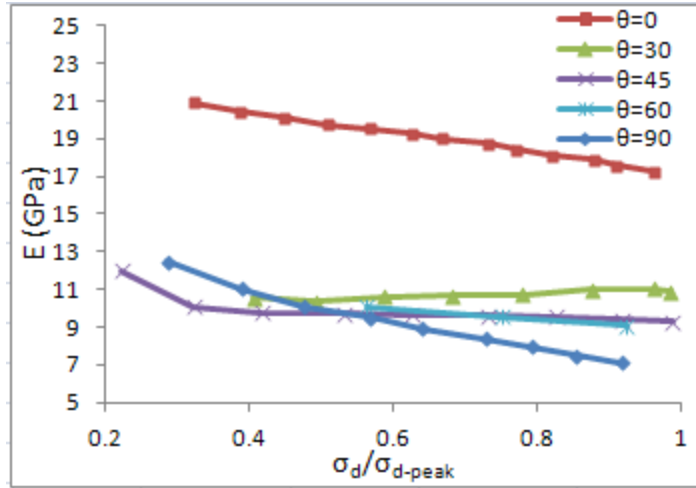
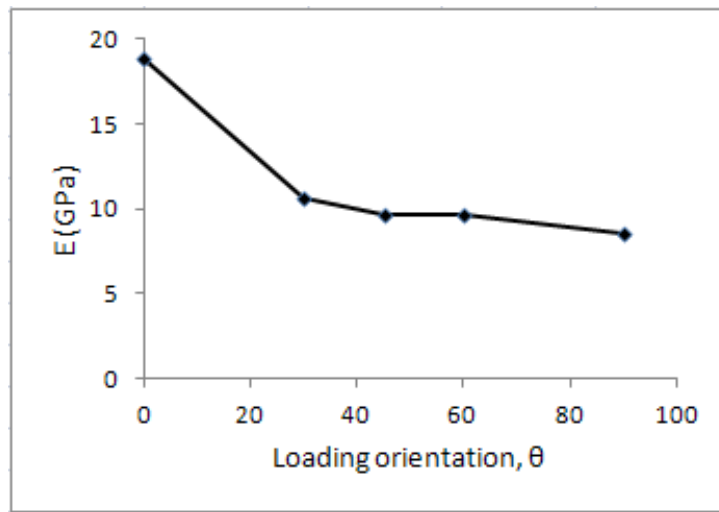Figure 3.2. Variation of E, estimated from unloading-reloading cycles, with $\sigma_d/\sigma_{d\text{-peak}}$.

Figure 3.3. Variation of E, estimated at 70% $\sigma_d/\sigma_{d\text{-peak}}$, with θ.

3.2.3   Elastoplastic hardening zone

For the Tournemire argillite, the elastoplastic hardening zone represents the nonlinear section of the stress-strain curve, from the end of the "microcrack/bedding closure zone" up to the peak strength. The amount of plastic strain that can develop in this zone depends on the stress level, θ and σ_c. The volumetric strain in this zone is mainly contraction. Acoustic emission data indicate that microcracks initiate in this section, at $\sigma_{ci} = 70\% \sim 75\%$ σ_{peak}. Above σ_{ci}, the formation and propagation of microcracks accelerate with the increase in stress level, and as

a result rapid degradation in the mechanical properties of the material is expected. Fracture/fractures start to develop within the specimen at the end of this zone and their number and orientation depend on θ. Also, the crack damage starts in this section at $\sigma_{cd} = 85\% \sim 90\%$ σ_{peak}.

Figure 3.4 shows the variation of the axial strain at peak strength with θ for different values of σ_c. The axial strain at peak strength increases with the increase in σ_c. At small values of θ ($<30^o$), there is no significant effect of θ on the values of the axial strain at peak strength. However, larger values of θ ($>30^o$) have a significant effect on the axial strain at peak strength. The axial strain at peak strength increases with the increase in θ.
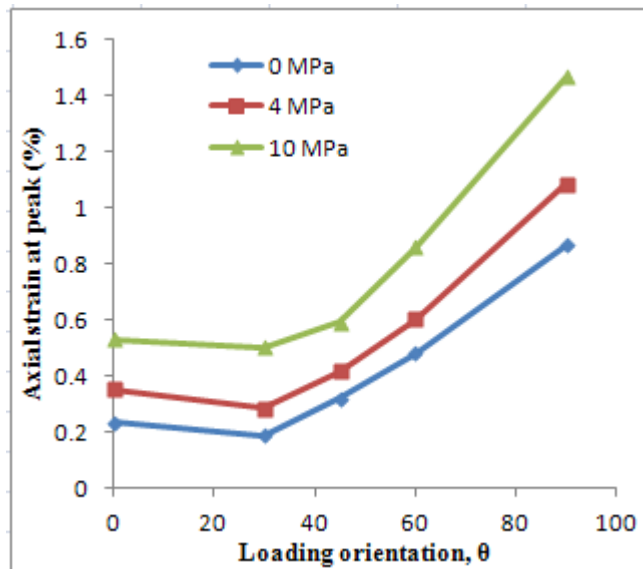
Figure 3.4: Variation of the axial strain at peak strength with θ for different values of σ_c.

Figure 3.5 shows the values of peak strength obtained in uniaxial and triaxial tests. This figure shows that the peak strength depends on θ and confining pressure, σ_c. For the range of σ_c considered, the maximum strength was obtained in tests performed at $\theta=0^o$. The strength obtained in tests performed at $\theta=90^o$ was smaller than the strength at $\theta=0^o$. The strength obtained in tests performed at a loading angle of $30^o \leq \theta \leq 60^o$ had the smallest values. This indicates that the compressive strength is highly sensitive to the load inclination and the shear strength characteristics of bedding planes.
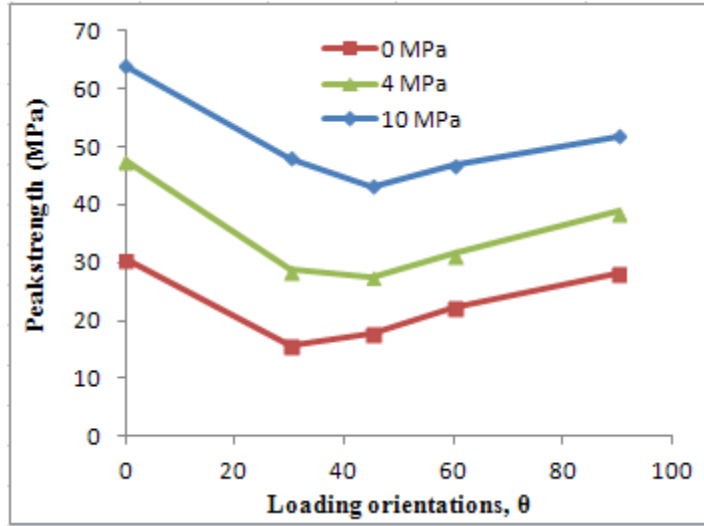
Figure 3.5: Variation of peak strength with θ for different values of σ_c.

3.2.4   Post-peak zone

The Tournemire argillite can be classified as a brittle material. A sudden collapse of the material, e.g. moving from peak strength towards a small value of strength measured in the post-peak region, is observed in uniaxial, triaxial, and cyclic tests. Figure 3.6 shows the smallest measured values of strength in the post-peak region obtained in uniaxial and triaxial tests, which depend on θ and σ_c. The highest value is measured in tests performed at θ=0°, whereas the lowest values are measured in tests performed at 30°≤θ≤60°.
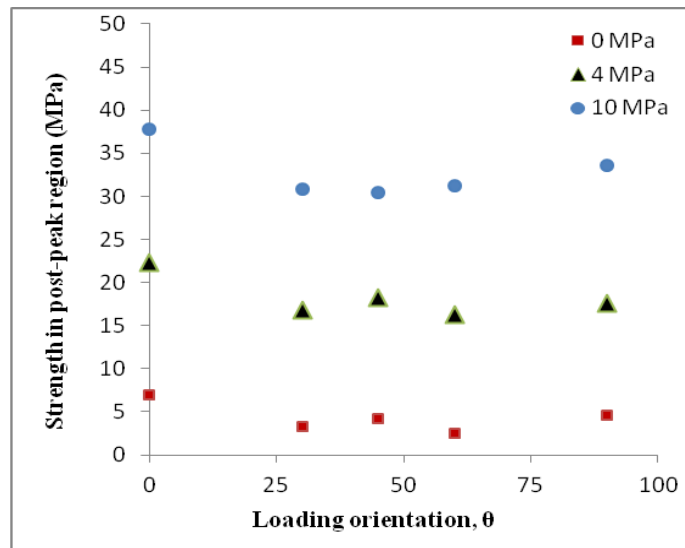
Figure 3.6: Variation of the strength in the post-peak region with θ for different values of σ_c.

3.3 Summary of observed behavior

Both the strength and stiffness of rock specimens reduce as microcracks develop. As shown in cyclic tests, an increase in stress level causes an increase in the amount of plastic strain. Figure 3.7 shows the variation of the Young's modulus with the number of cycles. Except for the loading orientation $\theta=30^{o}$, the degradation in Young's modulus is significant. Every additional loading-reloading cycle (at different stress levels) shows an extra degradation in the Young's modulus. Compared to uniaxial tests, it seems there is no significant effect of cycling on the strength and deformation properties of the material, and on the failure mode of the material.
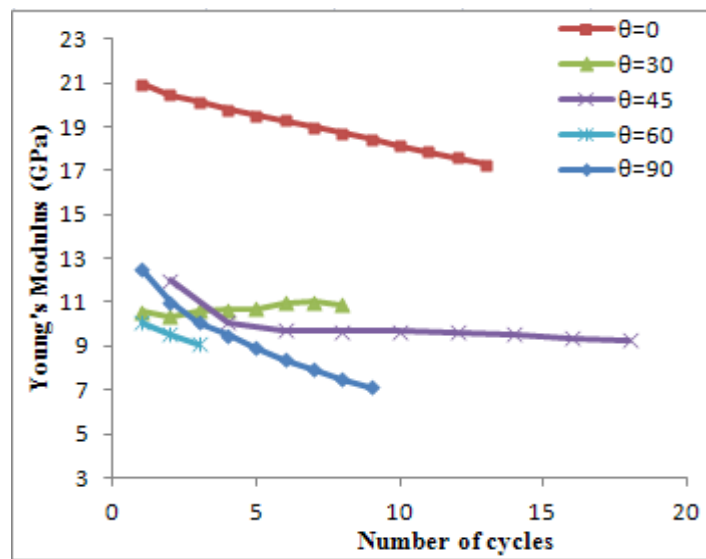

Figure 3.7: Variation of the Young's modulus with the number of cycles.

3.4 Parameters of peak strength and strength measured in post-peak region

The calculated values of both cohesion and friction angle at peak strength and minimum strength measured in post-peak region (SMIPPR) are listed in Table 3.1 for different loading orientations. The highest values of friction and cohesion are obtained in tests carried out at $\theta=0^{o}$. The data indicates that the strength parameters are sensitive to the inclination of bedding planes.

Table 3.1: Friction and cohesion at peak strength and at SMIPPR for different loading orientations, θ.

Loading orientation θ	Friction angle at peak strength φ (degrees)	Cohesion at peak strength c (MPa)	Friction angle at SMIPPR φ_{pp} (degrees)	Cohesion at SMIPPR c_{pp} (MPa)
0°	32.68	8.65	30.5	2.32
30°	31.26	4.4	27.7	1.01
45°	26.6	5.3	25.8	1.11
60°	27.2	6.43	26.1	1.15
90°	31.46	6.8	29	1.48

Note: Subscript "pp" means post-peak.

3.5 Strength anisotropy

The evolution of the degree of anisotropy is investigated by defining two parameters as follows:

$$k_1 = \frac{(\sigma_1 - \sigma_3)_{\theta=0}}{(\sigma_1 - \sigma_3)_{\theta=90}} \quad \text{and} \quad k_2 = \frac{(\sigma_1 - \sigma_3)_{max}}{(\sigma_1 - \sigma_3)_{min}}$$

In these equations, the parameter k_1 defines the ratio between the principal stress difference at the peak strength when θ=0° and the principal stress difference at the peak strength when θ=90°. The parameter k_1 must be determined from the tests conducted at the same confining pressures. The parameter k_2 defines the ratio between the maximum and minimum peak strengths for the same confining pressure. Figure 3.8 describes the experimental results obtained for both parameters. The parameter k_1 increases slightly with the increase in confining pressure, but its value is nearly equal to unity. This indicates that the strength anisotropy between the two principal axes, θ=0° and 90°, is small. The value of the parameter k_2 is nearly equal to two and it decreases with the increase in confining pressure. This indicates that the strength anisotropy becomes smaller for high confining pressures.
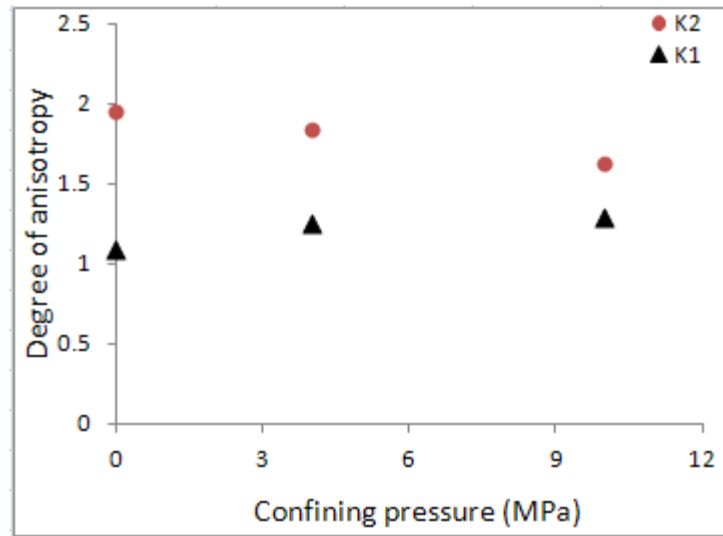
Figure 3.8: Variation of the degree of anisotropy with σ_c.

3.6   Main failure modes of the argillite

Fractures observed on failed samples indicate that the failure occurs in two principal modes: extension (splitting) and shearing. The mode of failure is a function of the loading orientation, θ, as shown in Fig. 3.9. The range of confining pressures considered in this investigation has little effect on the failure mode.

Testing at $\theta=0^o$

The failure mode is an extension type. In this particular test, two fractures (almost vertical) were developed and the sample was split into three blocks.

Testing at $\theta=30^o$, 45°, and 60°

The failure mode is shearing. It manifested itself by the opening and sliding of bedding planes. The orientation of the developed fracture is nearly equal to θ.

Testing at $\theta=90^o$

The failure mode is an extension type at the top of the rock specimen. The fracture cuts through the argillite sample perpendicular to the bedding planes. In the lower half of the specimen, the failure mode becomes shearing. The sample broke into three blocks. It is possible that the development of shear fractures is caused by the constraints imposed on the lower end of the specimen by the loading platen at the base.
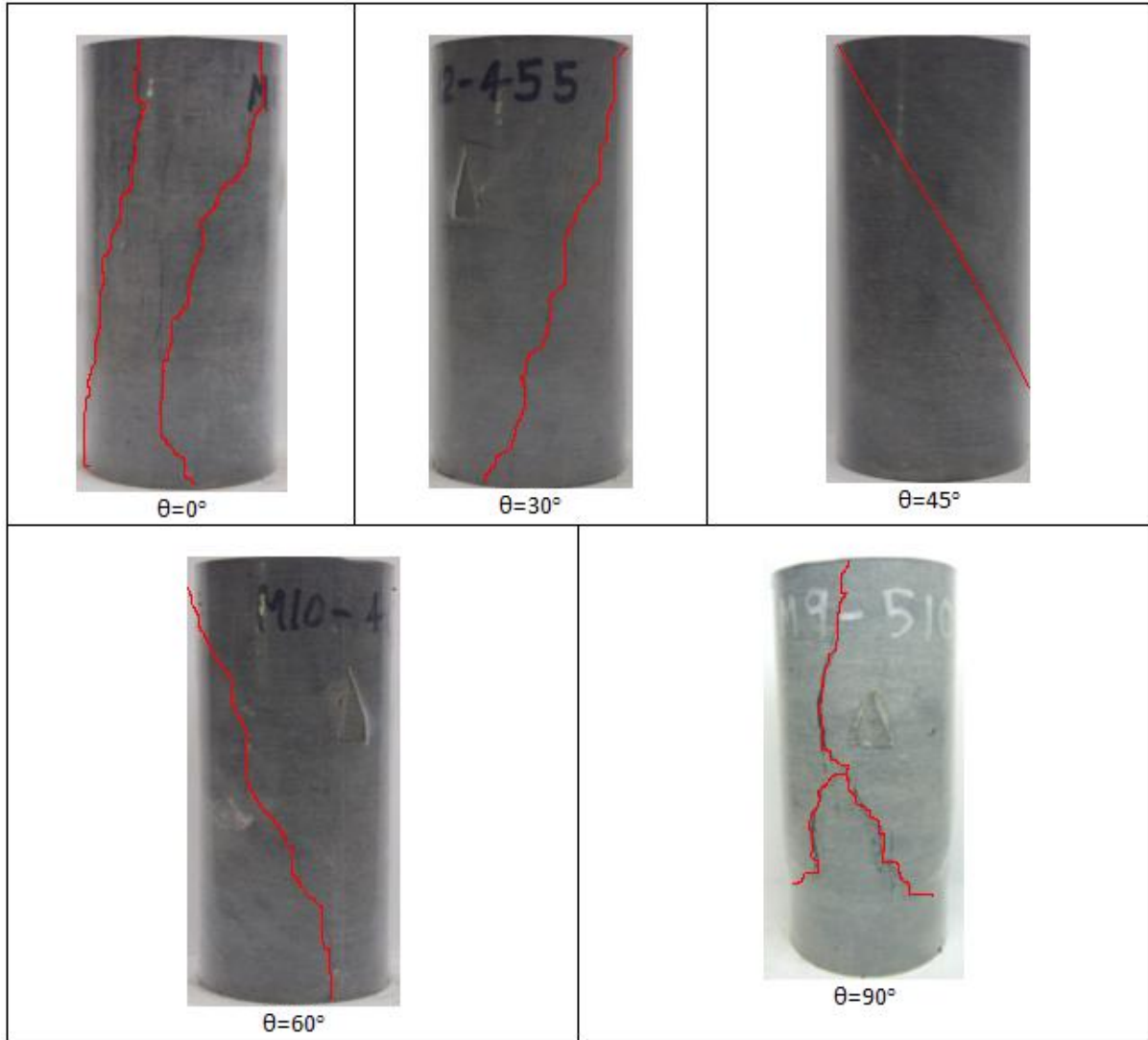
Figure 3.9: Failure modes for different values of θ.

3.7 Comparison with previous experimental data

Many parameters such as loading rate, sample size, capabilities of the testing machine, testing protocols, etc, can affect the results of the tests. Therefore, comparison of the present experimental data with previous experimental data is not a straightforward process. However, it is expected that similar trends to be observed in the present tests. The mechanical behavior of the Tournemire argillite was investigated by Niandou et al. (1997). The size of the specimen used by those authors was about 37 mm in diameter and 75 mm in height,

compared to, respectively, 61.3 mm and 133 mm, used in the present investigation. In the present study, all tests are displacement-controlled type except for the Brazilian tests. Here, comparisons of some key results are given.

The mechanical properties of the Tournemire argillite are anisotropic in both strength and deformation. The compressive strength, post-peak SMIPPR, axial strain, plastic strain, and volumetric strain are influenced by θ and σ_c. The elastic parameters are also influenced by θ. Similar observations were made by other authors.

In terms of the magnitude, the compressive strength values obtained in this research are around two-thirds of the compressive strength values reported by other authors. On the other hand, the axial and volumetric strains measured in the present investigation are higher than those by Niandou et al. (1997). In the cyclic tests of the present study, after the removal of the deviatoric stress the plastic strain represents between two-thirds to one half of the total strain and the other authors reported a value of one half. However, the values of the elastic modulus in the two main directions and shear modulus are very close to the corresponding values reported by other authors. With respect to Poisson's ratio, the results of the present study are slightly less than those reported by Niandou et al. (1997).

3.8   Conclusions of Part 3

The mechanical behavior of the Tournemire argillite can be divided into four zones: microcrack/bedding closure zone, elastoplastic hardening zone, an elastic zone which exists only during unloading-reloading cycles, and post-peak zone. Elastic parameters are estimated from the material behavior during the unloading-reloading cycles of the experiments, and they are influenced by θ and the number of cycles. The strength parameters of the material are also influenced by θ.

The peak strength and SMIPPR of the material depend on the loading angle, θ and the confining pressure, σ_c. For the range of σ_c considered the maximum strength is measured in tests performed at $\theta=0^o$. The peak strength obtained in tests performed at $\theta=90^o$ is slightly less than the strength in tests with $\theta=0^o$. The minimum strength is obtained in tests performed at $30^o \leq \theta \leq 45^o$. The tensile strength does not show much dependence on θ. When considering only the two principal axes ($\theta=0^o$ and $\theta=90^o$), the strength anisotropy parameter k_1 is small and close to unity. When considering all the orientations, the strength anisotropy parameter k_2 is close to two and it becomes smaller for high values of σ_c.

Cyclic behavior of the Tournemire argillite depends on whether cycling is performed before or after the peak strength. Load cycling (at different stress levels) before the peak strength causes additional plastic strains to develop. In addition, the Young's modulus degrades and sample contraction increase with additional load cycles. The cyclic behavior of the material after the peak is controlled by the fracture/fractures. Compared to uniaxial tests, cyclic loading had no significant effect on the strength and deformation properties of the material, and on the failure mode of the material. However, this conclusion cannot be generalized, because of the limited number of cycles used in the present investigation.

The development of constitutive relationships for the Tournemire argillite could be based on the classical framework of strain hardening/softening plasticity. To take into account the inherent anisotropy of the argillite, one can adopt transversely isotropic elasticity in the elastic domain, and the microstructure tensor approach in the plastic domain (Pietruszczak and Mroz, 2001). Damage effect on elastic parameters due to microcracking could be included into the formulation using, e.g., Kachanov model.

For the Tournemire argillite, the failure occurs in two principal modes: extension (splitting) and shearing. The mode of failure is a function of the loading orientation, θ. The range of confining pressures considered in this investigation has little effect on the failure mode.

Part 4

An elastoplastic model for simulating the mechanical behavior of the Tournemire argillite

4.1   Background

This Part 4 describes an elastoplastic model for simulating the mechanical behavior of the Tournemire argillite. The model is formulated based on the classical theory of plasticity and continuum damage mechanics concepts. The model requires the definition of a yield surface, flow rule, hardening law, a failure criterion, and a representation of damage caused by the initiation and propagation of the microcracks under stress. The effects of inherent anisotropy on the deformation and strength properties are incorporated in the model. All model parameters are estimated from the experimental data.

The capabilities of the model are evaluated by simulating uniaxial compression tests, triaxial compression tests with confining pressures, and unconfined and confined cyclic tests. Five different loading orientations are considered in the analysis ($\theta=0^o$, 30°, 45°, 60°, and 90°). The development of microcracks is assumed to be uniform throughout the material. The Tournemire argillite and the loading orientation angle are described in Part 2. A typical stress-strain curve for the Tournemire argillite is sketched in Part 3.

4.2   Formulation of the elastoplastic model

The classical theory of plasticity is used in conjunction with continuum damage mechanics concepts to formulate the model. The yield surface is expressed as a function of mobilized strength parameters under stress. Kachanov equation is used to represent the damage caused by the initiation and propagation of the microcracks on the elastic properties of the material.

4.2.1 Strength parameters and yield criterion

As mentioned in Part 2, for the Tournemire argillite the plastic strain starts to develop at the beginning of the stress-strain relationship. In order to calculate the plastic strain, the values of the mobilized strength parameters along the stress-strain curve should be known. Figures 4.1 and 4.2 describe such values that are obtained with the modeling at different stress levels as a function of loading orientation angle and confining pressure. These results were obtained by using the test data and the numerical simulations. In general, upon loading the specimen, the mobilized cohesion starts to increase very rapidly with the increase in axial strain and its rate of increase reduces when the stress level becomes more than σ_{ci}. The mobilized cohesion reaches a maximum value at the peak strength, and it reduces rapidly to a small value after the peak which depends on the confining pressure. On the other hand, the mobilized friction angle is small at very low stress levels. When the stress level is above σ_{ci}, the increase in the

mobilized friction angle becomes large and its value reaches a maximum value at the peak
strength. In the post peak region, the mobilized friction angle starts to decrease.
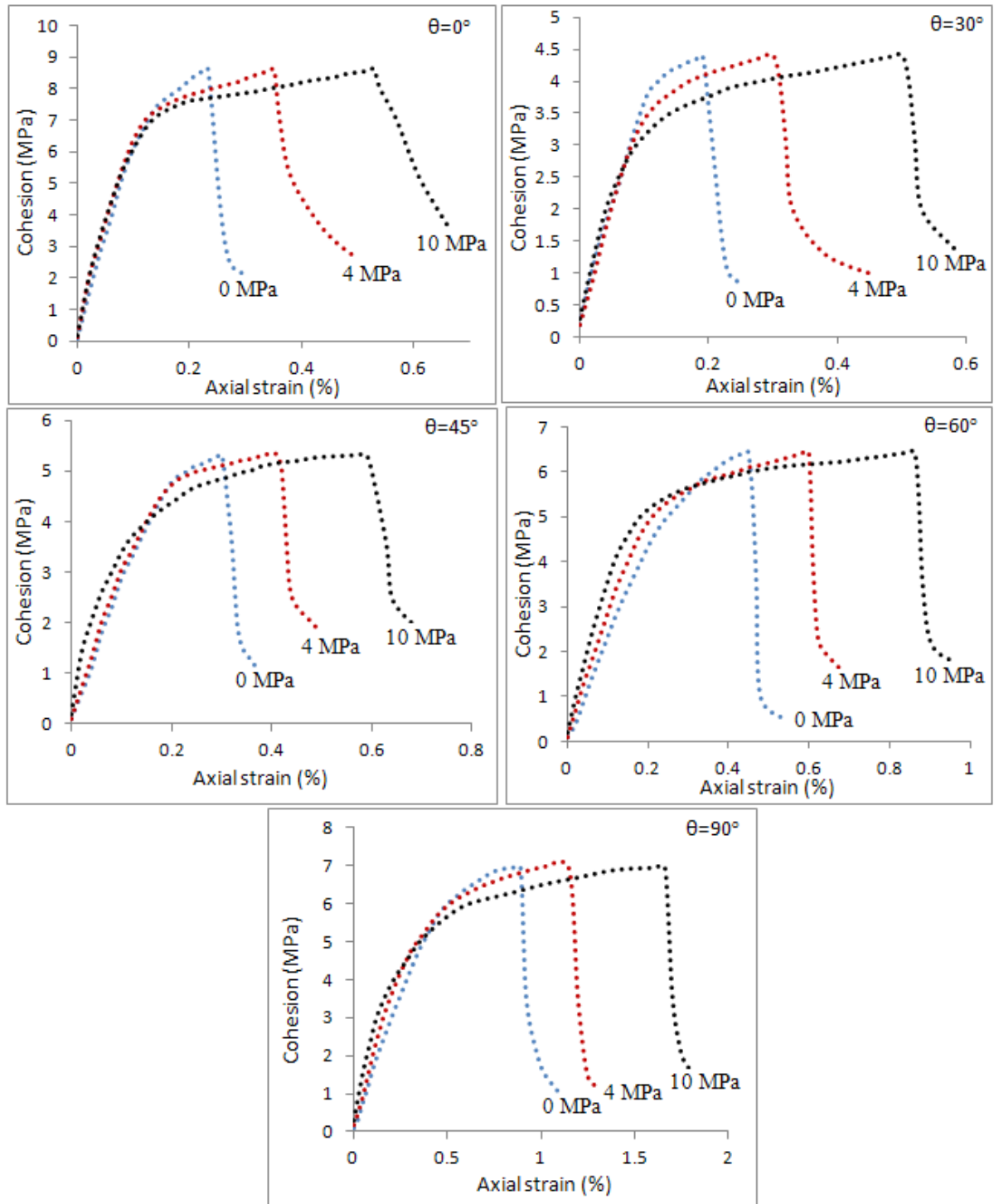
Figure 4.1. Mobilized cohesion versus axial strain curves for different loading orientations (θ) and confining pressures σ_c= 0 MPa, 4 MPa, and 10 MPa.
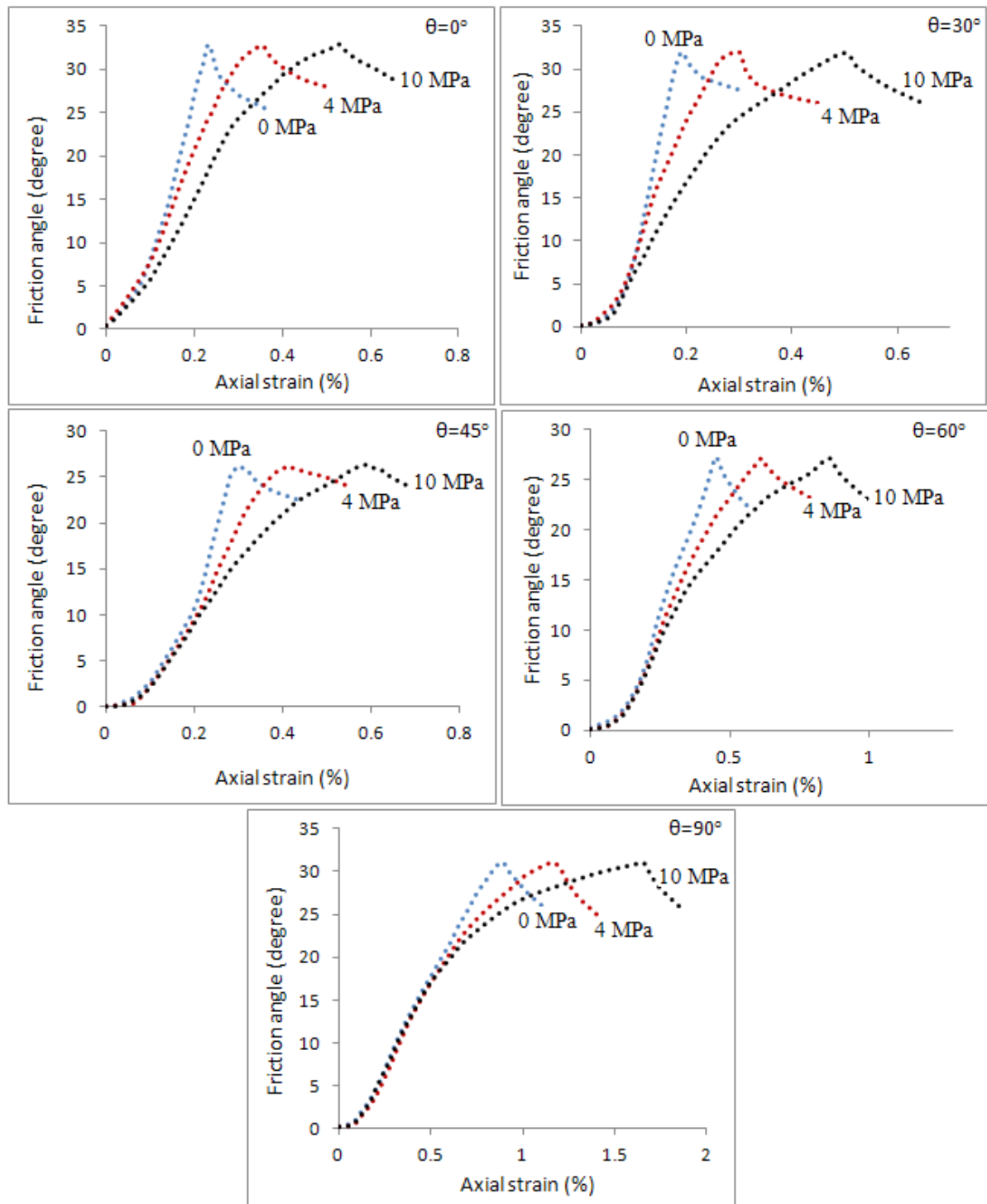

Figure 4.2. Mobilized friction angle versus axial strain curves for different loading orientations (θ) and confining pressures σ_c= 0 MPa, 4 MPa, and 10 MPa.

Different forms of yield criteria have been reported in the literature. In most cases, however, a yield criterion is expressed as a function of stress invariants and mobilized strength/material parameters. In the present analysis, the yield criterion has the following form:

$$F = J_2^{1/2} * \left(\cos\beta - \sin\beta * \frac{\sin\varphi_m}{\sqrt{3}}\right) - (I_1/3) * \sin\varphi_m - C_m * \cos\varphi_m = 0 \qquad (4.1)$$

where I_1 is the first invariant of the stress tensor and J_2 is the second invariant of the deviatoric stress tensor. In this equation, β is the Lode angle; c_m is the mobilized cohesion and φ_m is the mobilized friction angle of the material. At the time of failure, C_m becomes equal to C_{peak} and φ_m becomes equal to φ_{peak}.

Figure 4.3 describes the translation of the yield envelope as a function of the mobilized strength parameters for a uniaxial test ($\theta=45°$). The cohesion of the material controls the translation process at low stress levels. At high stress levels the friction has more effect.
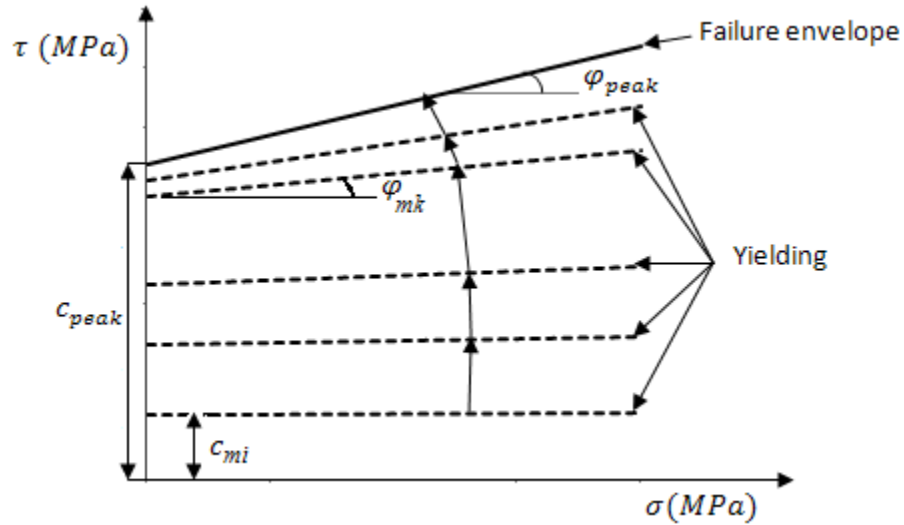

Figure 4.3. Illustration of the translation of the yield surface as a function of the mobilized strength parameters for a uniaxial test ($\theta=45°$). Note: c_{mi} indicates the mobilized cohesion at stress level i. Similarly, φ_{mk} indicates the mobilized friction angle at stress level k.

4.2.2 Characterization of damage

The mechanical and hydraulic properties of a rock mass can be affected by the process of microcracking; see for example Rutqvist et al. (2009) and Martin (1993). Different approaches have been developed to measure the damage or to formulate continuum damage mechanics constitutive equations. For isotropic damage, the equal distribution of microcracks in all directions is assumed. In this case, Kachanov (1958) defined a damage parameter D as shown in Fig. 4.4. This figure considers the effect of damage on the elastic modulus of the material. The damage parameter can be treated as a scalar quantity and completely characterizes the three-dimensional damage state. In his one dimensional model, Kachanov stated that the stress-strain relationship can be expressed as follows.

$$\varepsilon = \frac{\sigma}{E\,(1-D)} \tag{4.2}$$

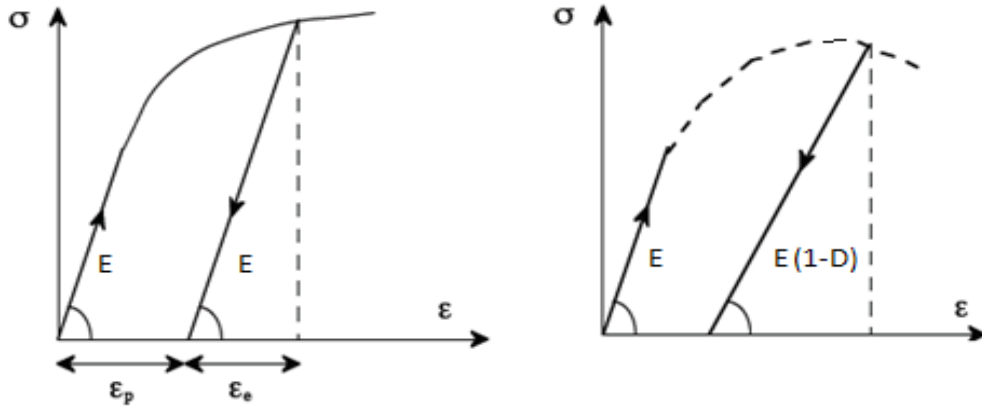The damage parameter D can be expressed in terms of stress or strain.

Figure 4.4. Stiffness degradation (D is the scalar damage variable).

In general, the damage induced in most geomaterials is anisotropic due to preferred orientation of microcracks. In the present analysis, it is assumed that the formation of microcracks to be uniform which means the effect of damage on Poisson's ratio is negligible. However, for each loading orientation, the effect of damage due to microcracking on the stiffness of the material is assumed to be a function of the effective plastic strain (Martin, 1993; Nguyen, 2007). The following expression is used to express the relationship between damage and plastic strain:

$$E = E_0(1 - d\,\varepsilon_p) \tag{4.3}$$

where E_0 is the initial elastic modulus (obtained from the first cycle in an orientation-dependent cyclic test), d is a material constant which is determined to be 30 for the

Tournemire argillite according to the calibration procedure discussed in the next section, and ε_p is the effective plastic strain. For each axis direction (x, y, or z), the corresponding Young's modulus is defined according to the Eq. 4.3.

Thus, the effect of damage is considered in all four zones of the stress-strain relationship from the beginning of loading to the failure of the specimen, including unloading-reloading cycles.

4.2.3 Stress-strain relationship

The strain increments are divided into elastic and plastic parts.

$$d\varepsilon = d\varepsilon_e + d\varepsilon_p \tag{4.4}$$

The plastic strain increment is given by:

$$d\varepsilon_p = \lambda \frac{\partial F}{\partial \sigma} \tag{4.5}$$

where the scalar, λ, represents a proportionality coefficient that can change with loading.

The incremental stress-strain relationship can be expressed as follows:

$$d\sigma = D_{ep} d\varepsilon \tag{4.6}$$

where D_{ep} is the elastoplastic constitutive matrix, $d\sigma$ and $d\varepsilon$ are the increments of the stress and strain, respectively, written in vector form.

The expression of D_{ep} is:

$$D_{ep} = D_e - \frac{D_e \frac{\partial F}{\partial \sigma}\left(\frac{\partial F}{\partial \sigma}\right)^T D_e}{A + \left(\frac{\partial F}{\partial \sigma}\right)^T D_e \frac{\partial F}{\partial \sigma}} \tag{4.7}$$

The elastic matrix is defined as:

$$D_e = \begin{bmatrix} \dfrac{1}{E_x} & \dfrac{-v_{yx}}{E_y} & \dfrac{-v_{zx}}{E_z} & & & \\ \dfrac{-v_{xy}}{E_x} & \dfrac{1}{E_y} & \dfrac{-v_{zy}}{E_z} & & 0 & \\ \dfrac{-v_{xz}}{E_x} & \dfrac{-v_{yz}}{E_y} & \dfrac{1}{E_z} & & & \\ & & & \dfrac{1}{2G_{yz}} & 0 & 0 \\ & 0 & & 0 & \dfrac{1}{2G_{zx}} & 0 \\ & & & 0 & 0 & \dfrac{1}{2G_{xy}} \end{bmatrix} \tag{4.8}$$

The parameter A is defined as follows:

$$A = -\frac{\partial F}{\partial h}(\sigma)^T \frac{\partial F}{\partial \sigma} \tag{4.9}$$

where h is the hardening parameter.

4.3   Numerical simulations of experimental data

Numerical simulations were carried out using the Mohr-Coulomb failure criterion. The Mohr-Coulomb criterion used in these simulations has not been extended to take into account the inherent anisotropy of the argillite.   Rather, different values of the Mohr-Coulomb parameters are input for different load orientations in order to determine the best-fit values of those parameters. A   possible generalization of the Mohr-Coulomb criterion that considers inherent anisotropy will be discussed in the next section. Numerical results are compared with experimental data obtained from uniaxial tests, triaxial tests with confining pressures, and unconfined and confined cyclic tests on the Tournemire argillite. Five different loading orientations and three different confining pressures are considered.

4.3.1   Numerical simulations of uniaxial and triaxial compression tests

Five uniaxial tests and ten triaxial tests are numerically simulated. Five different loading orientations ($\theta=0^o$, 30°, 45°, 60°, and 90°) and three different confining pressures (0 MPa, 4 MPa, and 10 MPa) are considered. For the purpose of comparison, the deviatoric stress-axial strain curves obtained from the numerical simulations for different loading orientations are shown together with the corresponding curves obtained from the experiments (Fig. 4.5).

Deviatoric stress-volumetric strain curves are shown in Fig. 4.6. In the experiments, the reversal from contraction to dilation occurs at a stress level σ_r equal to the peak strength. In

the numerical simulations, the reversal from contraction to dilation occurs at σ_r which is less than the peak strength. The level of this stress depends on both confining pressure and loading orientation angle. In general, compared to the results of the experiments, smaller volumetric strain in the contraction side and larger volumetric strain in the extension side are predicted. This small difference in the results could be due to the following:

- Continuum-based numerical models cannot predict the closure, formation, and propagation of microcracks and fractures.
- In the experiments, a chain extensometer is used to measure the circumferential displacements at the center of the test specimen. However, it is observed that the deformed shape of the specimen at failure is not uniform. This indicates that the measured values of the volumetric strain after the peak strength could be less than the actual values.
- In the numerical simulations, it is assumed that the material is homogeneous. However, the specimen used in the experiments may contain pre-existing microcracks and small fractures. Their mechanical properties may not be homogeneous.
- Applying associated flow rule in plasticity over-predicts the volumetric strain.

But, in general, a good agreement is obtained between numerical and experimental results.
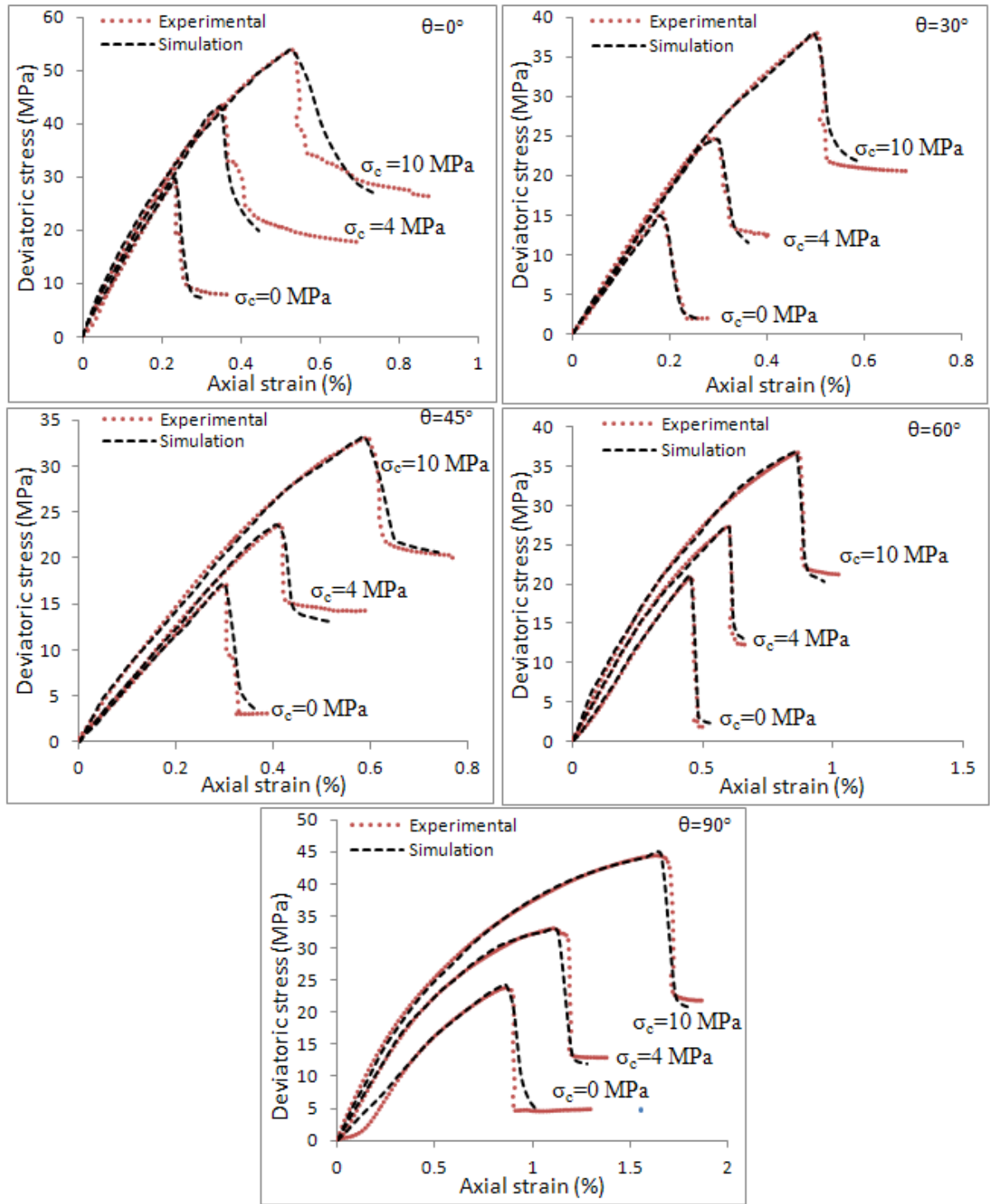
Figure 4.5. Deviatoric stress versus axial strain curves for uniaxial and triaxial tests, obtained from experiments and numerical simulations.
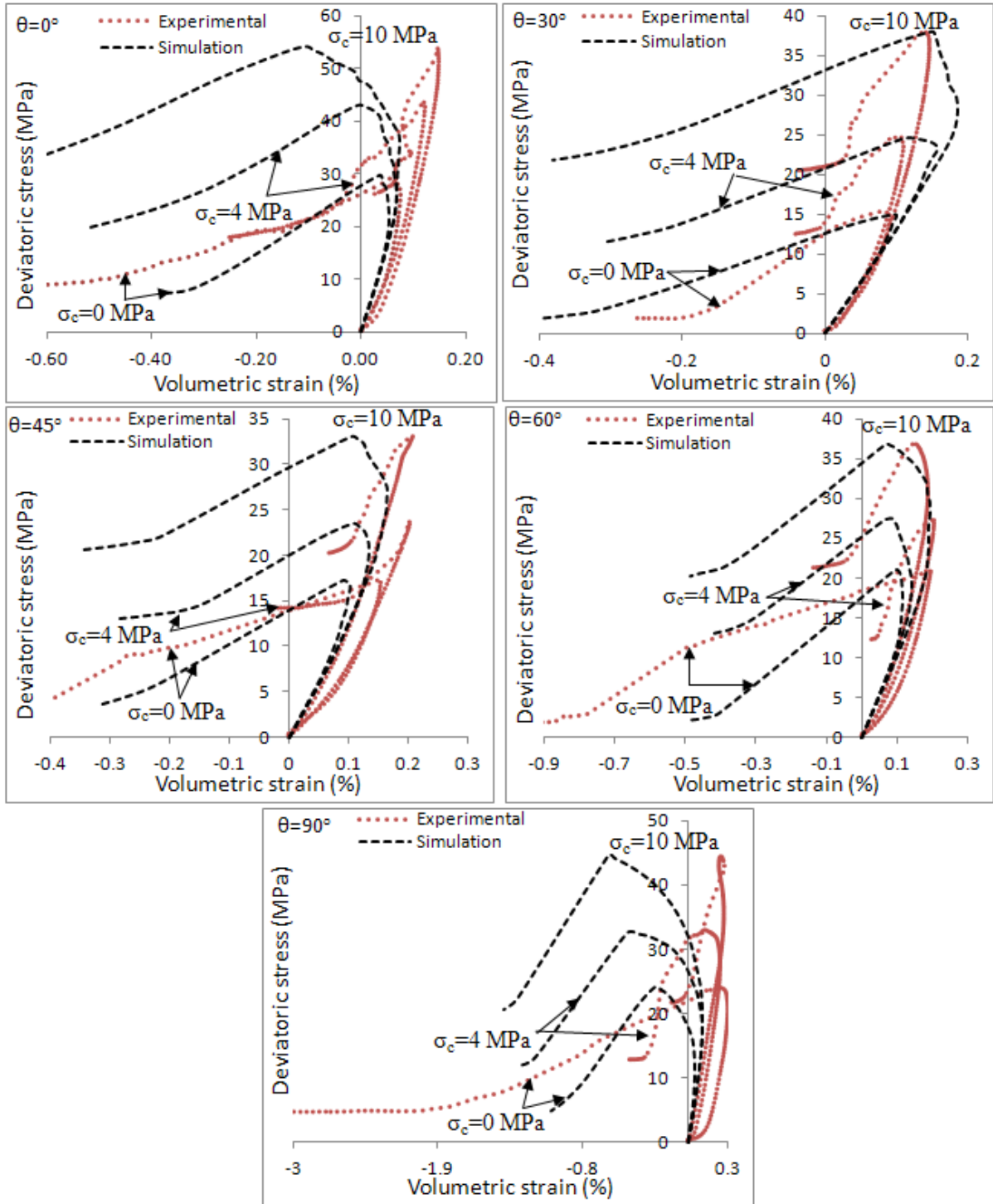
Figure 4.6. Deviatoric stress versus volumetric strain curves for uniaxial and triaxial tests, obtained from experiments and numerical simulations.

Figure 4.7 describes the results of the numerical simulation of the variation of the effective plastic strain versus deviatoric stress for different loading orientations. The effective plastic strain starts to develop at the beginning of the stress-strain curve and it is very sensitive to the inclination of bedding planes. The larger values of the effective plastic strain are calculated for the case where the loading is perpendicular to bedding planes.
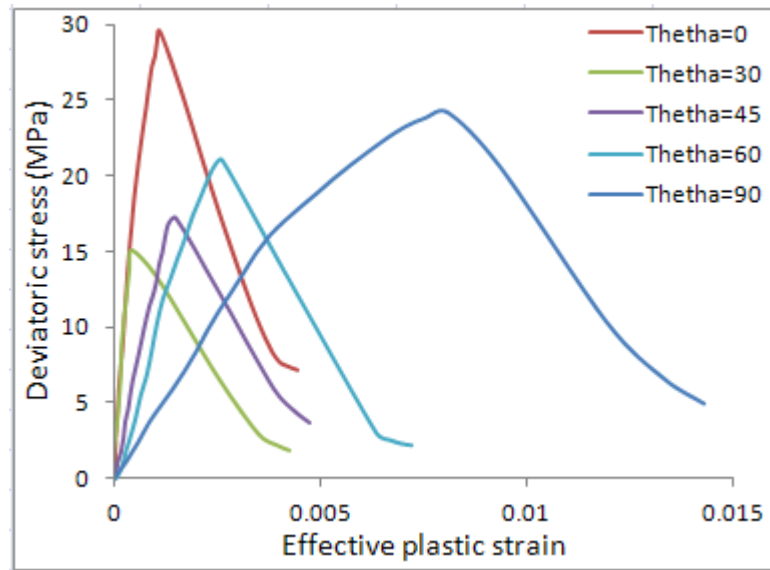
Figure 4.7. Deviatoric stress-effective plastic strain curves for different loading orientations.

4.3.2   Numerical simulations of unconfined cyclic tests

Five uniaxial cyclic tests are numerically simulated. Five different loading orientation angles are considered: $\theta=0^{\circ}$, 30°, 45°, 60°, and 90°. In each cyclic test, only a couple of cycles are numerically simulated. The deviatoric stress-axial strain curves obtained from numerical simulations are shown together with the corresponding curves obtained from the experiments (Fig. 4.8). Deviatoric stress versus volumetric strain curves are shown in Fig. 4.9. As mentioned above, in the experiments, the reversal from contraction to extension occurs at σ_r = peak stress. In the numerical simulations, the reversal from contraction to extension occurs at a stress level σ_r smaller than peak strength. In both experiments and numerical simulations, if cycling is below σ_r the specimen experiences only a small change in volumetric strain with each additional cycle (contraction). If cycling is above σ_r, the specimen experiences a significant change in volumetric strain (extension) with each additional cycle.
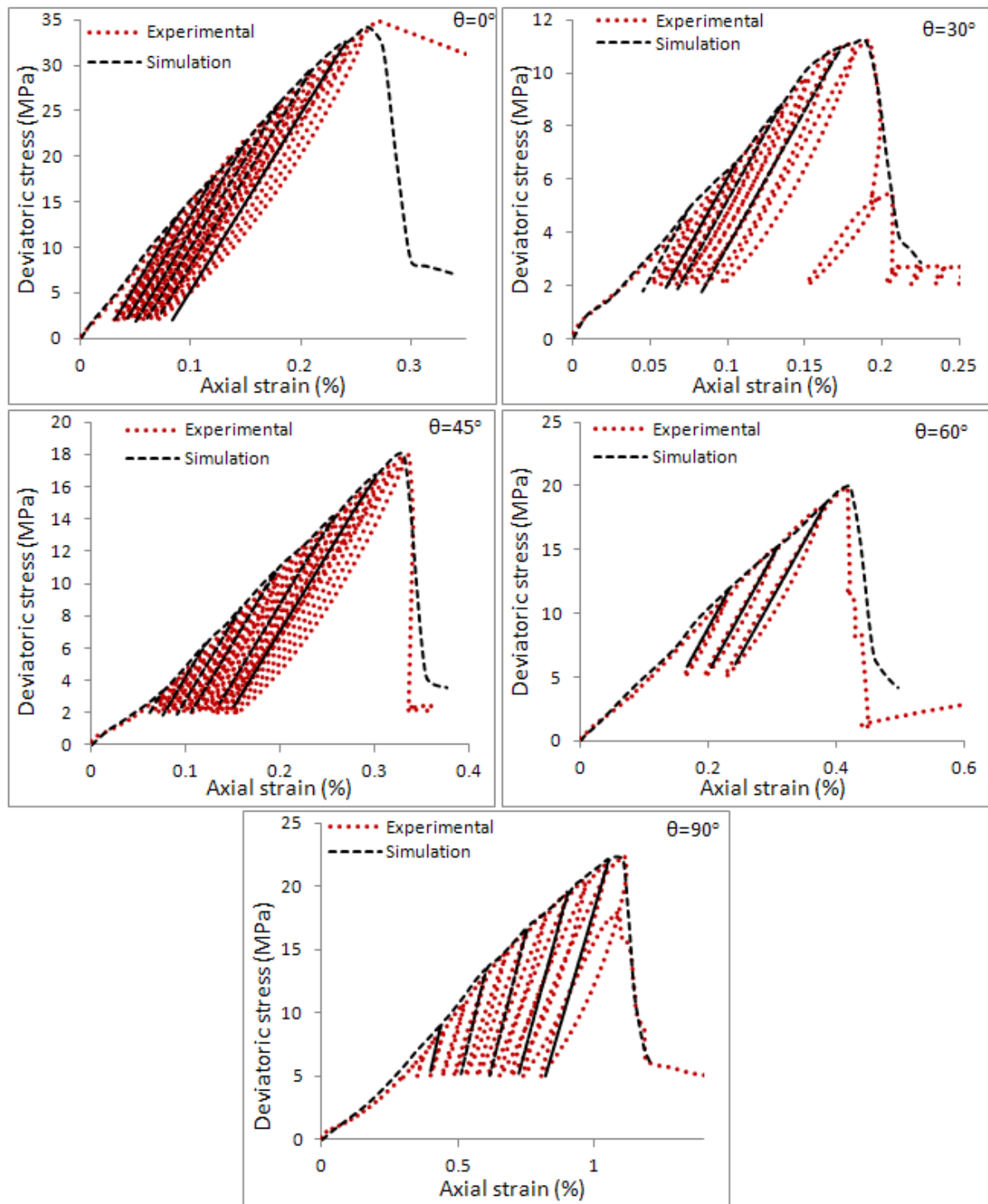
Figure 4.8. Deviatoric stress versus axial strain curves for unconfined cyclic tests, obtained from experiments and numerical simulations.
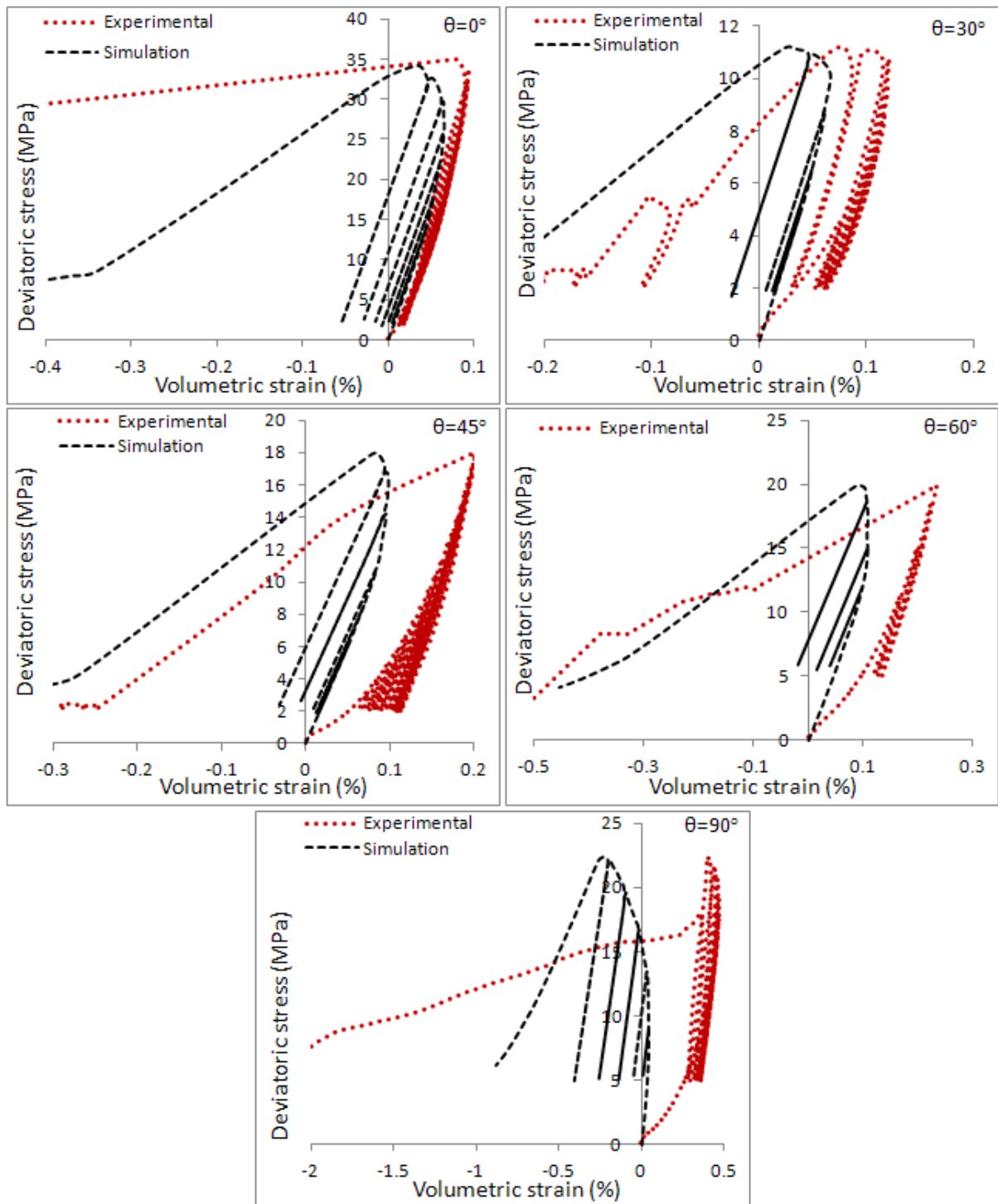
Figure 4.9. Deviatoric stress versus volumetric strain curves for unconfined cyclic tests, obtained from experiments and numerical simulations.

4.3.4   Numerical simulations of confined cyclic tests

To further explore the capabilities of the model, two more confined cyclic tests are simulated. Two loading orientations, $\theta=0^o$ and 45°, and a confining pressure of $\sigma_c=10$ MPa are considered. Stress-strain curves obtained from numerical simulations and experimental results for both loading orientations are shown together in Fig. 4.10. Measured and calculated results are comparable. Smaller volumetric strain is predicted in the contraction side and this could be due to similar reasons as explained before. In the extension side, larger volumetric strain is predicted and the reversal from contraction to extension occurred at a stress level less than the peak strength. The results of these tests clearly indicate that the model can predict the mechanical behaviour of the Tournemire argillite under any triaxial loading condition.
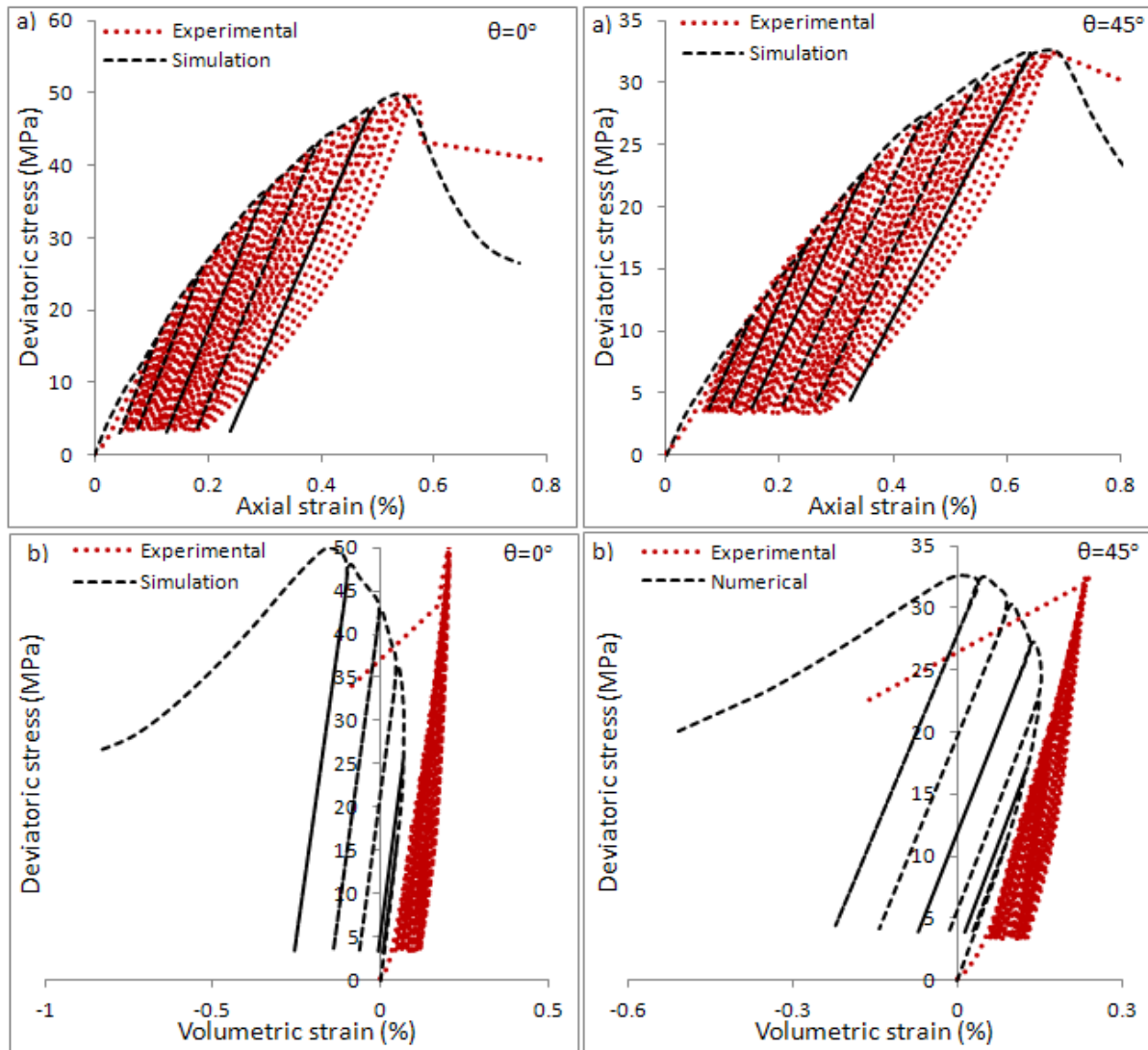
Figure 4.10. Stress-strain curves for confined cyclic tests; a) Deviatoric stress-axial strain curves, b) Deviatoric stress versus volumetric strain curves.

4.4 Anisotropic yield criterion and derivation of strength descriptors for the Tournemire argillite

Based on the microstructure approach, Pietruszczak and Mroz (2001) extended the Mohr-Coulomb yield criterion and a flow rule to the case of inherent anisotropy. Here, the formulation is summarized and the relevant orientation-dependent strength descriptors for the Tournemire argillite are derived.

4.4.1 Microstructure approach

The microstructure approach requires the introduction of only one anisotropic scalar parameter, η. This parameter represents the projection of the second-order microstructure tensor a_{ij}, which describes the spatial distribution of the microstructure of the material, on a well defined loading direction (l). It is defined as the ratio of joint invariants of stress and microstructure tensor $a_{ij} \sigma_{ik} \sigma_{jk}$ to the stress invariant $\sigma_{ij} \sigma_{ij}$.

$$\eta = a_{ij} l_i l_j = \frac{tr(a_{ik} \sigma_{ij} \sigma_{kj})}{tr(\sigma_{pq} \sigma_{pq})} \tag{4.10}$$

The vector l is defined as follows:

$$l_i = \frac{L_i}{\sqrt{L_k L_k}} = L_1 e_i^{(1)} + L_2 e_i^{(2)} + L_3 e_i^{(3)} \tag{4.11}$$

where $L_1 = \sqrt{\sigma_{11}^2 + \sigma_{12}^2 + \sigma_{13}^2}$, $L_2 = \sqrt{\sigma_{21}^2 + \sigma_{22}^2 + \sigma_{23}^2}$, $L_3 = \sqrt{\sigma_{31}^2 + \sigma_{32}^2 + \sigma_{33}^2}$

and, e_i^γ, γ=1,2,3, define the preferred material axes.

The parameter η can also be expressed in a general from:

$$\eta = \eta_0 (1 + A_{ij} l_i l_j) \tag{4.12}$$

where:

$A_{ij} = \frac{1}{\eta_0} a_{ij} - \delta_{ij}$ and $\eta_0 = \frac{1}{3} a_{kk}$

The Eq. 4.12 can be generalized by considering higher order tensors:

$$\eta = \eta_0 \left(1 + A_{ij}l_il_j + A_{ijkl}l_il_jl_kl_l + A_{ijklmn}l_il_jl_kl_ll_ml_n + \dots\right)$$ (4.13)

For simplicity reasons, the higher order tensors are defined as follows.

$$A_{ijkl} = b_1 A_{ij}A_{kl}, A_{ijklmn} = b_2 A_{ij}A_{kl}A_{mn}, \dots$$

Therefore, η can be defined in the following general form.

$$\eta = \eta_0 \left(1 + A_{ij}l_il_j + b_1(A_{ij}l_il_j)^2 + b_2(A_{ij}l_il_j)^3 + b_3(A_{ij}l_il_j)^4\right)$$ (4.14)

where "b"s are constants.

4.4.2 Incorporating η into Mohr-Coulomb failure criterion and a flow rule

The anisotropic parameter, η, can be incorporated into plasticity formulations. The yielding function can be expressed in the general form as follows.

$$f = f\left(\sigma_{ij}, a_{ij}, \varepsilon_{ij}^p\right) = f(I_1, I_2, I_3, \eta, h) = 0$$ (4.15)

where I_1, I_2, and I_3 are the first, second, and third invariants of the stress tensor, h is the hardening parameter. The parameter η is typically identified with a relevant strength descriptor, whose value is then assumed to depend on the orientation of the bedding planes relative to loading orientation.

The Mohr-Coulomb failure criterion is expressed in the functional form as follows.

$$F = \sqrt{3}\bar{\sigma} - \eta \, g(\beta)(\sigma_m + C) = 0$$ (4.16)

where

$$g(\beta) = \frac{3 - \sin\phi}{2\sqrt{3}\cos\beta - 2\sin\beta\sin\phi}; \eta = \frac{6\sin\phi}{3 - \sin\phi}; C = c\cot\phi; \bar{\sigma} = \sqrt{J_2}; \sigma_m = -\frac{1}{3}I_1;$$

$\beta = \frac{1}{3}\text{asin}\left(\frac{-3\sqrt{3}J_3}{2\bar{\sigma}^3}\right)$ ^$-\frac{\pi}{6} \leq \beta \leq \frac{\pi}{6}$; β is the Lode angle; c and ϕ are the strength parameters; I_1 is the first invariant of the stress tensor σ_{ij}; J_2 and J_3 are the second and third invariants of the stress deviator s_{ij}.

An extension to the case of inherent anisotropy can be achieved by assuming that the strength descriptors in Eq. 4.16, η and C, are orientation dependent and have the representation analogous to that of Eq. 4.14. C is the strength under hydrostatic tension; therefore, it is independent of loading orientation. Thus, the effects of anisotropy can be attributed to variation in strength parameter η which will have the form analogous to Eq. 4.14.

The gradient operator can be expressed as:

$$\frac{\partial f}{\partial \sigma_{ij}} = \left(\frac{\partial f}{\partial \sigma_m} \frac{\partial \sigma_m}{\partial \sigma_{ij}} + \frac{\partial f}{\partial \bar{\sigma}} \frac{\partial \bar{\sigma}}{\partial \sigma_{ij}} + \frac{\partial f}{\partial \beta} \frac{\partial \beta}{\partial \sigma_{ij}} \right) + \left(\frac{\partial f}{\partial \eta} \frac{\partial \eta}{\partial \sigma_{ij}} \right) \tag{4.17}$$

The last parameter in Eq. (4.17) represents the influence of the loading orientation on plastic flow.

and,

$$\frac{\partial \eta}{\partial \sigma_{ij}} = 2 \, \eta_0 (1 + 2b_1 A_{ij} l_i l_j + 3b_2 (A_{ij} l_i l_j)^2 + \cdots) \frac{A_{ki}\sigma_{kj}\sigma_{pq}\sigma_{pq} - A_{pk}\sigma_{pq}\sigma_{kq}\sigma_{ij}}{(\sigma_{mn}\sigma_{mn})^2} \tag{4.18}$$

4.4.3 Derivation of η for the Tournemire argillite

The variations of strength descriptors, η and C, with θ are shown in Figs 4.11 and 4.12, respectively. In theory (Pietruszczak and Mroz, 2001), the strength descriptor C is invariant with respect to orientation of the sample (strength under hydrostatic tension). But, according to experimental data, it seems that there is a small variation in C with θ, between 8 ~ 13. For modeling purposes, a value of 10.5 can be considered.

In the case of uniaxial testing and for transversely isotropic materials, we can write:

$$A_{ij} l_i l_j = A_1 (1 - 3 \, l_2^2) \tag{4.19}$$

where $l_2^2 = cos^2 \alpha$

Therefore, using Eq. 4.14, the η descriptor can be expressed as a function of the loading orientation angle as follows.

$$\eta = \eta_0 \left[\begin{array}{c} 1 + A_1(1 - 3 \, cos^2\alpha) + b_1 A_1^2 (1 - 3 \, cos^2\alpha)^2 + \\ b_2 A_1^3 (1 - 3 \, cos^2\alpha)^3 + b_3 A_1^4 (1 - 3 \, cos^2\alpha)^4 \end{array} \right] \tag{4.20}$$

where $\alpha = 90 - \theta$, θ is the loading orientation angle.

Using the experimental data, described in Fig. 4.11, the values of different coefficients in the Eq. 4.20 are calculated:

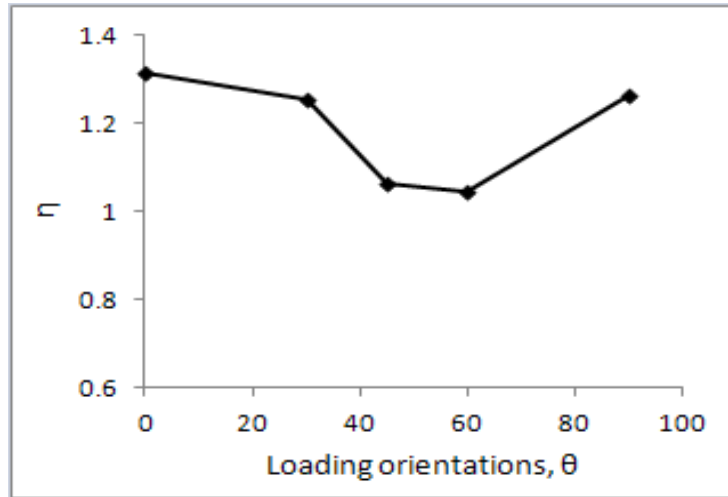$\eta_0 = 1.1849$, $A_1=0.236$, $b_1=0.217$, $b_2=-8.62$, and $b_3=-8.44$.

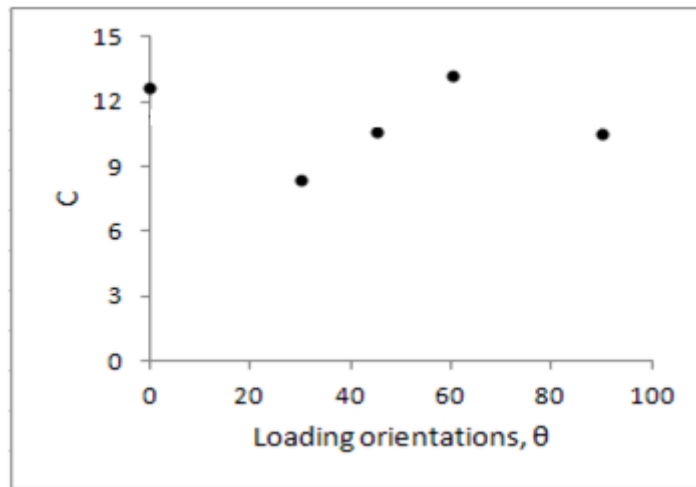Figure 4.11. Variation of η parameter with θ.

Figure 4.12. Variation of parameter C with θ.

4.5   Conclusions of Part 4

An elastoplastic model has been developed for simulating the mechanical behavior of transversely isotropic Tournemire argillite. The model is formulated based on the classical theory of plasticity and continuum damage mechanics concepts. The model requires the definition of a yield surface, flow rule, hardening law, a failure criterion, and a representation of damage caused by the initiation and propagation of the microcracks under stress. Currently, anisotropy has been handled in a piecewise manner, by using different input parameters for different loading orientations. This allows a best-fit determination of the parameters for different directions.

The capabilities of the model are evaluated by simulating uniaxial tests, triaxial tests with confining pressures, and unconfined and confined cyclic tests. Different confining pressures and loading orientations are considered. A fair agreement is obtained between numerical and experimental results. In particular, the ability of the model to handle strain hardening/softening and the degradation of the elastic stiffness due to damage is demonstrated.

Based on microstructure approach, Pietruszczak and Mroz (2001) extended the Mohr-Coulomb strength criterion and a flow rule to the case of inherent anisotropy. Here, the corresponding relevant orientation-dependent strength descriptors are derived. The microstructure approach seems to be promising and should be considered in a general formulation of the present model.

Part 5

Numerical Analysis of Excavation Damaged Zones around an Underground Opening in Sedimentary Rock

Ontario Power Generation (OPG Report – 1, 2008; OPG Report - 2, 2008) is planning to develop a DGR in southern Ontario to host low-level and intermediate-level (LILW) nuclear wastes. If approved, the proposed DGR is to be constructed at a depth of about 680 m within Ordovician Cobourg limestone. Shafts, tunnels, and a large number of underground emplacement rooms of rectangular shape are to be excavated. The extent of the EDZ needs to be determined for the considerations of mechanical instability and change in fluid flow characteristics of the host rock. This part of the report has two main sections dealing with: 1) Two and three dimensional numerical analyses of excavation damaged zones around the deep geologic repository at the Bruce site and 2) Coupled Hydro-Mechanical analysis of excavation damage zones around the deep geologic repository at the Bruce site

5.1 Two and three dimensional numerical analyses of excavation damaged zones around a deep geologic repository in sedimentary rock

The excavation and operation of potential radioactive waste repositories and the subsequent natural events can result in alterations of the Thermal (T)-Hydrological (H)-Mechanical (M)-Chemical (C) characteristics of the host rock. The excavation of the repository is possibly the main cause of mechanical disturbance, resulting in an excavation damaged zone (EDZ). It is necessary to know the size of the EDZ and the intensity of damage in the rock mass within the EDZ. This investigation shows (a) the differences between the results of two and three dimensional analyses and (b) the effect of the excavation of a second emplacement room on the extent of the EDZ.

5.1.1 Introduction

Deep geologic repositories (DGR) are being considered in many parts of the world to contain and isolate radioactive waste. The excavations of a DGR can result in damage in the rock and enhance rock mass permeability. The extent of the excavation damaged zones (EDZ) in the vicinity of the underground openings depends on the in-situ stresses, material properties, and excavation techniques. Field and laboratory studies and numerical analyses have been carried out by many researchers to assess the effect of the EDZ on the thermal, hydrological, mechanical, and chemical characteristics of rock masses (Sato et al. 2000, Souley et al. 1999, Bossart et al. 2004, Tsang et al. 2005, Nguyen 2007, and Kwon and Cho 2008). Underground research laboratories (URL) have been constructed in different countries including Canada, France, Switzerland, Belgium, Japan, Sweden, and South Korea. The types of rock formations encountered in these URL sites include crystalline rocks, rock salt, and argillaceous rocks.

The objectives of the present work are as follows: (1) to assess the extent of damage caused by the excavation of emplacement rooms, (2) to determine the differences in the results of 2D and 3D analyses with respect to stresses and deformations in the rock mass around a DGR, and (3) to evaluate the effect of the excavation of a second emplacement room on the extent of EDZ.

5.1.2 Geology at the DGR site

Figure 5.1 shows the rock formations at the site of the proposed DGR for LILW. The types of rock include carbonates, shale, evaporate and sandstone. The repository would be located at an approximate depth of 683 m in the Cobourg limestone with low permeability (lower

than 10^{-21} m^2). The groundwater at the repository level has a relatively high concentration of dissolved solids, and is saline. In-situ horizontal stresses at the proposed site are higher than the vertical stress. According to the regional data (OPG Report -1, 2008), the maximum in-situ horizontal stress is around 2 times the in-situ vertical stress. The minimum in-situ horizontal stress is about 1.1 times the in-situ vertical stress. In the analysis, it is conservatively assumed that the maximum in-situ horizontal stress is acting perpendicular to the axes of the emplacement rooms and the direction of the minimum in-situ horizontal stress is parallel to the axes of the emplacement rooms. In the present analyses, all emplacement rooms are excavated at the same elevation at a depth of 683 m below the ground surface. The emplacement rooms are of rectangular shape (7.5 m height x 8.1 m width), and the horizontal distance between the two adjacent emplacement rooms is 16 m.

5.1.3 Finite Element Models

Four rock layers around the emplacement rooms are included in the numerical analysis. These four layers (from the bottom up) are: Sherman Fall (layer 1), Weak Sherman Fall (layer 2), Cobourg (layer 3), and Shale (layer 4) as shown in Figure 5.2. The dimensions of the analysis domain are 120 m along the x-axis (horizontal) and 103 m along the y-axis (vertical) for 2D analysis. In the 3D analysis, the dimensions of the analysis domain are 120 m along the x-axis (horizontal), 40 m along the y-axis (horizontal), and 103 m along the z-axis (vertical).
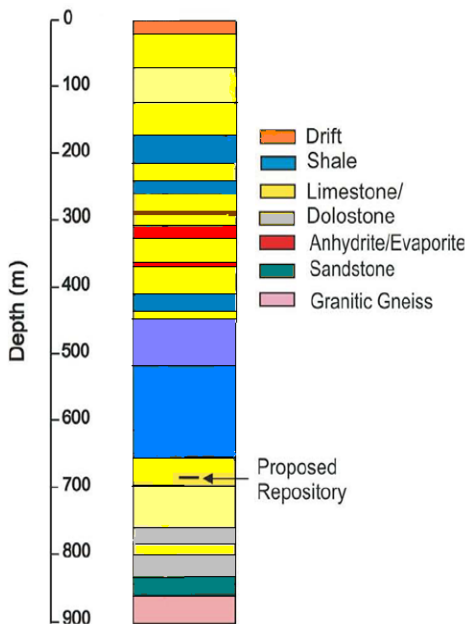

Figure 5.1. Rock formations (modified from Jensen et al. 2009)

84

The boundary conditions are as follows. The vertical boundaries are fixed horizontally, which means only vertical movements of the material are allowed at these boundaries. The top boundary is subjected to a uniform vertical load equivalent to the in-situ vertical stress. The base of the model is fixed. Plane strain conditions are imposed in 2D analysis.

5.1.4 Constitutive Relations and Parameters

Field and laboratory measurements of the geotechnical properties of the rock layers are obtained from open literature. The Drucker-Prager constitutive relation is used for all rock formations. For each rock layer, the average values of the elastic modulus, Poisson's ratio, unit weight, cohesion, and friction angle are required in the analysis. Table 5.1 summarizes the data used for these four layers (OPG Report - 2, 2008).
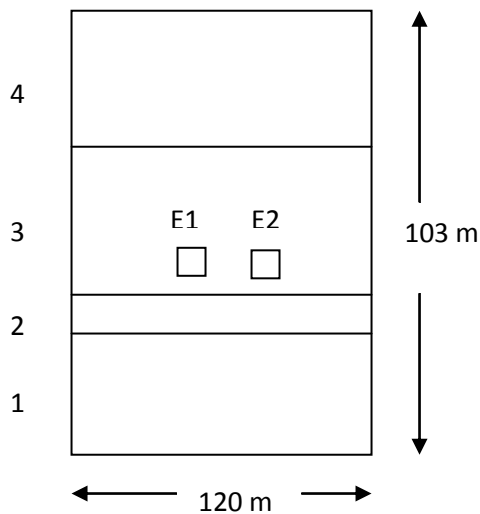
1 = Sherman Fall (30 m high)
2 = Weak Sherman Fall (10 m high)
3 = Cobourg (33 m high)
4 = Shale (30 m high)
E1 = Emplacement room-1
E2 = Emplacement room-2

Figure 5.2. Model geometry

Table 5.1. Geotechnical data (From OPG Report - 2, 2008)

Type of rock	E (GPa)	v	C (MPa)	Φ, deg
Sherman Fall	*26.45*	*0.23*	*12.4*	*45*
Weak Sherman	*10.74*	*0.08*	*6.23*	*45*
Cobourg	*36.04*	*0.19*	*19.09*	*45*
Shale	*7.3*	*0.09*	*6.46*	*45*

5.1.5 Results of Numerical Analyses

The numerical results are described in two sections. The first section consists of 2D results and the second section consists of 3D results. In this paper, only the data related to the various stress distributions, effective plastic strains, volumetric strains, shear strains, and displacements at the crown, the invert, and the springlines are presented. The sign convention for normal stresses plotted in the figures is as follows: a negative stress means compression and a positive stress means tension.

5.1.5.1 Two Dimensional Analysis

Two types of 2D analysis are carried out. In the first analysis, only one room is excavated (E1 in Fig. 5.2). The excavation process is simulated by gradually reducing the geotechnical properties of the excavated region, initial stresses, and body load from initial values to negligible values. In the second type of analysis, two rooms are excavated. The second room (E2 in Fig. 2) is excavated after completing the excavation of the first room (E1). The simulation of the excavation process for the second room followed the same procedure as the one used for the first room.

- **Excavation of one emplacement room**

Stress distributions (2D analysis)

Figure 5.3 shows the distribution of the vertical compressive stress after the excavation. Contour lines of the compressive stress with a magnitude less than 2e7 Pa are not plotted to maintain clarity. Before the excavation, the magnitude of the vertical compressive stress acting at the level of excavation was about 1.8e7 Pa. The vertical compressive stress acting on a horizontal surface extending from the right-bottom corner to the right boundary is plotted in Fig. 5.4. The horizontal line shown in this figure is the value of the vertical stress before the excavation. The magnitude of the maximum vertical compressive stress along this line is 3.4e7 Pa and it occurred at the corner of the emplacement room.
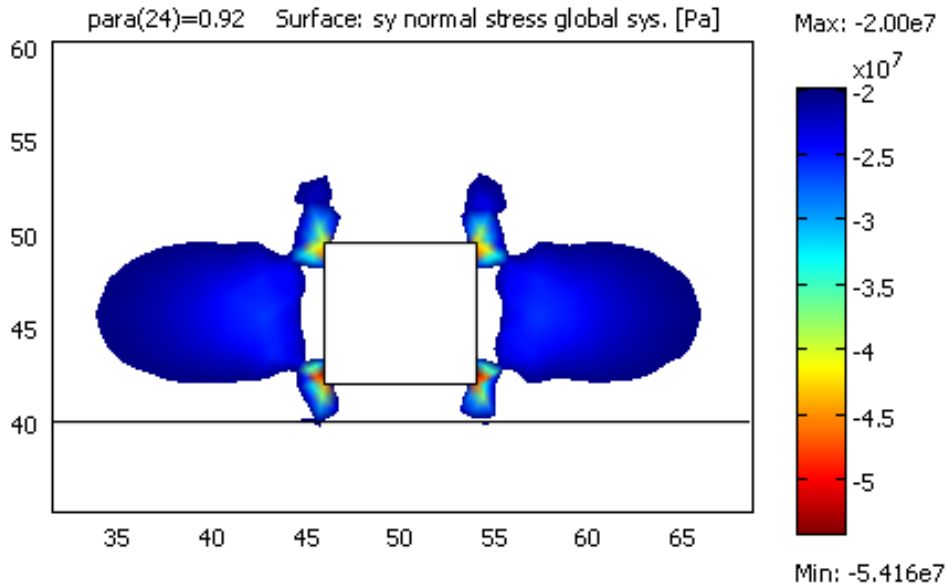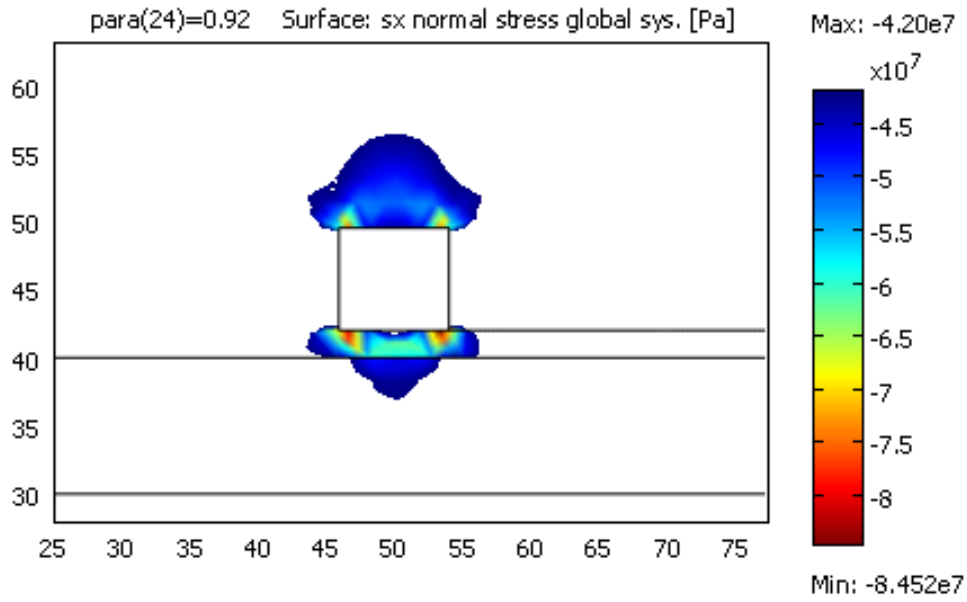

Figure 5.3. Distribution of vertical compressive stress after the excavation of the first room.
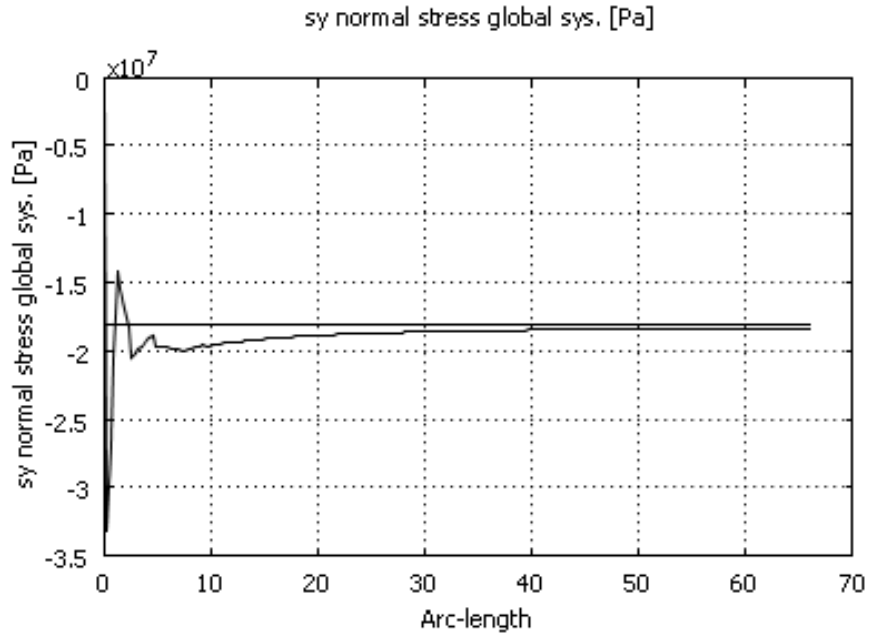
Figure 5.4. Variation of the vertical stress acting along a line between the right-bottom corner and the right boundary.

Figure 5.5 shows the distribution of the horizontal compressive stress at the end of the excavation. Before the excavation, the magnitude of the horizontal compressive stress acting at the level of excavation was about 3.6e7 Pa. The magnitude of the maximum horizontal compressive stress in the whole analysis domain is 8.45e7 Pa and it occurs at the corners of the emplacement room. Figure 5.6 shows an example of the variation of the horizontal stress at points along the line between the right-top corner and the top boundary. The nearly horizontal line shown in this figure represents the distribution of the horizontal compressive stress before the excavation. The magnitude of the maximum horizontal compressive stress is 6e7 Pa along this line.

Figure 5.5. Distribution of horizontal compressive stress after the excavation of the first room.
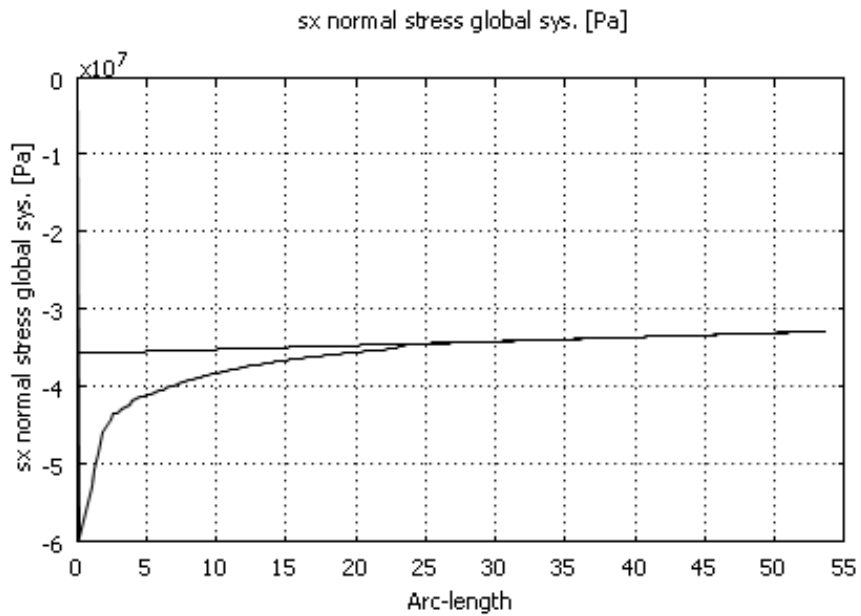
Figure 5.6. Variation of the horizontal stress acting along a line between the right-top corner and the top boundary.

Effective plastic strains (2D analysis)

Figure 5.7 shows the effective plastic strains greater than 0.0001, developed as a result of excavation. Plastic strains are developed at the corners of the room and within the weak Sherman Fall layer located at 2 m beneath the room. The calculated maximum value of plastic strain is 0.0022. The effective plastic strain (EPS) can be used as a measure of damage in the rock mass. Nguyen (2007) used EPS to predict changes in the permeability in the excavation damaged zone around a tunnel.

Volumetric strains (2D analysis)

Figure 5.8 shows the distribution of volumetric strains larger than 0.0001. Large expansive volumetric strains are
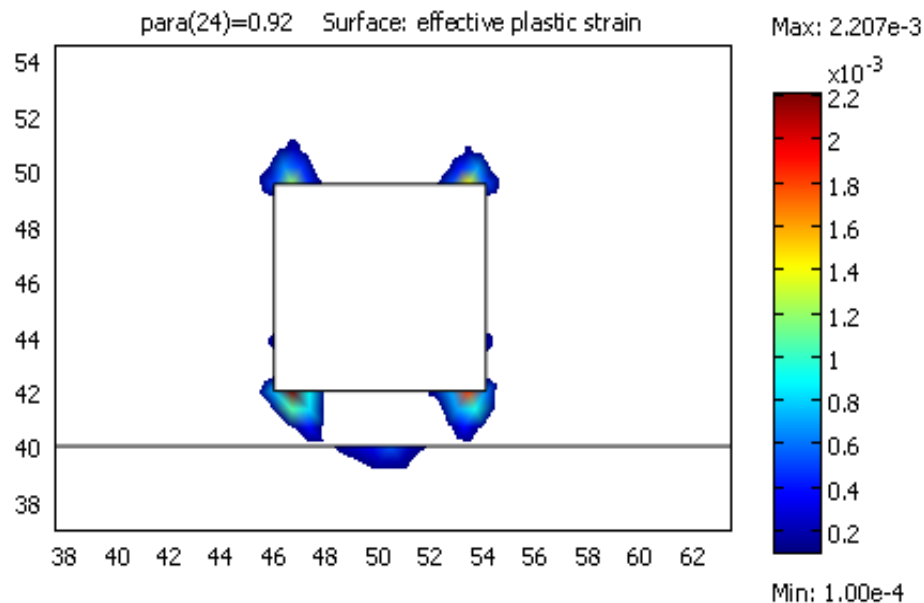
Figure 5.7. Distribution of effective plastic strains greater than 0.0001, after the excavation of the first room.

developed on the right and left sides of the room. Volumetric strains are also developed above and below the room and within the weak Sherman Fall layer located at 2 m beneath

the room. These results show that some expansion of the rock mass will occur and possibly the permeability of the material will increase as a result of the excavation.
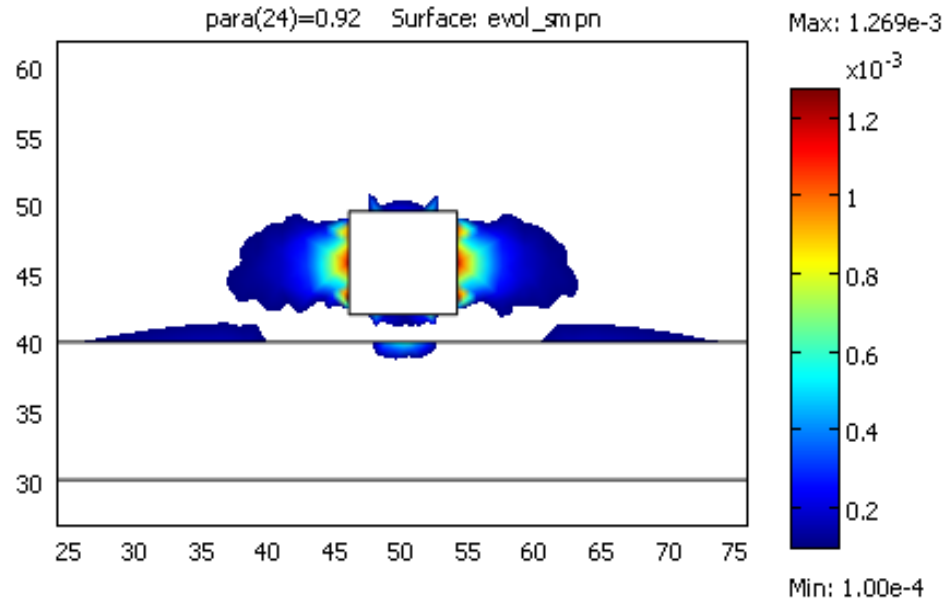

Figure 5.8. Distribution of volumetric strains greater than 0.0001, after the excavation of the first room.

- **Excavation of two emplacement rooms**

Stress distributions (2D analysis)

In the calculations, the second emplacement room is excavated after completing the excavation of the first room. Figure 5.9 shows the distribution of the vertical compressive stress after the excavation. The magnitude of the maximum compressive stress is 6.4e7 Pa and it occurred at the corners. Before the excavation, the magnitude of the vertical stress acting at the level of excavation was about 1.8e7 Pa. The vertical stress acting on a horizontal surface between the rooms is plotted in Fig. 10. The horizontal line shown in this figure is the magnitude of the vertical compressive stress before the excavation. The magnitude of the maximum compressive stress along this particular line is about 2.8e7 Pa and it occurred at a distance about 3 m away from the walls of the rooms.
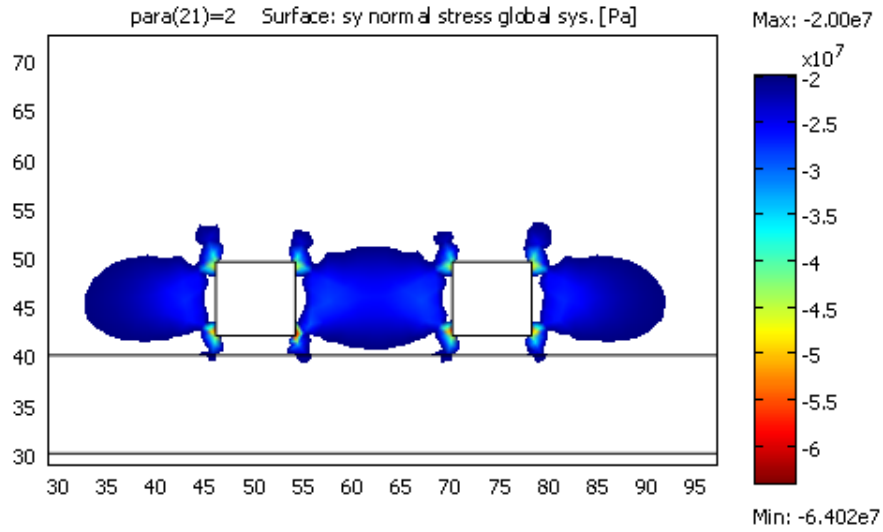
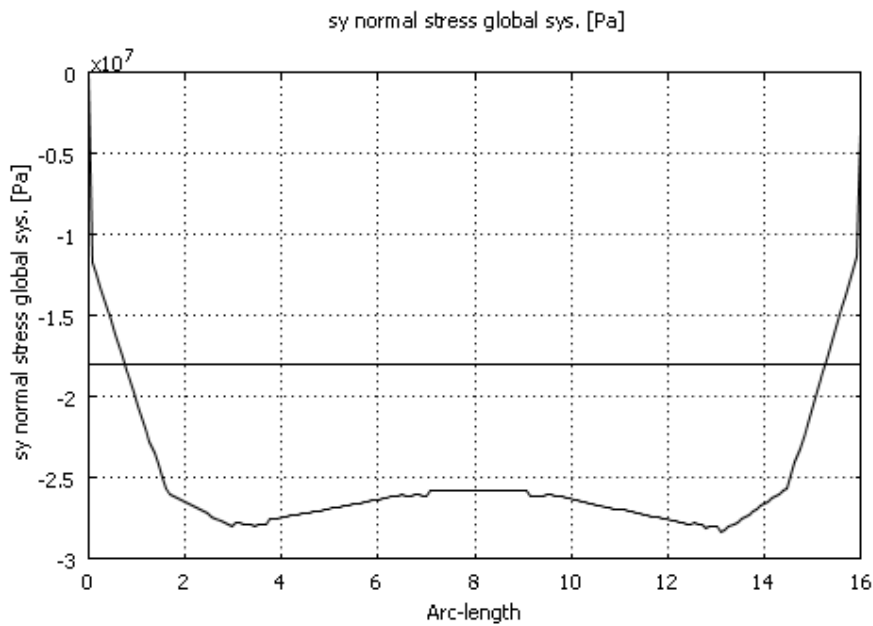Figure 5.9. Distribution of vertical normal stress after the excavation of two rooms

Figure 5.10. Variation of σ_y between the two rooms (at the level of springlines)

Figure 5.11 shows the distribution of the horizontal compressive stress at the end of the excavation. Before the excavation, the magnitude of the horizontal compressive stress acting

at the level of excavation was about 3.6e7 Pa. After the excavation, the magnitude of the maximum horizontal stress is 8.16e7 Pa and it occurs at the corners of the rooms.
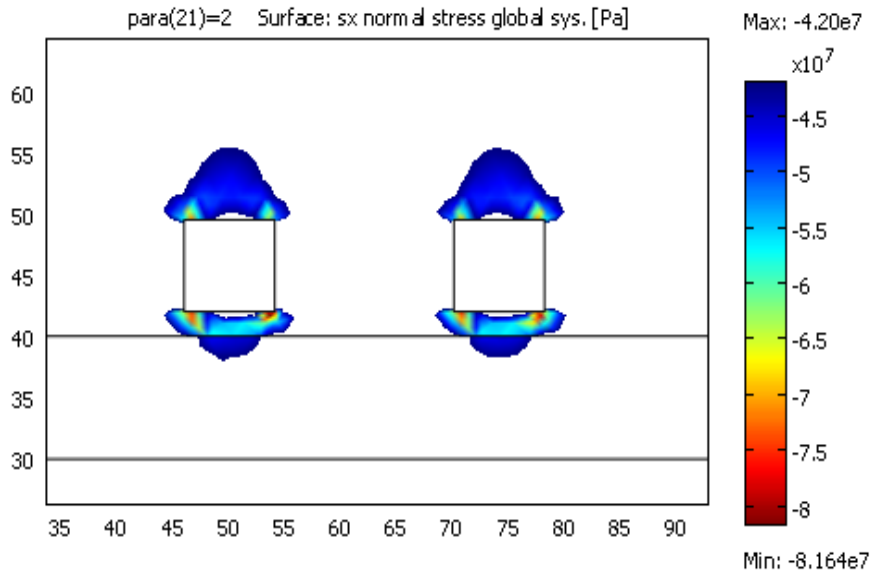

Figure 5.11. Distribution of horizontal compressive stress after the excavation of two rooms.

Effective plastic strains (2D analysis)

Figure 5.12 shows the distribution of the effective plastic strains, greater than 0.0001, after the excavation. Areas of plastic strains are developed at the corners of the rooms and within the weak Sherman Fall layer located at a distance of 2 m underneath the rooms.
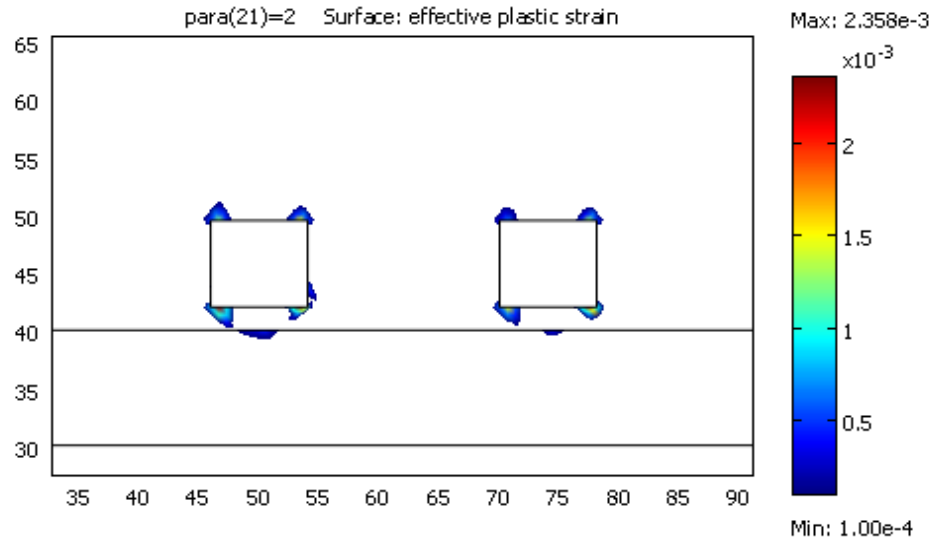
Figure 5.12. Distribution of plastic strains greater than 0.0001, after the excavation of two rooms.

Volumetric strains (2D analysis)

Figure 5.13 shows the distribution of volumetric strains greater than 0.0001. Large volumetric strains are developed on the right and left sidewalls, below and above the rooms, and within the weak Sherman Fall layer located at 2 m below the rooms.
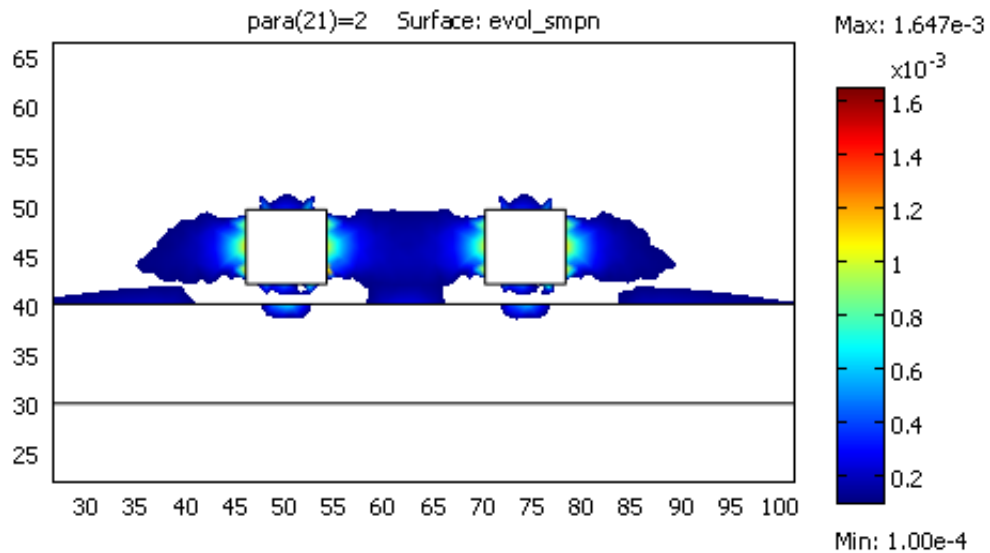

Figure 5.13. Distribution of volumetric strains greater than 0.0001, after the excavation of two rooms.

Shear stresses (2D analysis)

Figure 5.14 shows contours of shear stresses which are developed as a result of excavation. The top-left and bottom-right corners of the rooms are subjected to negative shear stresses, while the remaining corners are subjected to shear stresses with positive sign.

5.1.5.2 Three Dimensional Analyses

3D simulations are also carried out for the excavation of one and two emplacement rooms. In the first case, only one room is excavated (Room E1 in Fig. 5.2). As in 2D analysis, the room has a rectangular cross section (8.1 m in the x-direction and 7.5 m in the z-direction) and has a length of 10 m (in the y-direction). The excavation process is simulated by dividing the room into 10 slices. The simulation of the excavation is carried out by gradually reducing the values of the parameters of geotechnical properties, initial stresses, and body load from initial values to negligible values. In order to simulate the construction stages, the first slice is excavated starting at the room face.
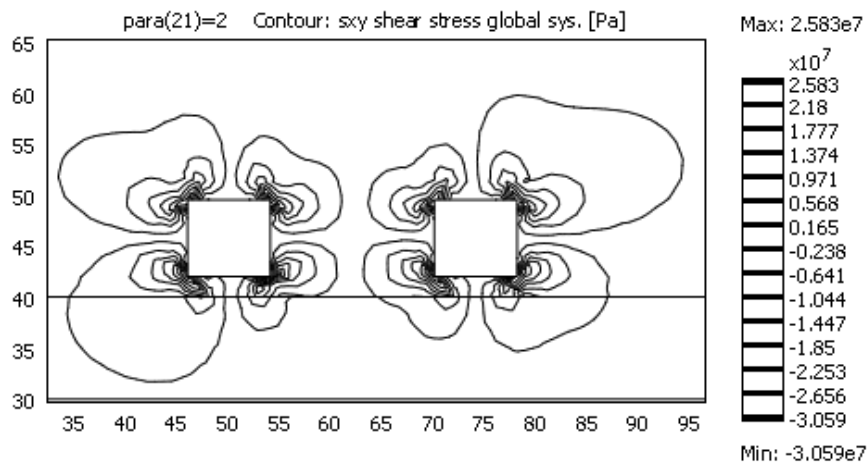

Figure 5.14. 2D contours of shear stresses after the excavation of two rooms.

This process is repeated sequentially for all slices until the tenth slice. Similar to the 2D analyses, two types of simulations are carried out. In the first type of analysis, only one room is excavated (E1 in Fig. 5.2). In the second type of analysis, two rooms are excavated one after the other but not simultaneously. The second room (E2 in Fig. 5.2) is excavated after completing the excavation of the first room (E1). The horizontal distance between the two rooms is 16 m. The simulation of the excavation process for the second room followed the same procedure as the one used for the first room.

- **Excavation of one emplacement room**

Stress distributions (3D analysis)

Stress states in the rock around the emplacement rooms change each time when a slice of the rock mass is removed from the analysis domain. Figure 5.15 shows the distribution of the vertical compressive stress after the excavation of the emplacement room E1.
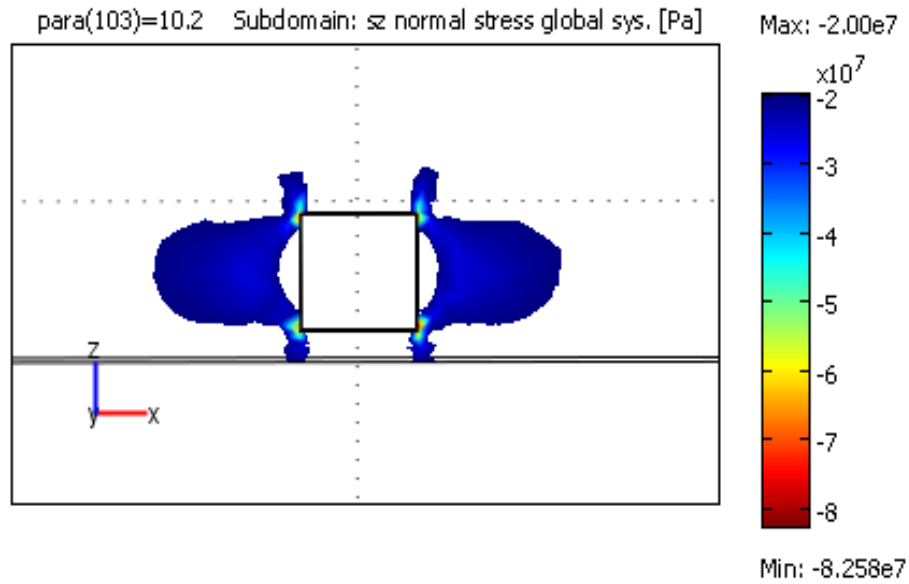

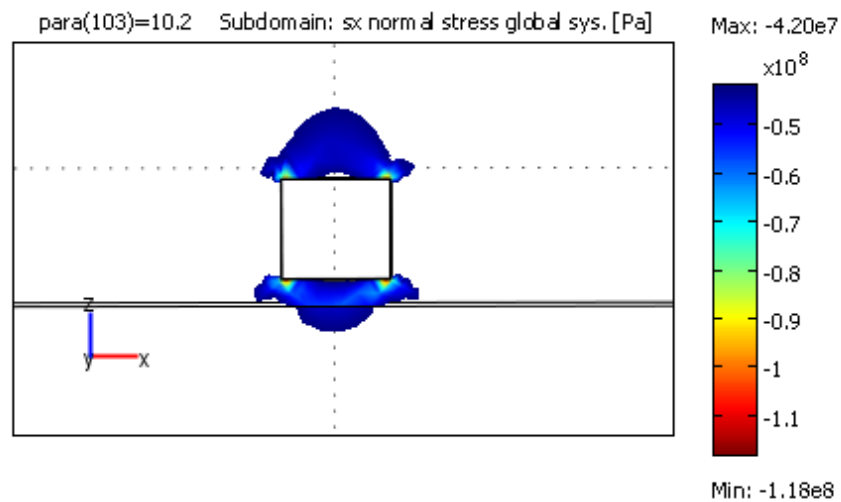Figure 5.15. Distribution of vertical compressive stress after the excavation.

Figure 5.16. Distribution of σ_x after the excavation.

Figure 5.16 shows the distribution of the horizontal compressive stress after the excavation. High stresses shown in Figures 5.15 and 5.16 start to develop at the room face and the magnitude of stresses depends on the excavation stages. The maximum vertical compressive stress (8.25e7 Pa) and the maximum horizontal compressive stress (11.8e7 Pa) are developed at the corners of the room.

Effective plastic strains (3D analysis)

Figure 5.17 shows the effective plastic strains greater than 0.00004, developed after the excavation. Plastic strains are developed at the corners of the room. The highest value of plastic strains is around 0.001.
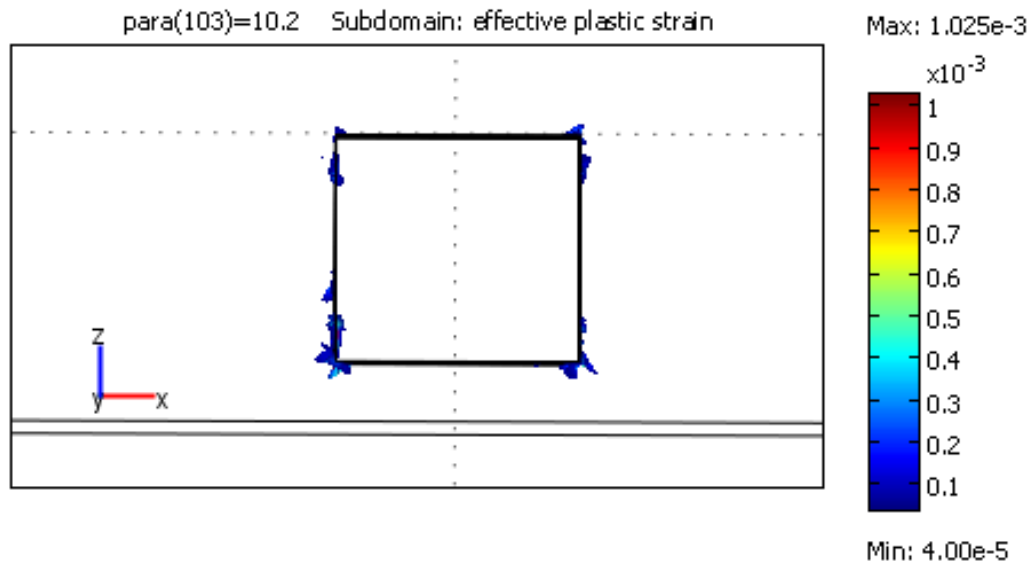

Figure 5.17. Distribution of effective plastic strains greater than 0.00004.

Volumetric strains (3D analysis)

Figure 5.18 shows the distribution of expansive volumetric strains greater than 0.0001, after the excavation. Largest volumetric strains are developed on the right and left sides of the room, underneath and above the room, and also within the weak Sherman Fall layer.
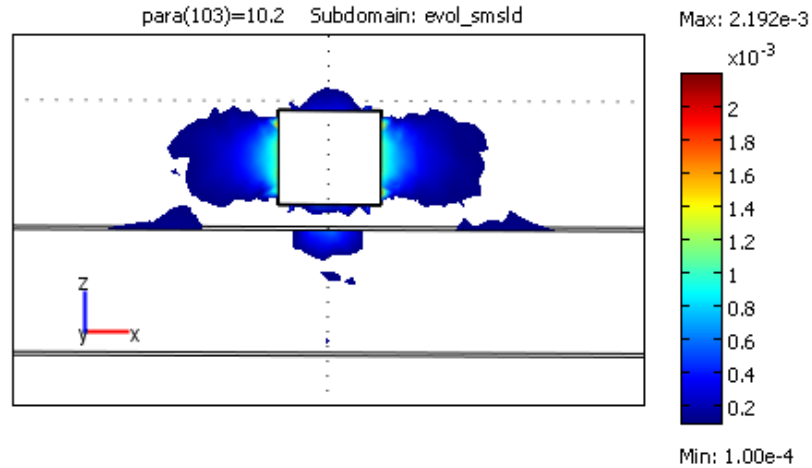
Figure 5.18. Distribution of volumetric strains greater than 0.0001,

- **Excavation of two emplacement rooms**

Stress distributions (3D analysis)

The second room is excavated after completing the excavation of the first room. Figures 5.19 and 5.20 show the distribution of vertical and horizontal stresses after the excavation. High stresses develop around the first emplacement room where the excavation starts first. As the excavation advances in the horizontal direction, the intensity of the stresses change and the size of the highly stressed areas of rock become larger along the emplacement room. The excavation of the second room has no significant additional effect in terms of the development of high stresses.
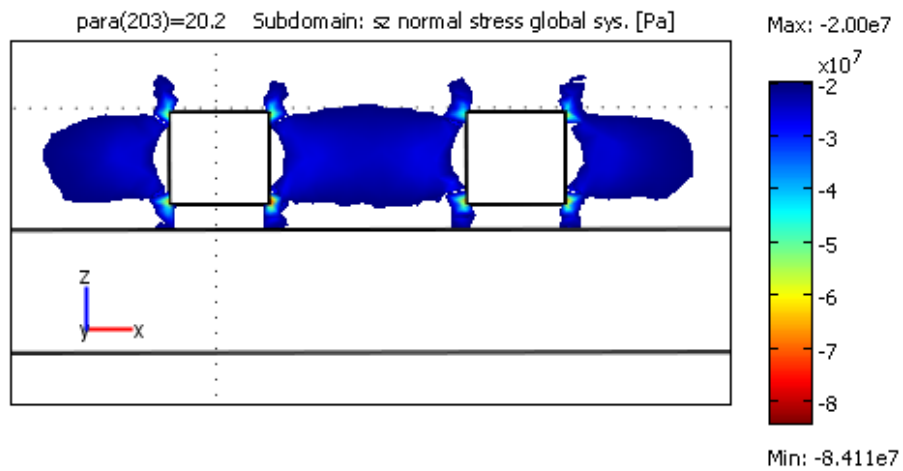

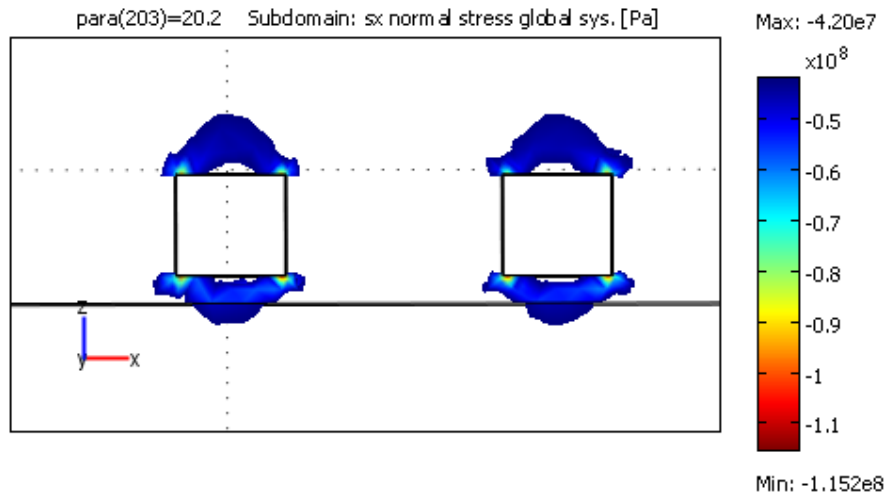Figure 5.19. Distribution of σ_z after excavating two rooms.

Figure 5.20. Distribution of σ_x after excavating two rooms.

Effective plastic strains (3D analysis)

Figure 5.21 shows the distribution of effective plastic strains greater than 0.00004. Plastic strains are larger at the corners of the rooms. The size of the regions of large plastic strains depends on the excavation stages. The maximum value of the effective plastic strain is around 0.002.
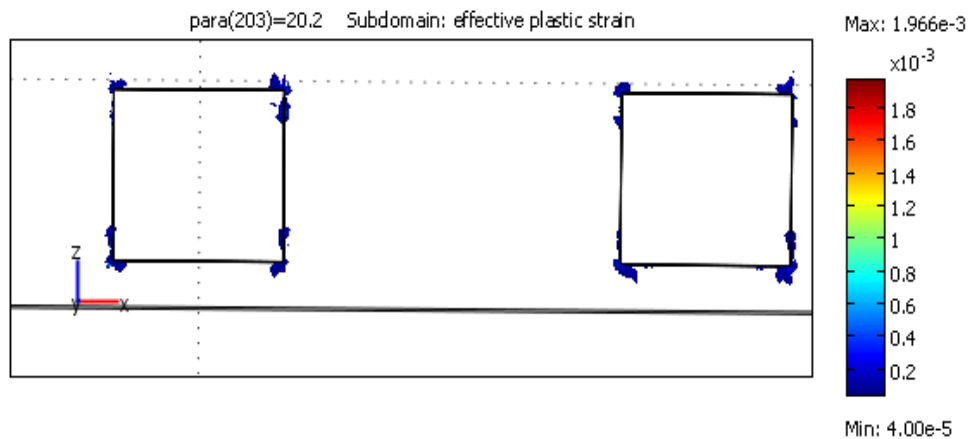

Figure 5.21. Distribution of effective plastic strains greater than 0.00004, after excavating two rooms.

Volumetric strains (3D analysis)

The distribution of expansive volumetric strains greater than 0.0001, is shown in Figure 5.22. Large volumetric strains are developed on the right and left sides of the rooms, underneath and above the rooms, and also within the weak Sherman Fall layer. Figure 5.23 shows the magnitude of the volumetric strains between the springlines of two rooms.
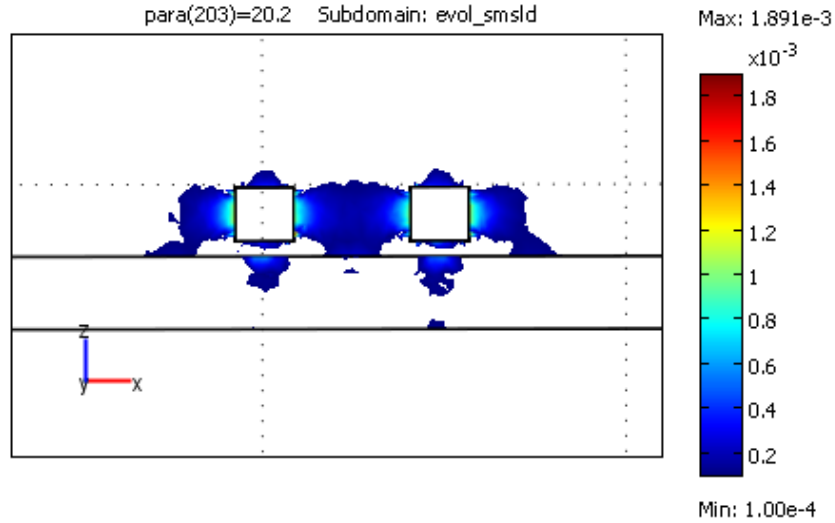

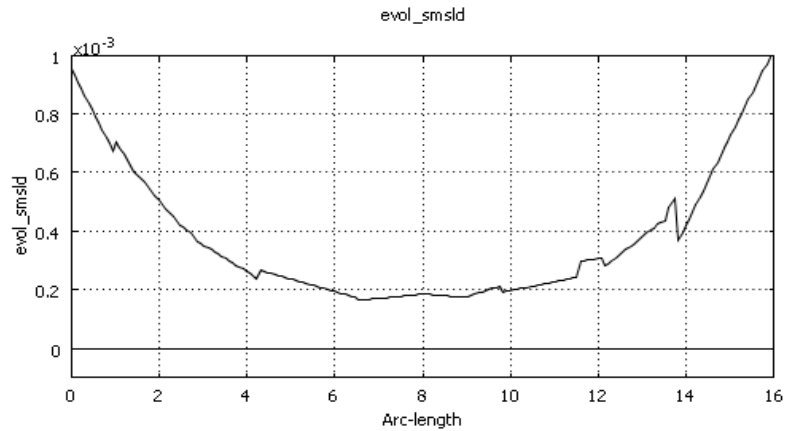Figure 5.22. Distribution of volumetric strains greater than 0.0001.

Figure 5.23. Variation of volumetric strains between the two rooms (spring line).

Shear strains (3D analysis)

Table 5.2 lists the values of shear strains, obtained from 2D and 3D analyses, at the corners of the rooms. Negative shear strains are calculated for the top-left and bottom-right corners of the rooms. Whereas, positive shear strains are calculated for the top-right and bottom-left corners of the rooms. The excavation of the second room causes development of slightly more shear strains.

Table 5.2: 2D and 3D shear strains at the top-left-corner (TLC), top-right-corner (TRC), bottom-left-corner (BLC), and bottom-right-corner (BRC) of the rooms.

Shear Strain, $x10^{-3}$ TLC		TRC	BLC	BRC
2D Analysis (one room)	-2.2	2.2	2.6	-2.6
3D Analysis (one room)	-2.6	2.6	2.8	-2.8
2D Analysis (two rooms)				
Room 1	-2.2	2.1	2.6	-2.8
Room 2	-2.0	2.3	2.5	-2.7
3D Analysis (two rooms)				
Room 1	-2.5	2.5	2.7	-3.2
Room 2	-2.5	2.5	2.7	-3.1

 Table 5.3 gives the displacements calculated at the crown, the invert, and springlines of one and two rooms. The numbers correspond to both the 2D and 3D analyses of the displacements at the face of the rooms. According to 2D analysis, inward displacements of about 6.3, 9.4, and 9.2 mm are generated on the floor and the left and right sides of the rooms, respectively. The downward displacement at the crown is around 4 mm. The excavation of the second room cause more displacements in the roofs of both rooms (up to 40%), less displacement on the right-side of the first room (-30%), and less displacement on the left-side of the second room (-30%). 2D analysis predicts up to 30% more displacements than the 3D analysis.

Table 5.3: 2D and 3D displacements (mm) at the crown (YDC), the invert (YDI), left springline (XDLS), and right springline (XDRS) for one and two rooms.

Displacement (mm)	YDC	YDI	XDLS	XDRS
2D Analysis (one room)	3	6.3	8.5	8.5
3D Analysis (one room)	2.8	6.2	7.5	7.5
2D Analysis (two rooms)				
Room 1	4.3	6.2	9.4	5.5
Room 2	4.3	6.2	5.5	9.2
3D Analysis (two rooms)				
Room 1	3.2	6.4	7.8	5.7
Room 2	3.2	6.4	5.7	7.8

Table 5.4: Inward displacements (mm) of rock mass along the length of emplacement rooms.

y-distance	0 m	4m	6 m	8 m	10 m
One Emplacement Room					
Crown	2.8	2.7	2.6	2.2	0.3
Invert	6.2	6	5.9	4.1	1.1
Springline (left)	7.5	7.1	6.6	5.5	1.8
Springline (right)	7.5	7.2	6.7	5.6	2
Two Emplacement Rooms					
Room 1					
Crown	3.2	3.2	2.8	2.5	0.6
Invert	6.4	6.2	5.5	4.2	1
Springline (left)	7.8	7.5	7	6	2.1
Springline (right)	5.7	5.5	5.2	4.4	1.1
Room 2					
Crown	3.2	3.1	2.9	2.4	0.6
Invert	6.4	6	5.5	4.1	1.1
Springline (left)	5.7	5.6	5.3	4.5	1.1
Springline (right)	7.8	7.5	7	5.8	2.3

According to the data of 3D analysis reported in Table 5.4, most of the deformation produced by excavation at any point in the emplacement room takes place by the time the excavation moves 4 meters away from this point.

5.1.6 Conclusions

The conclusions of this numerical study are as follows:

- Due to the excavation, high vertical and horizontal stresses are developed at the corners and close to the walls of the rooms. The amount of increase in the vertical stress is up to 300% as compared to the far field stresses. Similarly, the increase in the horizontal stress is up to 200%. The highest stresses are calculated at the corners of the rooms for both 2D and 3D analyses.
- Large volumetric strains, effective plastic strains, and shear strains are developed around the rooms, in between the rooms and within the weak Sherman Fall layer. In these areas of high strains, the rock mass is expected to experience damage. In the excavation damaged zones, it is likely to see a reduction in the strength of rock mass, increase in crack population, expansion of the existing fractures, and increase in the hydraulic conductivity of the material.
- For 3D analysis, most of the deformation produced by excavation at any point in the emplacement room takes place by the time the excavation moves 4 meters away from this point.
- The size of the EDZ can be approximated as follows: about 5 m on the left side, right side, and below the rooms, and 3 m above the roof of the rooms.
- The excavation of the second room increases the size of the EDZ above the rooms.
- Areas of volumetric strains and plastic strains are developed in the Weak Sherman Fall layer located at 2 m below the base of the emplacement rooms.
- In general, 2D analysis predicts slightly higher values of displacements and effective plastic strains than 3D analysis. On the other hand, 3D analysis predicts slightly higher values of stresses and volumetric strains than 2D analysis.

5.2 Coupled Hydro-Mechanical Analysis of Excavation Damage Zones around an Underground Opening in Sedimentary Rock

5.2.1. Introduction

In this section, a coupled hydro-mechanical analysis is performed to evaluate the short and long term stability of an isolated rectangular emplacement room. The Hoek-Brown parameters are used to obtain the friction angle and cohesion for various types of rocks. An expression relating the changes in the permeability of the rock mass to the equivalent deviatoric strain is used in the hydro-mechanical analysis. The objectives of the present work are as follows: (1) to determine the effect of excavation on stress and strain distributions, (2) to evaluate the effect of time on the short and long term pore pressure response, and (3) to assess the effect of rock damage on hydraulic processes around an emplacement room.

5.2.2 Geology and hydrogeology at the DGR site

Rock formations at the site of the proposed DGR include layers of argillaceous limestone, shale, evaporate and sandstone. The proposed repository is to be located at an approximate depth of 683 m in the Cobourg limestone with high-strength and low permeability (lower than 10^{-21} m^2). Based on the available regional data, it is assumed that the maximum in-situ horizontal stress at the level of the excavation is around 2 times the in-situ vertical stress. The minimum in- situ horizontal stress is nearly 1.2 times the in-situ vertical stress. In the analysis, it is conservatively assumed that the maximum in-situ horizontal stress is acting perpendicular to the axes of the emplacement room and the direction of the minimum in-situ horizontal stress is parallel to the axes of the emplacement room. The permeability in the horizontal direction at the location of the repository is assumed to be ten times higher than the permeability in the vertical direction.

In this numerical analysis, only four rock layers that surround the emplacement room are included in the analysis. Figure 5.24 describes the model geometry. These four layers (from the bottom-up) are: a 30 m thick Sherman Fall (SF) layer (layer 1), a 10 m thick Weak Sherman Fall (WSF) layer (layer 2), a 33 m thick Cobourg (C) layer (layer 3), and a 30 m thick Shale (S) layer (layer 4). The emplacement room, which is indicated as EMR in Fig. 1, is of a rectangular shape (8.6 m width x 7 m height), and it is located in the Cobourg formation. The dimensions of the analysis domain are 100 m along the x-axis (horizontal) and 103 m along the y-axis (vertical).

The preliminary results of in-situ measurements of the hydraulic conductivity and pore pressure (Avis et al., 2009) are shown in Figure 5.25. Preliminary pore pressure measurements were 5.06 MPa and 6.5 MPa at the top and bottom boundaries in Figure 5.24, respectively. For simplification, it is assumed in this paper, that the pore pressure distribution as a function of depth is linear. The measured values of hydraulic conductivity varied between 10^{-14} m/s and 10^{-13} m/s in the rock units at the proposed repository location.
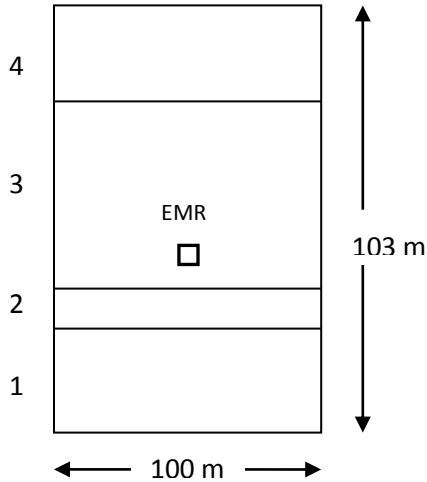

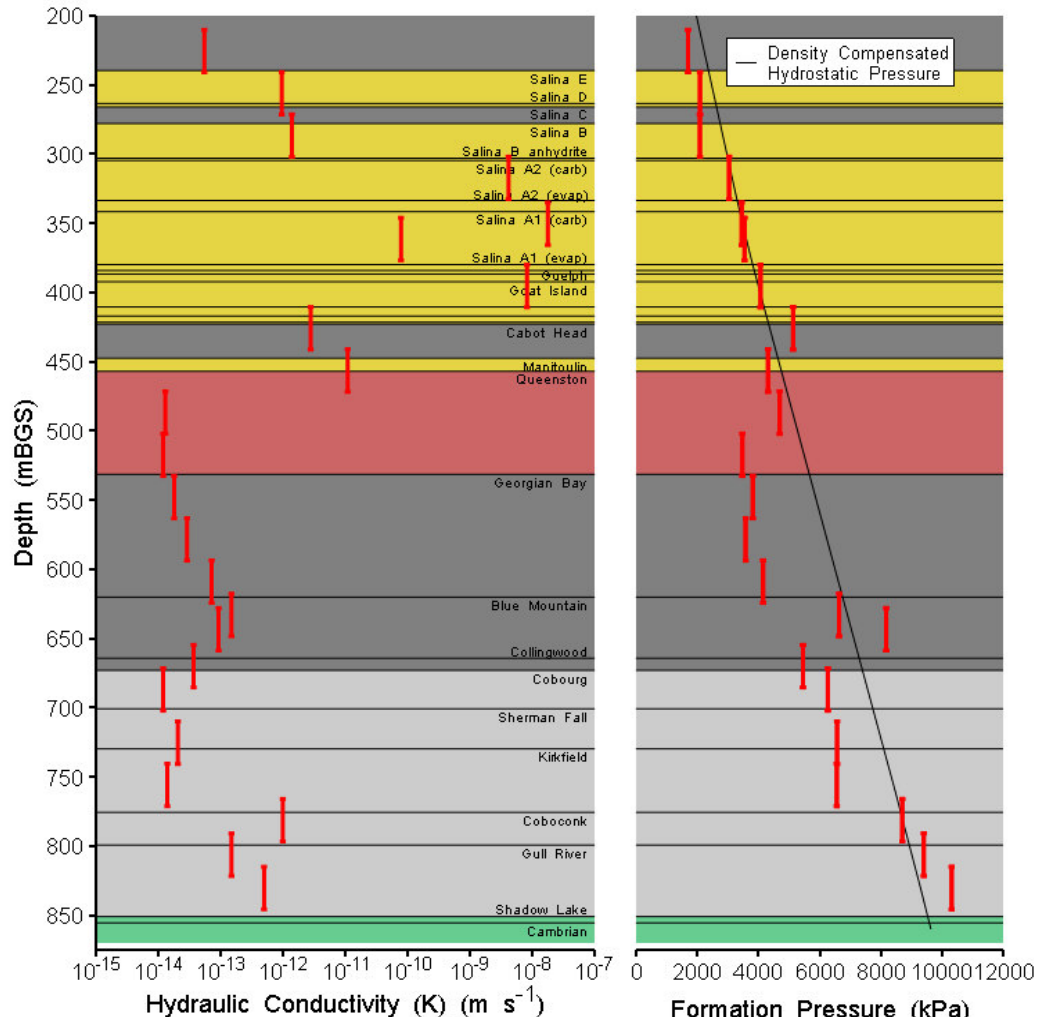Figure 5.24. Rock layers and an isolated emplacement room EMR.

Figure 5.25. Rock layers, hydraulic conductivities and pore pressures determined by field investigations (Avis et al., 2009).

5.2.3. Finite Element Model

The two dimensional stability analysis of an isolated emplacement room is carried out using the COMSOL Multiphysics code, version 3.5.

5.2.4. Constitutive relations and parameters

Geotechnical properties of the rock layers are obtained from OPG Report – 1 (2008). The friction angles and the cohesions are calculated from the Hoek-Brown parameters.

107

Table 5.5. Geotechnical data used in the FE analysis.

Rock Type	E (GPa)	v	UCS (MPa)	c (MPa)	Φ deg
SF	26.45	0.23	59.88	4.02	36.5
WSF	10.74	0.08	35.76	2.3	34.89
C	36.04	0.19	109.74	9.32	41.34
S	7.3	0.09	31.17	2.04	31.73

E: Young's modulus; v: Poisson's ratio; UCS: uniaxial compressive strength; c: cohesion;

Φ: friction angle.

Subsequently, the parameters are given as input for the Drucker-Prager elasto-plastic constitutive relation. Table 1 summarizes the data used for the four layers.

5.2.5 Governing equations

Conservation of Mass:

$$\left[C_s\,(1-\theta)+C_f\,\theta\right]\frac{\partial p}{\partial t}+\nabla.\left[-\left(\frac{K_s}{\mu}\right)(\nabla p+\rho_f\,g\,\nabla D)\right]=-\alpha_b\,\frac{\partial\epsilon_{vol}}{\partial t} \tag{5.1}$$

Conservation of Momentum:

$$\nabla.\boldsymbol{\sigma}+\alpha_b\nabla p+\boldsymbol{F}=0 \tag{5.2}$$

where

C_s & C_f = compressibility of solid and fluid; θ= porosity; K_s= permeability; μ= viscosity; ρ_f = density of the fluid; g= acceleration of gravity; ∇D= unit vector in the direction of g; p= fluid pressure; $\boldsymbol{\sigma}$= stress tensor; $\boldsymbol{F}$= Body force vector; α_b= Biot-Willis coefficient (It is assumed to be 0.8 for the limestone; ϵ_{vol}= volumetric strain.

The boundary conditions are as follows. Only vertical movements are allowed at the vertical boundaries of the analysis domain. The top boundary is subjected to a uniform vertical

effective stress equivalent to the in-situ vertical effective stress (13 MPa), while the vertical boundaries are subjected to uniform horizontal effective stresses equivalent to the maximum in-situ stress (30 MPa). The base of the model is fixed. Plane strain conditions are imposed. The room is maintained at atmospheric pressure, while the other boundaries are maintained at constant pressures equal to the initial pressures prior to excavation.

5.2.6 Results of Analysis

In this section, the data related to the stress and strain distributions, displacements, and pore pressure evolution are discussed. The sign convention adopted is as follows: the compressive normal stress plotted in the figures is negative and the tensile stress is positive.

Stress distribution

Figure 5.26 shows the distribution of the vertical compressive effective stress after 2 years from the excavation. Contour lines of the compressive effective stress with a magnitude less than 2e7 Pa are not plotted to maintain clarity. The magnitude of the maximum vertical compressive effective stress in the whole analysis domain is 5.1e7 Pa and it occurred at the corners of the emplacement room.

Figure 5.27 shows the distribution of the horizontal compressive effective stress after two years from the excavation. The magnitude of the maximum horizontal compressive effective stress is 8.6e7 Pa and it occurs at the corners of the emplacement room. The results indicate that the corners of the room and the areas above and below the room are subjected to high compressive stresses.
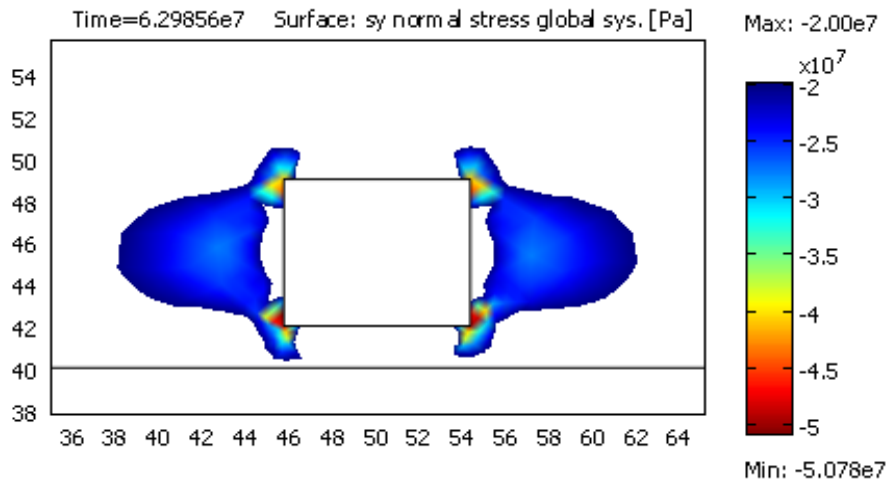
Figure 5.26. Distribution of σ_y' after two years from the excavation (less than -2e7 Pa).
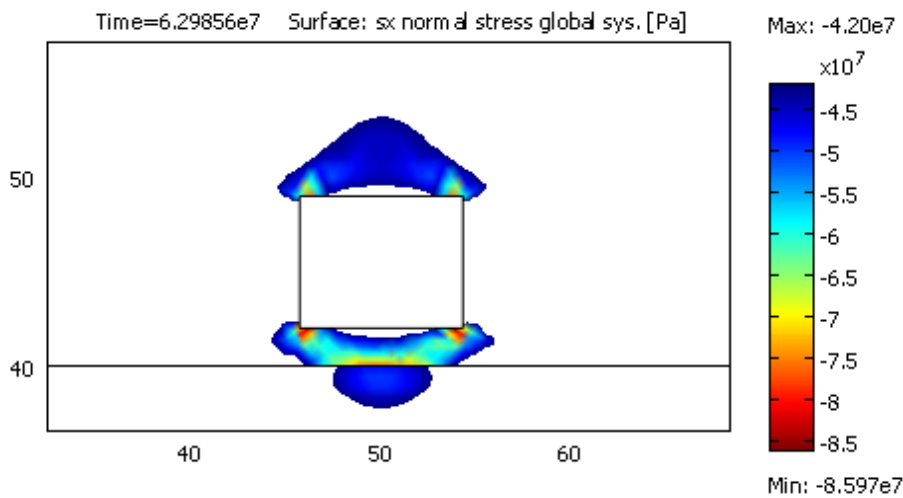

Figure 5.27. Distribution of σ_H' after two years from the excavation (less than -4.2e7 Pa).

Effective plastic strain distribution

The effective plastic strains caused by the excavation are shown in Figure 5.28 ($\varepsilon_p > 0.0001$). Largest plastic strains are developed at the corners of the room. Plastic strains also developed at locations above and below the room and within the weak Sherman Fall layer. The calculated maximum value of effective plastic strain at the corners is about 0.0095.
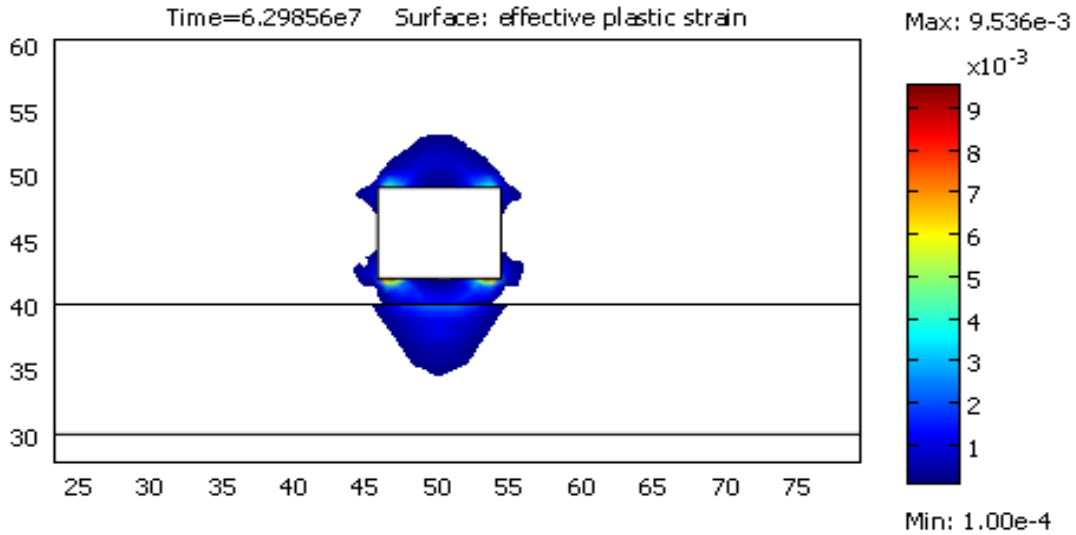
110

Figure 5.28. Distribution of the effective plastic strain (greater than 0.0001).

Volumetric strain distribution

Figure 5.29 shows the distribution of the volumetric strain at time of 2 years. Expansive volumetric strains are developed on both sides of the room, above and below the room, and within the weak Sherman Fall layer. Compressive volumetric strains are developed at the corners of the room. The expansion of the material can cause an increase in the hydraulic conductivity of the material.
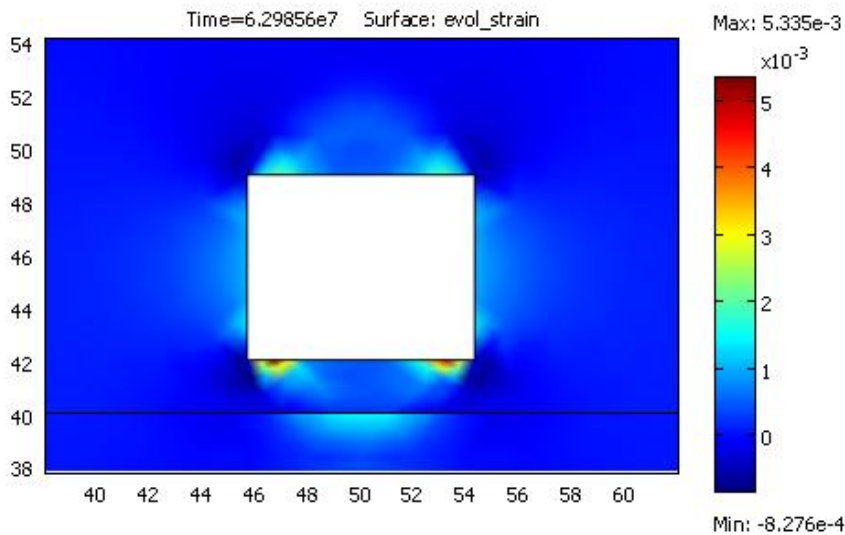

Figure 5.29. Distribution of the volumetric strain

Displacements

Table 5.6 describes the variation of the displacements with time at the crown, the invert, and the spring lines (Spr.). At the spring lines, a maximum inward horizontal displacement of about 8.3 mm is calculated at the end of the excavation. It seems that this displacement is not affected much by time and it remains at a value of 8.5 mm after 10 years. The maximum vertical displacement is 4.3 mm at the crown and 9.3 mm at the invert at the end of the excavation.

Table 5.6. Displacements versus time at the crown, invert, and spring lines.

Time	Crown (mm)	Invert (mm)	Springline (mm)
15 days	4.3	9.3	8.3
2 months	4.3	9.3	8.3
1 years	4.5	9.8	8.4
2 years	4.6	10	8.4
5 years	5	10.6	8.5
10 years	5.4	11.2	8.5

Table 5.7. Variation of strains with time.

Time	EPS Corner (10^{-3})	EPS Invert (10^{-3})	VS Corner (10^{-3})	VS Invert (10^{-3})
15 days	3.8	0.28	0.45	0.6
2 months	4.3	0.27	0.8	0.6
1 yr	5.7	0.29	1.56	0.59
2 yrs	6.2	0.24	2.1	0.58
5 yrs	7.1	0.14	2.65	0.59
10 yrs	7.5	0.1	3.1	0.57

These displacements increased with time and reached values of about 5.4 mm and 11.2 mm for the crown and the invert after ten years. The results indicate that the EDZ is not uniform

around the room and the displacements can increase with time at some locations within the EDZ.

Variation of strains with time

Table 5.7 describes the variation of the effective plastic strain (EPS) and the volumetric strain (VS) with time at the bottom left corner and the invert of the emplacement room. After ten years from the excavation, the effective plastic strain at the corner almost doubled while the volumetric strain increased five times. At the invert, no significant increase is calculated for both effective plastic strain and volumetric strain. This indicates that the degree of change in strains with time is not the same in all locations within the EDZ.

Pore pressure generation and dissipation

At the end of the excavation the pore pressure at the boundaries of the room reduces to the atmospheric pressure and the room acts as a sink. The shape of the excavation has an effect on the response of the rock mass to an excavation.

The damage to the rock affects the flow characteristics of the material. In the present analysis, two cases of permeability are considered. In the first case, the permeability is kept constant which means the effect of the mechanical damage on permeability is neglected. In the second case, the effect of damage on permeability is considered by expressing the permeability as a function of the equivalent deviatoric strain.

Case 1: Constant permeability

The pore pressure (PP) at the level of the emplacement room before the excavation was around 5.9e6 Pa. For clarity, in the following figures only the pore pressures greater than 5.9e6 Pa are plotted. Figure 5.30 shows the PP generated at the end of the excavation. High PPs are developed in the highly compressed areas. The maximum pore pressure is around 2.3e7 Pa and it is developed at the corners of the emplacement room. Most of the PP is dissipated after two years from the excavation as can be seen in Figure 5.31.

As soon as the excavation begins, the pore pressure starts to change and redistribute in the surrounding areas. Figure 5.32 shows PP distribution two months after the excavation.
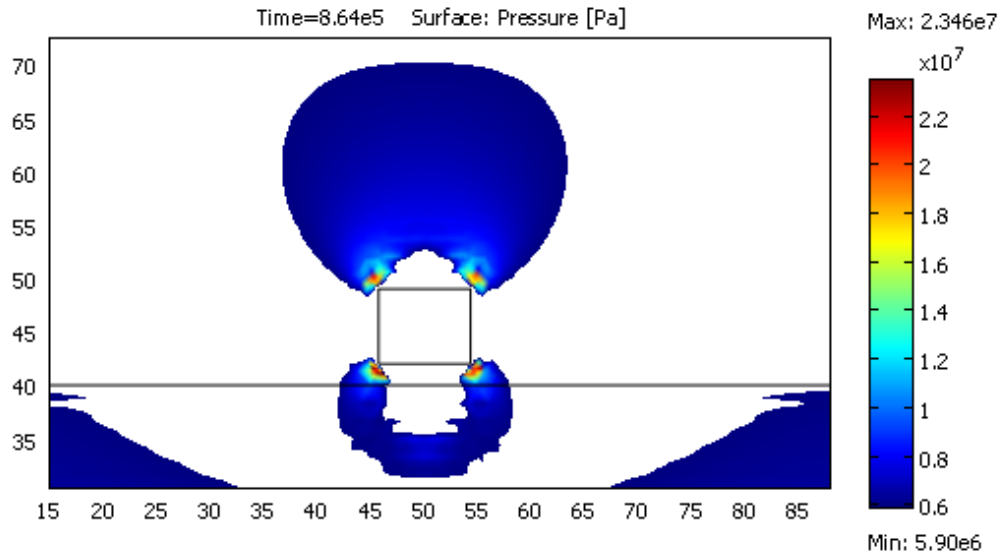
Figure 5.30. Pore pressures greater than 5.9e6 Pa at the end of the excavation.

The pore pressure is negative in the areas up to a distance of 4 m away from the vertical sides of the opening, and also on the roof and the floor (2~3 m) due to volumetric expansion.
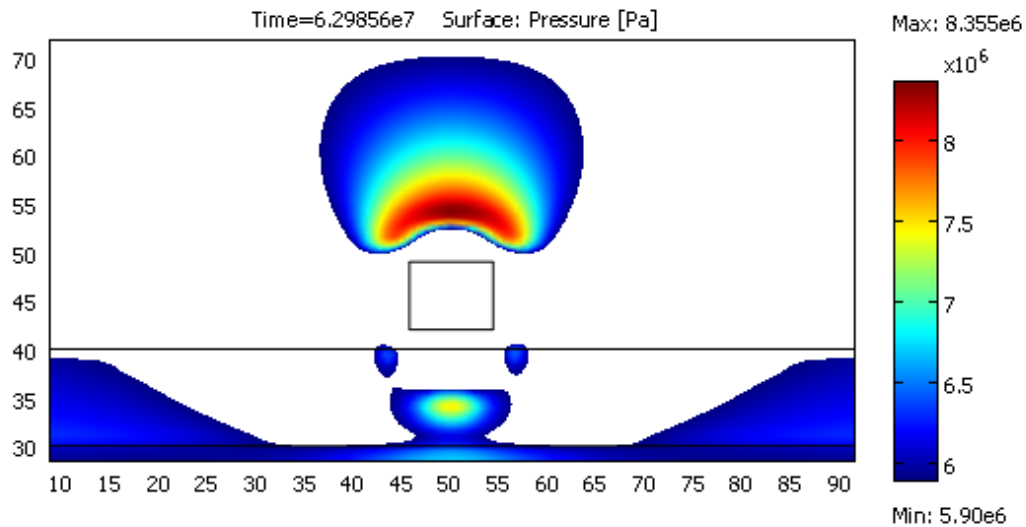

Figure 5.31. Pore pressures greater than 5.9e6 Pa two years after excavation.

The excess pore pressure is also negative above and below the room. The redistribution of pore pressure evolves with time.
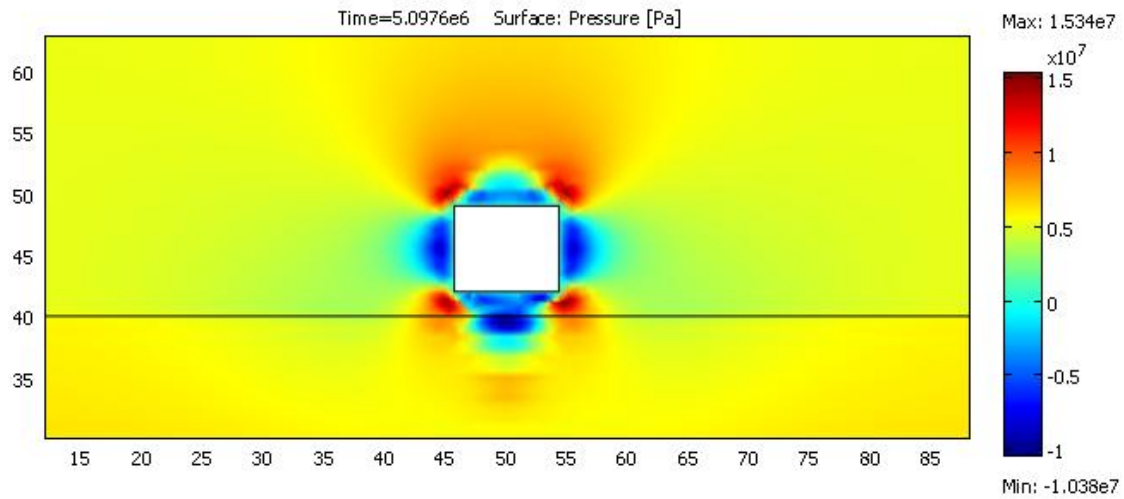

Figure 5.32. Pore pressure distribution after two months from the end of excavation.
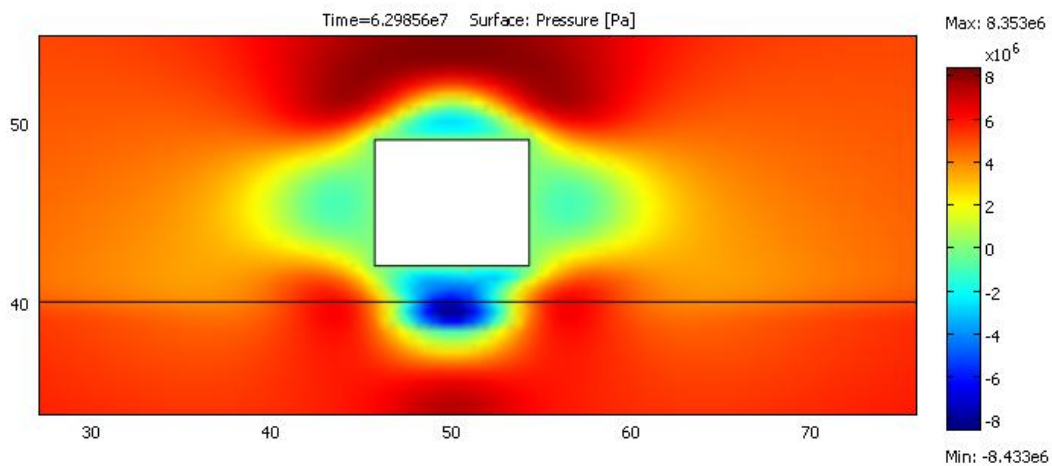

Figure 5.33. Pore pressure distribution after two years from the excavation.

Figure 5.33 shows its distribution after two years from the excavation. The anisotropy in permeability, the low permeability values, and the high stresses generated by the excavation are affecting the patterns of pore pressure distribution. Due to the low permeability of the rock, it could be seen that the pore pressure has not reached a steady state after two years.

Case 2: Permeability as a function of equivalent deviatoric strain

Excavation induces damage in rock. As a result, the material may expand in some areas around the opening and, consequently, the permeability may increase. In order to simulate the increase in permeability, we used Eq. 3 [2].

$$k = k_{ini} \, e^{7000 \, \epsilon_d} \tag{5.3}$$

$$\epsilon_d = \frac{\sqrt{2}}{3} \left((\epsilon_{11} - \epsilon_{22})^2 + (\epsilon_{22} - \epsilon_{33})^2 + (\epsilon_{11} - \epsilon_{33})^2 + 6 \, \epsilon_{12}{}^2 + 6 \, \epsilon_{13}{}^2 + 6 \, \epsilon_{23}{}^2 \right)^{1/2} \tag{5.4}$$

where ϵ_d is the equivalent deviatoric strain and

k_{ini} is the permeability of the undamaged rock.

In order to avoid numerical convergence problems, the value of the permeability is not allowed to increase more than 10^3 times the initial value. Figure 5.34 describes the PP generated at the end of the excavation. After the excavation, the pore pressure continues to evolve with time. Figure 5.35 gives the PP distribution two years after the excavation. A comparison of Figures 5.31 and 5.35 indicates that the increase in permeability due to damage speeds up the pore pressure dissipation.

Figure 5.36 shows the PP distribution two months after the excavation. Figure 5.37 shows the PP distribution two years after the excavation.
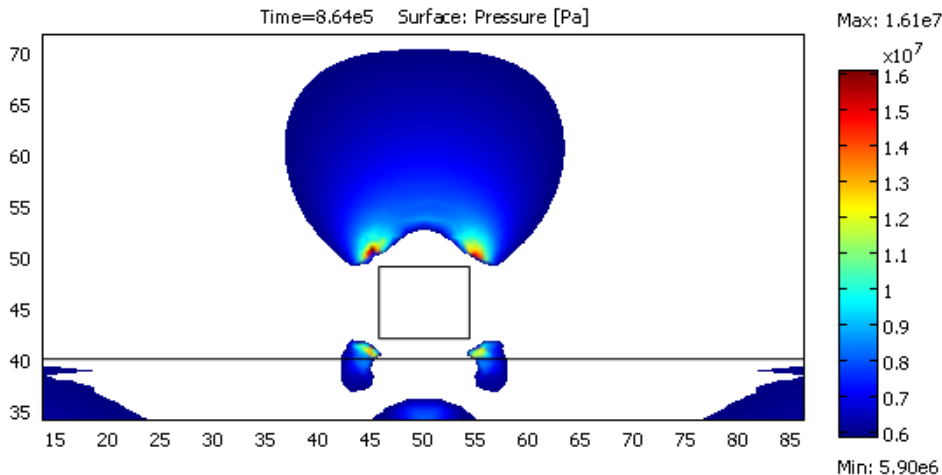

Figure 5.34. Pore pressures greater than 5.9e6 Pa at the end of excavation for variable permeability.
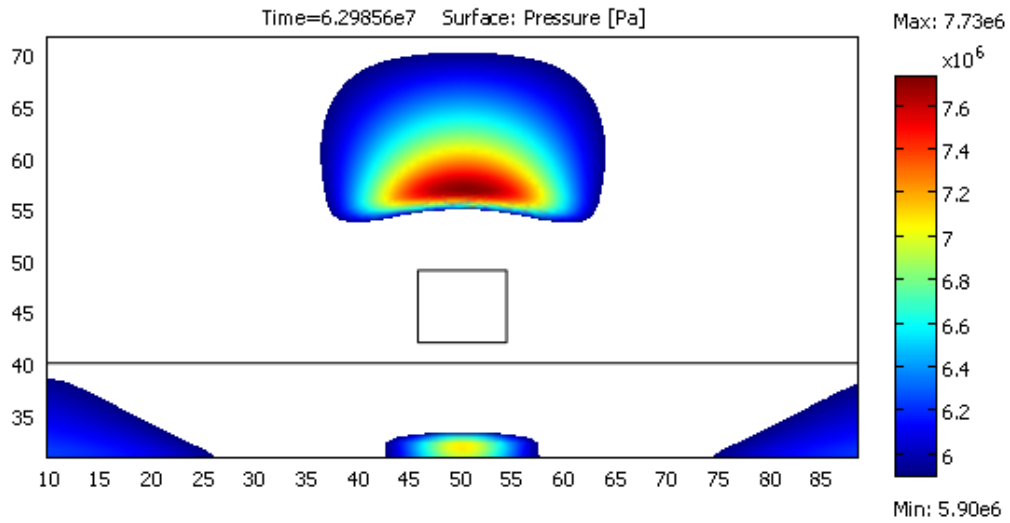
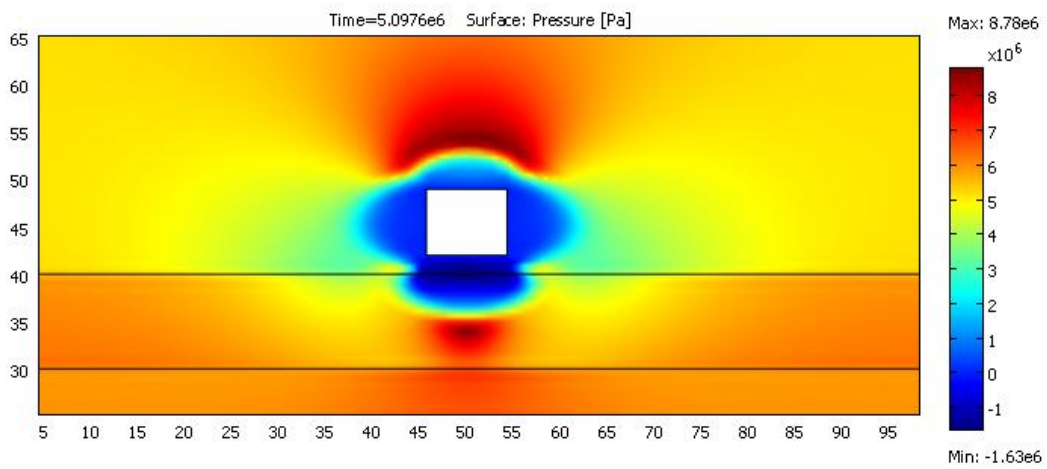Figure 5.35. Pore pressures greater than 5.9e6 Pa two years after excavation for variable permeability.

Figure 5.36. Pore pressure distribution two months after the excavation, for variable permeability.
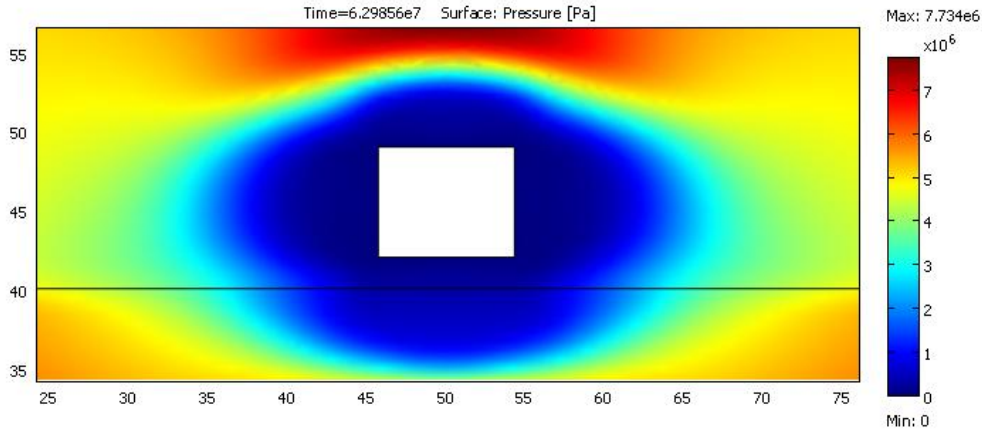
Figure 5.37. Pore pressure distribution after two years from the excavation, for variable permeability.

Pore pressures in compressed and expanded areas

The four points shown in Figure 5.38 are used to investigate the effect of compression or extension on the dissipation of pore pressure with time. Points 1 and 3 are located at a distance of 1.5 m away from the excavation. Points 2 and 4 are 4 m away from the excavation. Points 1 and 2 are located in a compressed area, whereas, points 3 and 4 are located in an expanded area. Two cases of permeability are considered: (a) constant and (b) variable.
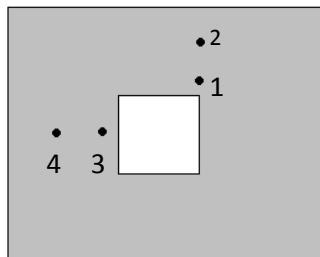
Figure 5.38. Selected points from the domain to track the pore pressure variation with time.

For the case of constant permeability, the generation and dissipation of pore pressure with time at the selected points are shown in Figure 5.39. In the compressed areas, the pore pressure reaches a maximum value at the end of the excavation. After some time, PP starts to dissipate and it takes years to completely dissipate. The pore pressure is higher in the vicinity of the opening than in the areas located far away from the opening. But, PP tends to dissipate more quickly in the areas near the opening. In the expanded areas, the pore pressure starts to

118

dissipate as soon as the excavation starts and reaches the atmospheric pressure in months. The negative pressure developed at point 3 is due to the expansion of the material.
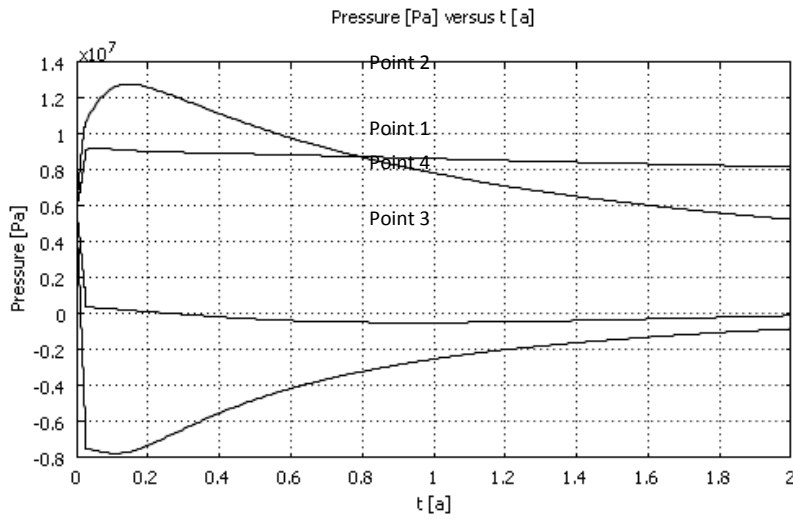
Figure 5.39. Variation of pore pressure with time (years) at selected points (constant permeability).

For variable permeability, the variation of the pore pressure with time at the selected points is shown in Figure 5.40. In general, similar behavior is observed as in the previous case of constant permeability. But here, in compressed areas, the pore pressure dissipates more quickly. In expanded areas, the pore pressure tends to reach the atmospheric pressure in days after the excavation.
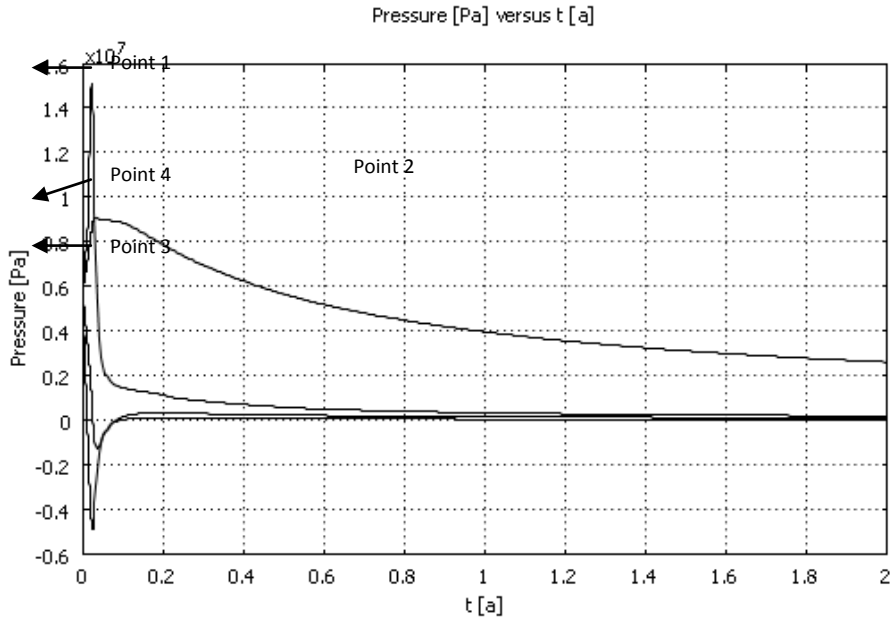
Figure 5.40. Variation of pore pressure with time (years) at selected points (variable permeability).

5.2.7. Conclusions

The conclusions of the hydro-mechanical coupling analysis are summarized below.

- An excavation causes stress concentrations at the corners of a rectangular shape repository.
- Large volumetric strains and effective plastic strains develop around the room and in the weak Sherman Fall layer. These strains increase with time.
- The EDZ is not uniformly distributed around the emplacement room. The size of the EDZ changes with time.
- The degree of the damage within the EDZ is not the same in all locations.
- The pore water pressure dissipation is faster in the analysis with variable permeability than the analysis with constant permeability.
- The type of volumetric strain (expansion or compression), the stress concentrations generated by the excavation, the low permeability of the material, and the anisotropy in permeability have a significant role in the development and dissipation of the pore pressure.

120

References

Abdi, H., Labrie, D., Nguyen, T. S., Barnichon, J. D., Su, G., Evgin, E., Simon, R., and Fall, M. 2012. Laboratory investigation and preliminary modelling of the mechanical behaviour of a transversely isotropic shale. Canadian Geotechnical Conference, Winnipeg, Canada.

Adams, J., and Bell, J. B. 1991. Crustal Stress in Canada. In: Slemmons, D.B., Engdahl, E.R., Zoback, M.D. and Backwell, D.D. (eds). Neotectonics of North America, Decade map volume to accompany the neotectonic maps, part of the Continent-scale maps of North America, Geological Society of America, 367 – 386.

Ajalloeian, R. and Lashkaripour, G. R. 2000. Strength anisotropies in mudrocks. The Bulletin of Engineering Geology and the Environment, 59:195-199.

Angabini, A. 2003. Anisotropy of rock elasticity behavior and of gas migration in a Variscan Carboniferous rock mass in the South Limburg, The Netherlands. Engineering Geology, 67:353-372.

Autio, J., Hjerpe, T., and Siitari-Kauppi, M. 2005. Porosity, diffusivity and permeability of EDZ in crystalline rock and effect on migration in a KBS-3 type repository. Proceedings of a European Commission Cluster conference and workshop, Luxembourg, EUR 21028 EN. pp. 149-155.

Autio, J., Malmlund, H., Hjerpe, T., Kelokaski, M. and Siitari-Kauppi, M., 2003. Excavation damaged zone in the Experimental Deposition Holes at Äspö and Comparison to Existing Data. In MRS 2003 Scientific Basis for Radioactive Waste Management XXVII, Kalmar, Sweden.

Avis J., Lam T., Roberts R., Chace D., Toll N., and Beauheim, R. 2009. Hydraulic testing to characterize low permeability sedimentary formations - proposed Deep Geologic Repository, Tiverton, Ontario. GeoHalifax. Halifax, NS, Canada.

Barbreau, A. and Boisson, J.Y. 1993. Caracterisation d'une formation argileuse: synthèse des principaux résultats obtenus a partir du tunnel de Tournemire. CCE report no. 1 EUR 15736 FR, réf. SERGD 93/22.

Bastiaens, W. and Mertens, J. 2003. EDZ around an industrial excavation in Boom Clay. Proceedings European Commission CLUSTER Conference and Workshop on EDZ in Radioactive Waste Geological Repositories, Luxembourg. 3-5 November 2003, EUR 21028 EN.

Biot, M. A. 1941. General theory of three dimensional consolidations. Journal of Applied Physics, 12:155-164.

Blumling, P., Bernier, F., Lebon, P., and Martin, C. D. 2007. The excavation damaged zone in clay formations time-dependent behavior and influence on performance assessment. Physics and Chemistry of the Earth, 32: 588–599.

Bock, H., Dehandschutter, B., Martin, C.D., Mazurek, M., de Haller, A., Skoczylas, F., and Davy, C. 2009. Self-sealing of fractures in argillaceous formations in context with the geological disposal of radioactive waste. review and synthesis. Report on radioactive waste management, France.

Boisson, J.Y., Cabrera, J., De Windt, L. 1997. Caracterisation d'une formation argileuse – caractérisations des propriétés de transferts au laboratoire des argilites et marnes toarciennes de Tournemire, Aveyron, France. CCE report no. 5, ref. SERGD 97/04.

Boisson, J.Y., Cabrera, J., De Windt, L. 1998. Caracterisation d'une formation argileuse – caracterisation des proprieties de transferts au laboratoire des argilites et marnes toarciennes de Tournemire, Aveyron, France. CCE report no. 5, ref. SERGD 97/04.

Bonin, B. 1998. Deep geological disposal in argillaceous formations: studies at the Tournemire test site. Journal of contaminant hydrology, 35**:**315-330.

Bossart, P., Trick, T., Meier, P. M., Mayor, J.-C. 2004. Structural and Hydrogeological Characterisation of the Excavation-Disturbed Zone in the Opalinus Clay (Mont Terri Rock Project, Switzerland). Applied Clay Science, 26: 429–488.

Carlsson H. 1986. Update: The international Stripa project. IAEA Bulletin, Spring 1986, pp. 25-28.

Chappell, B. A. 1990. Moduli stress dependency in anisotropic rock masses. Mining Science and Technology, 10:127-143.

Charlier, R., Chambon, R., Li, X., Dizier, A., Sieffert, Y., Colin, F., and Levasseur, S. 2008. Modelling the Excavated damage zone around an underground gallery- Coupling mechanical, thermal and hydraulical aspects. Seventh European Commission Conference on the Management and Disposal of Radioactive Waste Euradwast'08, Luxembourg.

Cho, W.-J., Kwon, S., and Park, J.-H. 2008. KURT, a small-scale underground research laboratory for the research on a high-level waste disposal. Annals of Nuclear Energy. 35:123-140.

Corkum, A. G. and Martin, C. D. 2007. The mechanical behaviour of weak mudstone (Opalinus Clay) at low stresses. International Journal of Rock Mechanics and Mining Sciences, 44:196-209.

122

Eberhardt, E., Stead, D., and Stimpson, B. 1999. Quantifying progressive pre-peak brittle fracture damage in rock during uniaxial compression. International Journal of Rock Mechanics and Mining Sciences, 36:361-380.

Emsley, S., Olsson, O., Stenberg, L., Alheid, H.-J., and Falls, S. 1997. ZEDEX-a study of damage and disturbance from tunnel excavation by blasting and tunnel boring. SKB TR-97-30, Svensk Kärnbränslehantering AB. 198.

Fang, Z. and Harrison, J. P. 2002. Development of a local degradation approach to the modelling of brittle fracture in heterogeneous rocks. International Journal of Rock Mechanics and Mining Sciences, 39:443-457.

Fractures Systems Ltd, 2011. Excavation damaged zones assessment. NWMO DGR-TR-2011-21.

Gartner Lee Limited 2008. Phase I: Regional Geomechanics, Southern Ontario. Supporting Technical Report for OPG's Deep Geological Repository for Low and Intermediate Level Wastes. Prepared for Ontario Power Generation. OPG 00216-REP-01300-00008-R00.

Hoek E. 1983. Strength of jointed rock masses. Géotechnique 33, No. 3, 187-223.

Hoek, E., Carranza -Torres, C.T., and Corkum, B. 2002. Hoek-Brown failure criterion: 2002 edition. Proceedings of the North American Rock Mechanics Society Meeting, Toronto, Canada, 1-6.

Hudson, J. A., Backstrom, A., Rutqvist, J., Jing, L., Backers, T., Chijimatsu, M., Feng, X.-T., Kobayashi, A., Koyama, T., Lee, H.-S., Pan, P.-Z., Rinne, M., Shen, B. 2008. Final Report of DECOVALEX-THMC Task B. EDZ Guidance Document-Characterizing and Modeling the Excavation Damaged Zone (EDZ) in Crystalline Rock in the Context of Radioactive Waste Disposal.SKI report. 68.

Hudson, J. A., Backstrom, A., Rutqvist, J., Jing, L., Backers, T., Chijimatsu, M., Christiansson, R., Feng, X.-T., Kobayashi, A., Koyama, T., Lee, H.-S, Neretnieks, I., Pan, P.-Z., Rinne, M., and Shen, B.-T. 2009. Characterizing and modelling the excavation damaged zone in crystalline rock in the context of radioactive waste disposal. Environmental Geology, 57:1275-1297.

Jensen, M., Lam, T., Luhowy, D., McLay, J., Semec, B., and Frizzell, R. 2009. Ontario Power Generation's Proposed L&ILW Deep Geologic Repository: An Overview of Geoscientific Studies. GeoHalifax, 2009. CGS-IAH (CNC), Halifax, NS, Canada.

Kachanov, L. M. 1958. Time of the rupture process under creep conditions. Izv. AN SSSR., Otd. Tekh. Nauk., **8**:26-31 (in Russian).

Kaiser, P.K., Diederichs, M.S., Martin, C.D., Sharp, J., and Steiner, W. 2000. Keynote Lecture: underground works in hard rock tunneling and mining. Proceedings of the GeoEng2000, Melbourne, **1**: 841–926.

Kwon, S. and Cho, W.J. 2008. The influence of an excavation damaged zone on the thermal-mechanical and hydro-mechanical behaviors of an underground excavation. Engineering Geology, 101 (3-4), pp. 110-123.

Lam. T., Martin, D., and McCreath. D. 2007. Characterising the Geomechanics properties of the sedimentary rocks for the DGR excavations. Geotechnical conference, Ottawa.

Labrie, D. and Conlon, B. 2008. Hydraulic and poroelastic properties of porous rocks and concrete materials. The 42nd US Rock Mechanics Symposium, San Francisco, June 29-July 2.

Langer, M. 1999. Principles of geomechanical safety assessment for radioactive waste disposal in salt structures. Engineering Geology, 52:257-269.

Lee, C.F. 1981. In-situ Stress Measurements in Southern Ontario. Proceedings 22rd US Symposium on Rock Mechanics. Rock Mechanics from Research to Application. Massachusetts. 465-472.

Li, L., Aubertin, M., Simon, R., and Bussiere, B. 2005. Formulation and application of a general inelastic locus for geomaterials with variable porosity. Canadian Geotechnical Journal, **42**:601-624.

Liang, W. G., Xu, S. G., and Zhao, Y. S. 2006. Experimental study of temperature effects on physical and mechanical characteristics of salt rock. Rock mechanics and rock engineering, 39:469-482.

Lidskog, R. and Andersson, A. 2001. The management of radioactive waste. A description of ten countries. SKB report.

Lo, K.Y. 1978. Regional Distribution of In-Situ Horizontal Stresses in Rocks of Southern Ontario. Canadian Geotechnical Journal, 15: 371-381.

Lo, K.Y. and Hori, M. 1979. Deformation and strength properties of some rocks in southern Ontario. Canadian Geotechnical Journal, 16:108-120.

Malmgren, L., Saiang, D., Toyra, J., and Bodare, A. The excavation disturbed zone (EDZ) at Kiirunavaara mine, Sweden—by seismic measurements. *Journal of Applied Geophysics*, **61**(1), (2007).

Martin, C. D. 1990. Characterizing in situ stress domains at the AECL Underground Research Laboratory. Canadian Geotechnical Journal, **27**:631-646.

Martin, C. D. 1993. The strength of Massive Lac du Bonnet Granite around underground openings. PhD Thesis, McGill University, Canada.

Martin, C. D. and Chandler, N. A. 1993. Stress heterogeneity and geological structures. International Journal of Rock Mechanics and Mining Sciences & Geomechanics Abstracts, 30:993-999.

Martin, C. D. and Chandler, N. A. 1994. The progressive fracture of Lac du Bonnet granite. International Journal of Rock Mechanics and Mining Sciences & Geomechanics Abstracts, 31:643-659.

Martin, C. D., Chandler, N. A., and Read, R. S. 1997. The role of convergence measurements in characterizing a rock mass. Canadian Geotechnical Journal, 33:363-370.

Martin, C. D., G.W. Lanyon, P. Blumling, and J.-C. Mayor, 2002. The excavation disturbed zone around a test tunnel in the Opalinus Clay. In Proceedings 5th North American Rock Mechanics Symposium and 17th Tunnelling Association of Canada Conference: NARMS/TAC 2002, R. Hammah, W. Baden, J. Curran, and M. Telesnicki, eds., 1581–1588. Toronto: University of Toronto Press.

Martin, C. D., Kaiser, P. K., and McCreath, D. R. 1999. Hoek-Brown parameters for predicting the depth of brittle failure around tunnels. Canadian Geotechnical Journal, 36:136-151.

Matray, J.M., Savoye, S. and Cabrera, J. 2007. Desaturation and structure relationships around drifts excavated in the well-compacted Tournemire's argillite (Aveyron, France). Engineering Geology, 90:1-16.

McEwen, T 2003. Review of the conclusions of previous EDZ workshops. Proceedings of a European Commission CLUSTER conference held in Luxembourg on 3–5 Nov. 2003.

Millard, A. and Rejeb, A. 2008. Simulation of short term and long term responses of the Tournemire argillite in a mine-by-test experiment. The 12th International Conference of International Association for Computer Methods and Advances in Geomechanics (IACMAG) 1-6 October, 2008, Goa, India.

Nguyen, T. S. 2007. Excavation damage and pore pressure evolutions around a test tunnel in granite, Proceedings of the 2007 Canadian Geotechnical Conference, Ottawa.

Niandou, H., Shao, J., Henry, J., and Fourmaintraux, D. 1997. Laboratory investigation of the mechanical behaviour of Tournemire argillite. International Journal of Rock Mechanics and Mining Sciences, 34:3-16.

NWMO Report, 2011a. Excavation Damaged Zones Assessment. Report #: DGR-TR-2011-21.

OPG Report-1. 2011. OPG Deep Geologic Repository for Low & Intermediate Level Waste, Environmental Impact Statement, Volume 1, Main Report, Golder Associates Ltd., 00216-REP-07701-00001-R000, March 2011.

OPG Report – 1, 2008. Phase 1 Geosynthesis, Prepared by Gartner Lee Limited, OPG 00216-REP-01300-00010-R00.

OPG Report - 2, 2008. Phase 1. Long-Term Cavern Stability, Prepared by ITASCA Consulting Group, Inc., OPG 00216-REP-01300-00005-R00.

OPG Report 2008e. OPG's deep geologic repository for low & intermediate level waste, Supporting Technical Report, Phase I, Geosynthesis, Prepared by Gartner Lee, (OPG Report Number (OPG 00216-REP-01300-00010-R001), 126 p.

Perras, M. A., Diederichs, M. S., and Lam, T. 2010. A review of excavation damaged zones in sedimentary rocks with emphasis on numerical modeling for EDZ definition. Geotechnical conference, Calgary, Canada.

Pietruszczak, S. and Mroz, Z. 2001. On failure criteria for anisotropic cohesive-frictional materials. International Journal for Numerical and Analytical Methods in Geomechanics, 2001; 25:509-524.

Popp, T., Salzer, K., and Minkley, W. 2008. Influence of bedding planes to EDZ-evolution and the coupled HM properties of Opalinus Clay. Physics and chemistry of the earth, 33:374-387.

Rabotnov, Y. N. 1971. Creep rupture under stress concentration. Advances in creep design, ed., A. I. Smith and A. M. Nicolson, pp. 3-19.

Read, R. and Birch, K. 2009. The role of rock engineering in developing a deep geological repository in sedimentary rocks. Proceedings of the 3rd CANUS Rock Mechanics Symposium, Toronto.

Rejeb, A. 2003. Time-dependent behaviour of Tournemire argillites (France). Proc. ISRM, Gauteng, South Africa, September 8-12, 2003.

Rejeb, A. and Cabrera, J. 2006. Time-dependent evolution of the excavation damaged zone in the argillaceous Tournemire site (France). In Weiya Xu (Ed.), Proceedings of the 2nd International Conference on Coupled T-H-M-C Processes in Geosystems and Engineering (GeoProc2006), Nanjing, P.R. China, HoHai University, 2006.

Rejeb, A. and Tijani, M. 2003. Stress field in the Tournemire argillaceous. In situ measurements and interpretation, Revue Francais de Géotechnique, 103:75–84.

Rejeb, A., Millard, A., and Maleki, K. 2007. Mine-by-test experiment around the excavated 2003 gallery in the Tournemire site. NFPRO Project. DEI/SARG/2007-040.

Rutqvist, J. and Stephansson, O. 2003. The role of hydromechanical coupling in fractured rock engineering. Hydrogeology Journal, 11:7–40.

Rutqvist, J., Backstrom, A., Chijimatsu, M., Feng, X., Pan, P., Hudson, J., Jing, L., Kobayashi, A., Koyama, T., Lee, H., Huang, X., Rinne, M., and Shen, B. 2009. A multiple-code simulation study of the long-term EDZ evolution of geological nuclear waste repositories. Environmental Geology, 57:1313-1324.

Rutqvist, J., Borgesson, L., Chijimatsu, M., Hernelind, J., Jing, L., Kobayashi, A., and Nguyen, S. 2009. Modeling of damage, permeability changes and pressure responses during excavation of the TSX tunnel in granitic rock at URL, Canada. Environmental Geology, 57:1263-1274.

Sato, T., Kikuchi, T., and Sugihara, K. 2000. In-situ experiments on an excavation disturbed zone induced by mechanical excavation in Neogene sedimentary rock at Tono mine, central Japan. Engineering Geology, 56:97-108.

Schmitt, L. 1994. Etude du soutenement hydraulique des puits petroliers dans les argilites par l'essai triaxial a confinement fluide direct. These de doctoral INPL (ENSG de Nancy).

Soonawala, N. M. 1984. An overview of the geophysics activity within the Canadian nuclear fuel waste management program. Geoexploration, 22: 149-168.

Souley, M., Homand, F., and Chibout, M. 1999. A 3D numerical modeling of damage extension around an underground excavation: Effect of cut-off keys in bulkhead design. The 37th U.S. Symposium on Rock Mechanics (USRMS), June 7 - 9, Vail, CO.

Souley, M., Homand, F., Pepa, S., and Hoxha, D. 2001. Damage-induced permeability changes in granite: a case example at the URL in Canada. International Journal of Rock Mechanics and Mining Sciences, 38: 297-310.

Stormont, J. C. 1997. In situ gas permeability measurements to delineate damage in rock salt. International Journal of Rock Mechanics and Mining Sciences, 34:1055-1064.

Sugihara, K. 2009. Geological disposal of high-level radioactive waste and the role of rock engineering. International Journal of the Japanese Committee for Rock Mechanics, **5**:19-24.

Takemura, T., Takahashi, M., and Makana, M. 2006. Mechanical and chemical properties changes in sedimentary rock during immersion in hot water. EUROCK 2006 – Multiphysics Coupling and Long Term Behaviour in Rock Mechanics – Van Cotthem, Charlier, Thimus & Tshibangu (eds), Taylor & Francis Group, London, pp. 163-167.

Tang, C.A., Tham, L.G., Lee, P.K.K., Yang, T.H., and Li, L.C. 2002. Coupled analysis of flow, stress and damage (FSD) in rock failure. International Journal of Rock Mechanics and Mining Sciences, 39:477–489.

Tsang, C.-F., and Bernier, F. 2004. Definitions of excavation disturbed zone and excavation damaged zone, Luxembourg, 3-5 November 2003, European Commission Report EUR 21028 EN.

Tsang C-F, Bernier F., and Davies C. 2005. Geohydromechanical processes in the Excavation Damaged Zone in crystalline rock, rock salt, and indurated and plastic clays—in the context of radioactive waste disposal. International Journal of Rock Mechanics and Mining Sciences, 42 (1), pp. 109-125.

Wai, R.S.C., and Lo, K.Y. 1982. Temperature effects on strength and deformation behaviour of rocks in southern Ontario. Canadian Geotechnical Journal, 19: 307-319.

Zienkiewicz and Taylor, 2005. Finite Element Method for Solid and Structural Mechanics. Textbook.